

A Variational Framework for Phase-Field Fracture Modeling with Applications to Microstructure Fragmentation, Dewatering, Ductile Failure, and Spallation

by

Tianchen Hu

Department of Mechanical Engineering and Materials Science
Duke University

Date: _____
Approved:

John Dolbow, Advisor

Wilkins Aquino

Johann Guilleminot

Manolis Veveakis

Benjamin W. Spencer

Dissertation submitted in partial fulfillment of the requirements for the degree of
Doctor of Philosophy in the Department of Mechanical Engineering and Materials
Science
in the Graduate School of Duke University
2021

ABSTRACT

A Variational Framework for Phase-Field Fracture Modeling
with Applications to Microstructure Fragmentation,
Dessication, Ductile Failure, and Spallation

by

Tianchen Hu

Department of Mechanical Engineering and Materials Science
Duke University

Date: _____
Approved:

John Dolbow, Advisor

Wilkins Aquino

Johann Guilleminot

Manolis Veveakis

Benjamin W. Spencer

An abstract of a dissertation submitted in partial fulfillment of the requirements for
the degree of Doctor of Philosophy in the Department of Mechanical Engineering
and Materials Science
in the Graduate School of Duke University
2021

Copyright © 2021 by Tianchen Hu
All rights reserved

Abstract

Lorem ipsum dolor sit amet, consectetur adipiscing elit. Sed porta finibus lacus venenatis varius. Proin luctus, est ac facilisis aliquam, leo est tempus velit, eu euismod mi nunc ut odio. Nulla porttitor velit vel dolor dapibus sollicitudin. Sed lobortis lorem ut dui bibendum pellentesque. Curabitur in volutpat ex, ut semper ipsum. In auctor ac ex euismod aliquet. Ut rutrum neque sed felis auctor luctus. Mauris nec lorem placerat, mattis turpis vel, lacinia purus. Maecenas nunc mauris, semper ut aliquam at, luctus sed justo. Proin porttitor cursus orci. Ut id vehicula massa, ac sagittis lectus. Sed eget justo faucibus, posuere purus.

Contents

Abstract	iv
List of Tables	viii
List of Figures	ix
Acknowledgements	xv
1 Introduction	1
1.1 Background	1
1.2 Organization of the dissertation	1
1.3 Notation	1
2 The Variational Framework	3
2.1 Kinematics and Constraints	3
2.2 Thermodynamics	5
2.3 The minimization problem	10
2.4 Discretization	15
3 Brittle and Quasi-Brittle Fracture: Fracture Evolution in Polycrystalline Materials	18
3.1 Introduction	18
3.2 Theory	20
3.2.1 Constitutive choices	20
3.2.2 Approximation of the pressure boundary condition	23

3.2.3	Governing equations	25
3.3	Verification	26
3.3.1	Uniaxial traction of a bar	26
3.3.2	Pressurized crack propagation	27
3.4	Numerical examples	29
3.4.1	Predicting the critical fracture strength	29
3.4.2	High burnup structure fragmentation	38
4	Cohesive Fracture: Soil Dessication	45
4.1	Introduction	45
4.2	Theory	50
4.2.1	Constitutive choices	50
4.2.2	Enforcing the traction-free boundary condition	52
4.2.3	Stochastic models for fracture properties	55
4.3	Verification	63
4.3.1	Mode I: Edge-Notched Unilateral Tension Test	63
4.3.2	Mode II: Edge-Notched Shear Test	66
4.3.3	Crack Propagation Under Biaxial Tension	69
4.3.4	Reconstruction of the marginal PDF	73
4.4	Numerical examples	73
4.4.1	One-Dimensional Simplification: Side View	73
4.4.2	Two-Dimensional Simplification: Stochastic Aspects of Fracture	77
4.4.3	Inverse Identification Based on Three-Dimensional Physical Experiments	89
5	Towards Ductile Fracture	95
5.1	Introduction	95

5.2	Theory	95
5.2.1	Constitutive choices	95
5.2.2	A power-law approximation to the yield surface	95
5.2.3	Variational constitutive updates	95
5.3	Verification	95
5.3.1	A homogeneous example: uniaxial constitutive response	95
5.3.2	A nonhomogeneous example: uniaxial load-displacement curves	95
5.3.3	Crack resistance curves	95
5.4	Numerical examples	95
5.4.1	Three-point bending	95
5.4.2	The Sandia Fracture Challange	95
5.4.3	Spallation of oxidation scale	95
6	Conclusion	96
A	Code availability	97
B	On the phase-field irreversibility constraint	98
C	The flooding algorithm for counting fragments	99
	Bibliography	103
	Biography	112

List of Tables

3.1	Parameters and material properties used in the intergranular fracture simulations	31
3.2	Summary of fracture strength obtained from 15 realizations of 3 porosity values. R denotes the realization index.	38
3.3	Parameters and material properties used in the fission-gas-induced HBS fracture simulations.	39
4.1	Summary of material properties and model parameters for all calculations in ??	78
4.2	Summary of material properties of mining waste and model parameters for all calculations in ??	90
C.1	Demonstration of classification after the update from time step n to time step n+1. Broken elements are denoted with an underscore. . .	102

List of Figures

3.1	A bar under uniaxial tension.	26
3.2	Phase-field variable in initial conditions (for internal length scale $l = 20$ mm). The red and blue color correspond to value of 10^{-3} and 0, respectively.	26
3.3	A bar under uniaxial tension with different pressure values \bar{p} : (a) Reaction force on the left boundary. (b) Reaction force on the right boundary. (c) Regularized pressure value.	28
3.4	A bar under uniaxial tension with different internal lengths l	29
3.5	Sneddon benchmark problem.	30
3.6	Comparison between the numerical results and the LEFM solution for the critical pressure values.	31
3.7	(a) The lenticular geometry is described by the length L , the thickness S and the dihedral angle ϕ . (b) Gas bubble geometry and boundary conditions. (c) Comparison of stress-strain curves for different gas bubble geometries.	33
3.8	Final configuration (crack surfaces highlighted in blue) for different loading (a) uniaxial (b) biaxial (c) triaxial.	34
3.9	Comparison of stress-strain curves for different loading conditions. . .	35
3.10	(a-c) Initial configuration of REVs with an average grain size of $9.4\text{ }\mu\text{m}$. (d-f) Final configuration (crack surfaces highlighted in blue) for REVs. Different porosity values are considered: (a, d) 2.02%, (b, e) 4.04%, (c, f) 6.06%.	36
3.11	Comparison of stress-strain curves for different porosity values.	36

3.12 Variation in normalized fracture strength with changing porosity. In the current chapter, five trial calculations were performed for each porosity level, and each calculation was based on one realization of the spatial distribution of bubbles. The 95% confidence interval is shown in stripes.	38
3.13 Results for (a-c) the small bubble with radius 0.25 μm and (d-f) the large bubble with radius 0.25 μm (a, d) Pressure history. (b, e) Crack paths superimposed on the voronoi structure. (c, f) Contour plot of the maximum principal stress.	40
3.14 Results for bubble radius 0.5 μm and external pressure (a-c) 0 MPa, (d-f) 30 MPa, (g-i) 60 MPa. (a, d, g) Pressure history. (b, e, h) Crack paths superimposed on the voronoi structure. (c, f, i) Contour plot of the maximum principal stress.	41
3.15 Results for (a-b) the two-bubble case and (c-d) the three-bubble case. (a, c) Crack paths superimposed on the voronoi structure. (b, d) Contour plot of the maximum principal stress.	43
3.16 (a, c, e) Crack paths superimposed on the microstructure and (b, d, f) contour plots of the maximum principal stress assuming different recrystallization stages: (a-b) 25% recrystallization, (c-d) 60% recrystallization, (e-f) 100% recrystallization.	44
4.1 Boundary conditions of the plate with a pre-existing crack for (a) a mode I tension test and (d) a mode II shear test. Finite element meshes for the mode I calculations (b - c) and for the mode II calculations (e - f). For (b, e) the meshes have the initial crack geometry “meshed-in” while (c, f) have local refinement around the initial damage field. All meshes are pre-refined along the predicted crack-path with a characteristic element size of 0.005 mm.	65
4.2 Edge-notched specimen loaded in tension with initial crack represented by a geometric notch with a rounded corner. (a) Dimensions of the notched plate. Damage d at (b) $u_y = 0 \text{ mm}$, (c) $u_y = 0.0048 \text{ mm}$, (d) $u_y = 0.006 \text{ mm}$	65
4.3 Edge-notched specimen loaded in tension with initial crack represented by a damage field. (a) Dimensions of the intact plate. The Damage d at (b) $u_y = 0 \text{ mm}$ (c) $u_y = 0.0048 \text{ mm}$ (d) $u_y = 0.006 \text{ mm}$	66

4.4 Mode I force–displacement curves obtained using (a) the spectral decomposition with two representations of the pre-existing crack (b) a spectral decomposition in conjunction with the contact split with different critical damage threshold on two representations of the pre-existing crack.	67
4.5 The crack paths obtained using (a-d) the spectral decomposition on a geometrically notched plate, (e-h) the spectral decomposition with an initial damage field d_0 (4.53) representing the initial crack, and (i-l) the contact split with an initial damage field. Snapshots of crack paths are shown at (b,f,j) $u_x = 0$ mm, (c,g,k) $u_x = 0.0109$ mm, and (d,h,l) $u_x = 0.02$ mm.	68
4.6 Mode II force–displacement curves obtained using (a) spectral decomposition with two representations of the initial crack (b) spectral decomposition in conjunction with the contact split with different critical damage threshold on two representations of the initial crack.	69
4.7 (a) Dimensions and boundary conditions of a thin plate with two parallel initial cracks. (b) The initial cracks are represented by an initial damage field.	71
4.8 Crack paths obtained using (a-c) a no-split technique (d-f) the spectral decomposition (g-i) the contact split.	72
4.9 Contour plot of the normal pressure right before the bridge forms. The pressure is calculated for an orientation that is estimated to be orthogonal to the bridge. Elements within the contour of $d = 0.75$ are removed to indicate the current crack set.	73
4.10 Description of a one-dimensional model for thin-film cracking. (a) Side view (highlighted in yellow) of the geometry (b) schematic representation of the side view. The elasticity solution is derived for the region highlighted with the shaded box, i.e. between the two discontinuities across the thin film. The coordinate system is centered at the middle of the bottom surface of the thin film.	74
4.11 The principal of “super-superposition” applied to the region of interest marked in Figure 4.10b. The analytical solution is derived based on the boundary conditions shown in (c).	74
4.12 Relationship between the dimensionless fracture driving energy and the dimensionless crack spacing: (a) analytical solution using linear elasticity; and (b) numerically generated curves using the phase-field for cohesive model detailed in this work.	77

4.13 Description of a two-dimensional model for thin-film cracking. (a) Top view (highlighted in yellow) (b) schematic representation of the top view. A typical crack is shown to emphasize that fracture is only considered in the film.	79
4.14 Damage fields resulting from six pairs of realizations with different correlation models and normalized correlation lengths. The left three pairs (a-b, g-h, m-n) are realizations obtained with a PSE covariance function, while the right three pairs (d-e, j-k, p-q) are samples generated with a PE covariance function. Energy release rate \mathcal{G}_c and the critical fracture energy ψ_c have a coefficient of variation of 0.03, and normalized spatial correlation length L^* of (a-b, d-e) 0.05 (g-h, j-k) 0.1 (m-n, p-q) 0.2 The corresponding damage fields are shown in (c, f, i, l, o, r), respectively. In these results, independent realizations of the underlying Gaussian fields are used.	82
4.15 Three pairs of qualitative comparison of smoothness of the kernel function with the same normalized correlation length $L^* = 0.05$. (a-f) pair 1 (g-l) pair 2 (m-r) pair 3. Each row compares two kernel functions transformed from the same samples of the underlying Gaussian fields.	83
4.16 (a, c) Mean dimensionless crack spacing \underline{l}^* versus dimensionless crack driving force \mathcal{D}^* (b, d) Estimated probability density of dimensionless crack spacing for different values of correlation length when $\mathcal{D}^* = 5.17$ based on (a-b) a PSE kernel (c-d) a PE kernel	84
4.17 Comparisons of (a) mean dimensionless crack spacing \underline{l}^* versus dimensionless crack driving force \mathcal{D}^* and (b) Estimated probability density of dimensionless crack spacing for different values of correlation length when $\mathcal{D}^* = 5.17$ for results obtained using a PSE kernel and a PE kernel	85
4.18 Point-wise correlated material properties: (a-f) normalized fracture toughness \mathcal{G}_c^* and (g-l) normalized critical fracture energy ψ_c^* with (left) PSE covariance function (right) PE covariance function	86
4.19 Comparisons of (a) mean dimensionless crack spacing as a function of dimensionless crack driving force and (b) estimated PDFs of dimensionless fragment size at loading $\mathcal{D}^* = 5.17$ for results with an underlying PSE kernel	86
4.20 Comparisons of (a) mean dimensionless crack spacing and dimensionless crack driving force and (b) estimated PDFs of dimensionless fragment size at loading $\mathcal{D}^* = 5.17$ for results with an underlying PE kernel	87

4.21 Superposition of fracture networks obtained by three samples of different coefficients of correlation, using the PSE kernel. Only the volume within the damage contour of $d = 0.9$ is shown to represent the resulting fracture network. Three samples are sampled (a) by holding \mathcal{G}_c constant and (b) by holding ψ_c constant.	88
4.22 Snapshots of damage field at different loading levels with $d \geq 0.75$ plotted over (a-c) fracture toughness \mathcal{G}_c and (d-f) critical fracture energy ψ_c with an underlying PSE covariance function	89
4.23 Snapshots of damage field at different loading levels with $d \geq 0.75$ plotted over (a-c) fracture toughness \mathcal{G}_c and (d-f) critical fracture energy ψ_c with an underlying PE covariance function	90
4.24 Three sets of experiments and calculations for (a-e) unilateral agitation (f-j) rotational agitation (k-o) point agitation. (b, g, l) snapshots of crack patterns from experiments. postulated spatially correlated (c, h, m) fracture toughness and (d, i, n) critical fracture energy to reproduce experimental observations. (e, j, o) damage fields obtained using corresponding spatially varying material properties.	91
4.25 Procedures of finding the optimal hyperparameter to match the experiment: (a) 12 pairs of fracture properties are sampled to explore the space of admissible spatial correlation lengths; three dimensional energy minimization problems are solved to obtain (b) the resulting fracture morphology; (c) distributions of fragment sizes are extracted from the simulated results, and the log-likelihood values of these distributions at the samples extracted from (d) the experimental fracture morphology are computed.	92
4.26 (a) Estimated PDFs of the dimensionless fragment sizes extracted from the experimental result and the calibrated stochastic model. (b) Fracture morphology obtained using the calibrated fracture properties. (c) Photograph of cracks in the mining waste.	93
4.27 Qualitative comparison between the experiments and the simulations: (a-c) Photographs (modified from [1]) of cracks in mining waste due to desiccation at steady state for three test specimens with thickness (a) 4 mm, (b) 8 mm, and (c) 16 mm. (d-f) Top view and (g-i) panoramic view of corresponding numerical simulation results with different film thickness. Volumes of material with $d \geq 0.75$ were removed to improve the visualization of the crack geometry.	94

C.1	(a) Final damage field obtained using a spatially correlated random \mathcal{G}_c and ψ_c . (b) Corresponding clusters labeled by the flooding algorithm. Cluster boundaries are marked in black.	100
C.2	Status change from step n to step n+1. “Broken” elements are labeled in yellow, and “intact” elements are white. The step-by-step reclassification procedure is shown in Table C.1.	102

Acknowledgements

I am thankful for the many people.

1

Introduction

Introduction placeholder.

1.1 Background

1.2 Organization of the dissertation

1.3 Notation

In what follows, deterministic scalar, vectors, second-order tensors, and fourth-order tensors are denoted by a (or A), \mathbf{a} (or \mathbf{A}), \mathbf{A} , and \mathbb{A} , respectively.

Let Ω be a collection of points $\mathbf{X} \in \mathbb{R}^d$, $d \in \{1, 2, 3\}$. Scalar- and vector-valued random fields defined on the probability space $(\Theta, \Sigma, \mathbb{P})$, indexed by Ω , are denoted as $\{A(\mathbf{X}), \mathbf{X} \in \Omega\}$ and $\{\mathbf{A}(\mathbf{X}), \mathbf{X} \in \Omega\}$, respectively. At any fixed material point $\mathbf{X} \in \Omega$, $a(\mathbf{X})$ and $\mathbf{a}(\mathbf{X})$ are random variables defined on the probability space $(\Theta, \Sigma, \mathbb{P})$. For any fixed $\theta \in \Theta$, $a(\theta)$ and $\mathbf{a}(\theta)$ are realizations of the random variables. Similarly, $\mathbf{X} \mapsto a(\mathbf{X}; \theta)$ and $\mathbf{X} \mapsto \mathbf{a}(\mathbf{X}; \theta)$ are realizations of the random fields $\{A(\mathbf{X}), \mathbf{X} \in \Omega\}$ and $\{\mathbf{A}(\mathbf{X}), \mathbf{X} \in \Omega\}$.

Einstein summations are assumed wherever applicable unless otherwise stated.

For any vectors \mathbf{a} and \mathbf{b} of the same size, the inner product is defined as $\mathbf{a} \cdot \mathbf{b} = a_i b_i$ where a_i and b_i are components of the vectors. The associated vector norm is $\|\mathbf{a}\|^2 = a \cdot a$. Similarly, for any second-order tensors \mathbf{A} and \mathbf{B} of the same size, the inner product is defined as $\mathbf{A} : \mathbf{B} = \text{tr}(\mathbf{A}^T \mathbf{B})$. The associated Frobenius norm writes $\|\mathbf{A}\|_F = \sqrt{\mathbf{A} : \mathbf{A}}$.

2

The Variational Framework

2.1 Kinematics and Constraints

Let us start by defining degrees of freedom in the system. Let Ω be a body consisting of a continuous collection of material points. Let $\Omega_0 \subset \mathbb{R}^d$ be the reference configuration at some time $t = t_0$, whose particles are identified by their position \mathbf{X} , and $\Omega_t \subset \mathbb{R}^d$ be the current configuration at a time $t > t_0$, with particles at position \mathbf{x} . Let $\Phi : \Omega_0 \times [t_0, t] \mapsto \mathbb{R}^d$ be the deformation map. The deformation gradient is denoted as $\mathbf{F} = \nabla \Phi$, where the operator ∇ denotes differentiation with respect to \mathbf{X} (in the reference configuration Ω_0). The Jacobian determinant of the deformation gradient is written as $J = \det \mathbf{F}$.

Throughout this contribution, the *local thermodynamic state* of an infinitesimal material neighborhood is defined by:

- the deformation gradient \mathbf{F} from the Lie group of invertible and orientation-preserving linear transformations in \mathbb{R}^d ;
- the collection of internal variables $\mathbf{Z} \in \mathbb{M}$, where the set \mathbb{M} depend on the material;

- the entropy density per unit volume $s \in \mathbb{R}$ in the reference configuration;

Plastic (or creep) deformations are modeled through the framework of multiplicative decomposition

$$\mathbf{F} = \mathbf{F}^e \mathbf{F}^p \mathbf{F}^g, \quad (2.1)$$

where \mathbf{F}^e , \mathbf{F}^p are referred to as the elastic and plastic deformation gradients, respectively. \mathbf{F}^g is the product of eigen deformation gradients. For example, isotropic thermal expansion can be accounted for by $\mathbf{F}^g = (1 + \alpha \Delta T) \mathbf{I}$, where α is the thermal expansion coefficient, and $\Delta T = T - T_0$ is the temperature change from the reference temperature T_0 .

Crack surfaces are regularized and modeled using a phase-field d , $0 \leq d \leq 1$, where $d = 0$ represents the intact state of a material point, and $d = 1$ indicates the material point has lost all of its load-carrying capacity.

For the systems of interest in this contribution, the internal variables are considered to be the plastic deformation \mathbf{F}^p (from the same Lie group of \mathbf{F}), the (scalar) effective plastic strain $\bar{\varepsilon}^p \in \mathbb{R}_+$, and the phase-field d regularizing the crack surfaces, i.e.

$$\mathbf{Z} = \{\mathbf{F}^p, \bar{\varepsilon}^p, d\}. \quad (2.2)$$

In general, internal variables evolve subject to constraints of the following form

$$\mathbf{L}(\mathbf{Z}) \dot{\mathbf{Z}} = \mathbf{0}. \quad (2.3)$$

The specific form of the constraint depends on physical requirements and the material class. For isotropic J_2 -plasticity, the Prandtl-Reuss flow rule requires

$$\text{tr} \left(\dot{\mathbf{F}}^p \mathbf{F}^{p-1} \right) = 0, \quad (2.4a)$$

$$\left\| \dot{\mathbf{F}}^p \mathbf{F}^{p-1} \right\|^2 - \frac{3}{2} |\dot{\varepsilon}^p|^2 = 0, \quad (2.4b)$$

where (2.4a) requires the plastic flow to be isochoric, and (2.4b) normalizes the effective plastic strain $\bar{\varepsilon}^p$ to be uniaxial. Furthermore, the plastic flow is assumed to be irreversible in the sense

$$\dot{\bar{\varepsilon}}^p \geq 0. \quad (2.5)$$

Since the phase-field variable d is an approximation to the irreversible crack set, and as will be shown later, the crack geometric function is a monotonically increasing function of d , it is intuitive to impose the irreversibility constraint on the phase-field variable, i.e.

$$\dot{d} \geq 0. \quad (2.6)$$

Note that (2.4a), (2.4b), (2.5), and (2.6) are all of the general form (2.3).

2.2 Thermodynamics

Recall that the motions of the body are described by the deformation mapping $\Phi : \Omega_0 \times [t_0, t] \mapsto \mathbb{R}^d$. Let ρ_0 be the density in the reference configuration, \mathbf{b} be the distributed body force per unit mass, \mathbf{P} be the first Piola-Kirchhoff stress, \mathbf{n}_0 be the outward normal in the reference configuration, u be the internal energy density, $k = \rho_0 \dot{\Phi} \cdot \dot{\Phi}$ be the kinetic energy density, \mathcal{P}^{ext} be the external power expenditure, s be the entropy density, q be the distributed heat source per unit mass, and \mathbf{h} be the heat flux. The densities u , k and s are all defined per unit volume in the reference configuration. The motions of the body must obey the following conservations and thermodynamic laws:

- Conservation of mass:

$$\frac{d}{dt} \int_{\Omega'} \rho_0 \, dV = 0. \quad (2.7)$$

- Conservation of linear momentum:

$$\frac{d}{dt} \int_{\Omega'} \rho_0 \dot{\Phi} dV = \int_{\Omega'} \rho_0 \mathbf{b} dV + \int_{\partial\Omega'} \mathbf{P} \mathbf{n}_0 dA. \quad (2.8)$$

- Conservation of angular momentum:

$$\frac{d}{dt} \int_{\Omega'} \Phi \times (\rho_0 \dot{\Phi}) dV = \int_{\Omega'} \Phi \times (\rho_0 \mathbf{b}) dV + \int_{\partial\Omega'} \Phi \times (\mathbf{P} \mathbf{n}_0) dA. \quad (2.9)$$

- The first law of thermodynamics:

$$\frac{d}{dt} \int_{\Omega'} u dV + \frac{d}{dt} \int_{\Omega'} k dV = \int_{\Omega'} \mathcal{P}^{\text{ext}} dV + \int_{\Omega'} \rho_0 q dV - \int_{\partial\Omega'} \mathbf{h} \cdot \mathbf{n}_0 dA. \quad (2.10)$$

- The second law of thermodynamics:

$$\frac{d}{dt} \int_{\Omega'} s dV - \int_{\Omega'} \frac{\rho_0 q}{T} dV + \int_{\partial\Omega'} \frac{\mathbf{h} \cdot \mathbf{n}_0}{T} dA \geq 0. \quad (2.11)$$

All the above conservation and thermodynamic laws hold for any arbitrary subbody $\Omega' \subset \Omega$, hence they can be written in the following local form:

$$\dot{\rho}_0 = 0, \quad (2.12a)$$

$$\rho_0 \mathbf{a} = \nabla \cdot \mathbf{P} + \rho_0 \mathbf{b}, \quad (2.12b)$$

$$\mathbf{P} \mathbf{F} = \mathbf{F} \mathbf{P}^T, \quad (2.12c)$$

$$\dot{u} + \dot{k} = \mathcal{P}^{\text{ext}} + \rho_0 q - \nabla \cdot \mathbf{h}, \quad (2.12d)$$

$$\dot{s}^{\text{int}} = \dot{s} - \frac{\rho_0 q}{T} + \nabla \cdot \frac{\mathbf{h}}{T} \geq 0. \quad (2.12e)$$

Alternatively, local form of the second law can be written in terms of the internal energy density as

$$\dot{s}^{\text{int}} = \mathcal{P}^{\text{ext}} - \dot{u} - \frac{1}{T} \mathbf{h} \cdot \nabla T. \quad (2.13)$$

For convenience, the collection of thermodynamic state variables (working with the Helmholtz free energy), kinematic degrees of freedom, and internal variables are defined as

$$\mathcal{S} = \{\mathcal{K}, T\}, \quad \mathcal{K} = \{\boldsymbol{\Phi}, \mathbf{Z}\}, \quad \mathbf{Z} = \{\mathbf{F}^p, \bar{\varepsilon}^p, d\}. \quad (2.14)$$

The rates of change of the kinematic variables are denoted as $\mathcal{V} = \{\dot{\boldsymbol{\Phi}}, \dot{\mathbf{F}}^p, \dot{\bar{\varepsilon}}^p, \dot{d}\}$.

The generalized velocities of the kinematic state variables are collected in the set

$$\dot{\Lambda} = \{\dot{\boldsymbol{\Phi}}, \dot{\mathbf{F}}, \dot{\mathbf{F}}^p, \dot{\bar{\varepsilon}}^p, \dot{d}, \nabla \dot{d}\}. \quad (2.15)$$

Recall that the local thermodynamic state is assumed to be depend only on $\boldsymbol{\Phi}$, \mathbf{Z} and s , i.e.

$$u = \hat{u}(\Lambda, s), \quad T = \hat{T}(\Lambda, s). \quad (2.16)$$

It is convenient to work with the Helmholtz free energy density (per unit volume) with T as a state variable by introducing the Legendre transformation

$$\psi(\Lambda, T) = \inf_s [u(\Lambda, s) - Ts]. \quad (2.17)$$

The local form of the second law can then be rewritten using the identity $\dot{\psi} = \dot{u} - \dot{T}s$ and the fact that $\mathcal{P}^{\text{ext}} = \mathcal{P}^{\text{int}}$:

$$\dot{s}^{\text{int}} = \delta - \frac{1}{T} \mathbf{h} \cdot \nabla T, \quad \delta = \mathcal{P}^{\text{int}} - \dot{\psi} - \dot{T}s. \quad (2.18)$$

where δ shall be referred to as the internal dissipation density (per unit volume).

Combining (2.12e) and (2.18) yields the energy balance in the *entropy form*:

$$T\dot{s} = \rho_0 q - \nabla \cdot \mathbf{h} + \delta. \quad (2.19)$$

The internal power expenditure \mathcal{P}^{int} can be expressed in terms of generalized forces as

$$\mathcal{P}^{\text{int}} = \mathbf{P} : \dot{\mathbf{F}} + \mathbf{T} : \dot{\mathbf{F}}^p + Y \dot{\bar{\varepsilon}}^p + f \dot{d} + \boldsymbol{\xi} \cdot \nabla \dot{d}. \quad (2.20)$$

It is assumed that each of the generalized forces can be additively decomposed into an equilibrium part, thermodynamically conjugate to the Helmholtz free energy density, and a viscous part, i.e.

$$\mathbf{P} = \mathbf{P}^{\text{eq}}(\Lambda, T) + \mathbf{P}^{\text{vis}}(\dot{\mathbf{F}}, T; \Lambda), \quad (2.21\text{a})$$

$$\mathbf{T} = \mathbf{T}^{\text{eq}}(\Lambda, T) + \mathbf{T}^{\text{vis}}(\dot{\mathbf{F}}^p, T; \Lambda), \quad (2.21\text{b})$$

$$Y = Y^{\text{eq}}(\Lambda, T) + Y^{\text{vis}}(\dot{\varepsilon}^p, T; \Lambda), \quad (2.21\text{c})$$

$$f = f^{\text{eq}}(\Lambda, T) + f^{\text{vis}}(\dot{d}, T; \Lambda), \quad (2.21\text{d})$$

$$\boldsymbol{\xi} = \boldsymbol{\xi}^{\text{eq}}(\Lambda, T) + \boldsymbol{\xi}^{\text{vis}}(\nabla \dot{d}, T; \Lambda), \quad (2.21\text{e})$$

where the viscous forces vanish as the rate diminishes to preclude viscous dissipation in quasi-static processes, i.e.

$$\lim_{\|\dot{\mathbf{F}}\| \rightarrow 0^+} \mathbf{P}^{\text{vis}} = 0, \quad (2.22\text{a})$$

$$\lim_{\|\dot{\mathbf{F}}^p\| \rightarrow 0^+} \mathbf{T}^{\text{vis}} = 0, \quad (2.22\text{b})$$

$$\lim_{|\dot{\varepsilon}^p| \rightarrow 0^+} Y^{\text{vis}} = 0, \quad (2.22\text{c})$$

$$\lim_{|\dot{d}| \rightarrow 0^+} f^{\text{vis}} = 0, \quad (2.22\text{d})$$

$$\lim_{\|\nabla \dot{d}\| \rightarrow 0^+} \boldsymbol{\xi}^{\text{vis}} = 0. \quad (2.22\text{e})$$

For convenience, the equilibrium forces and the viscous forces are collected in the sets

$$\mathcal{F}^{\text{eq}} = \{\mathbf{P}^{\text{eq}}, \mathbf{T}^{\text{eq}}, Y^{\text{eq}}, f^{\text{eq}}, \boldsymbol{\xi}^{\text{eq}}\}, \quad \mathcal{F}^{\text{vis}} = \{\mathbf{P}^{\text{vis}}, \mathbf{T}^{\text{vis}}, Y^{\text{vis}}, f^{\text{vis}}, \boldsymbol{\xi}^{\text{vis}}\}. \quad (2.23)$$

The rate of the Helmholtz free energy density can be expanded as

$$\dot{\psi} = \psi_{,\mathbf{F}} : \dot{\mathbf{F}} + \psi_{,\mathbf{F}^p} : \dot{\mathbf{F}}^p + \psi_{,\dot{\varepsilon}^p} \dot{\varepsilon}^p + \psi_{,d} \dot{d} + \psi_{,\nabla d} \cdot \nabla \dot{d} + \psi_{,T} \dot{T}. \quad (2.24)$$

Inserting the identity (2.24) into (2.18) and applying the Coleman-Noll procedure

lead to several thermodynamic restrictions on the constitutive relations:

$$\begin{aligned} \mathbf{P}^{\text{eq}} &= \psi_{,\mathbf{F}}, & \mathbf{T}^{\text{eq}} &= \psi_{,\mathbf{F}^p}, & Y^{\text{eq}} &= \psi_{,\bar{\varepsilon}^p}, & f^{\text{eq}} &= \psi_{,d}, & \boldsymbol{\xi}^{\text{eq}} &= \psi_{,\nabla d}, & -s &= \psi_{,T}. \end{aligned} \quad (2.25)$$

Substituting (2.25) and (2.24) into (2.18) simplifies the definition of the internal dissipation density:

$$\delta = \mathbf{P}^{\text{vis}} : \dot{\mathbf{F}} + \mathbf{T}^{\text{vis}} : \dot{\mathbf{F}}^p + Y^{\text{vis}} \dot{\bar{\varepsilon}}^p + f^{\text{vis}} \dot{d} + \boldsymbol{\xi}^{\text{vis}} \cdot \nabla d. \quad (2.26)$$

Using the identities (2.24) and (2.25), the rate of the entropy density can be expanded as

$$\dot{s} = -\dot{\psi}_{,T} = -\mathbf{P}_{,T}^{\text{eq}} : \dot{\mathbf{F}} - \mathbf{T}_{,T}^{\text{eq}} : \dot{\mathbf{F}}^p - Y_{,T}^{\text{eq}} \dot{\bar{\varepsilon}}^p - f_{,T}^{\text{eq}} \dot{d} - \boldsymbol{\xi}_{,T}^{\text{eq}} \cdot \nabla d - \psi_{,TT} \dot{T}. \quad (2.27)$$

By introducing the heat capacity per unit mass at constant Λ :

$$\rho_0 c_v = -T \psi_{,TT}, \quad (2.28)$$

the energy balance (2.19) can be rewritten as

$$\rho_0 c_v \dot{T} = \rho_0 q - \nabla \cdot \mathbf{h} + \delta + \delta_T, \quad (2.29)$$

where δ_T is the dissipation density accounting for the thermal effects in the thermodynamic conjugates:

$$\delta_T = T \left(\mathbf{P}_{,T}^{\text{eq}} : \dot{\mathbf{F}} + \mathbf{T}_{,T}^{\text{eq}} : \dot{\mathbf{F}}^p + Y_{,T}^{\text{eq}} \dot{\bar{\varepsilon}}^p + f_{,T}^{\text{eq}} \dot{d} + \boldsymbol{\xi}_{,T}^{\text{eq}} \cdot \nabla d \right), \quad (2.30)$$

e.g. $T \mathbf{P}_{,T}^{\text{eq}} : \dot{\mathbf{F}}$ is the dissipation accounting for thermoelastic effects, and $T Y_{,T}^{\text{eq}} \dot{\bar{\varepsilon}}^p$ is the dissipation accounting for thermoplastic softening.

2.3 The minimization problem

In this section, we construct a potential such that *all* the conservation and thermodynamic laws can be derived (if not implied by construction) from a minimization problem. First, we assume that the Helmholtz free energy density ψ can be additively decomposed into a strain-energy density ψ^e , a plastic energy density ψ^p , a fracture energy density ψ^f , and a thermal energy density ψ^h :

$$\psi = \psi^e(\mathbf{F}, \mathbf{F}^p, d, T) + \psi^p(\bar{\varepsilon}^p, d, T) + \psi^f(d, \nabla d, T) + \psi^h(T). \quad (2.31)$$

To maintain a variational structure, the viscous forces are supposed to be derived from dual kinetic potentials.

Example (The elastic dual kinetic potential). Suppose there exist a potential $\zeta(\mathbf{P}^{\text{vis}})$ such that

$$\dot{\mathbf{F}} = \zeta_{,\mathbf{P}^{\text{vis}}}. \quad (2.32)$$

The dual kinetic potential is introduced by applying the Legendre transformation:

$$\psi^{e*}(\dot{\mathbf{F}}) = \sup_{\mathbf{P}^{\text{vis}}} \left[\mathbf{P}^{\text{vis}} : \dot{\mathbf{F}} - \zeta \right], \quad (2.33)$$

where it follows immediately that

$$\mathbf{P}^{\text{vis}} = \psi^{e*}_{,\dot{\mathbf{F}}}. \quad (2.34)$$

Note that the symbol ψ^{e*} is chosen in line with the energetic counterpart of the potential, not to imply that ψ^{e*} is the Legendre transformation of ψ^e . In fact, ψ^{e*} is the Legendre transformation of ζ .

Following the foregoing example, the viscous forces are defined as

$$\mathbf{P}^{\text{vis}} = \psi^{e*}_{,\dot{\mathbf{F}}}, \quad \mathbf{T}^{\text{vis}} = \psi^{p*}_{,\dot{\mathbf{F}}^p}, \quad \mathbf{Y}^{\text{vis}} = \psi^{p*}_{,\dot{\varepsilon}^p}, \quad \mathbf{f}^{\text{vis}} = \psi^{f*}_{,d}, \quad \boldsymbol{\xi}^{\text{vis}} = \psi^{f*}_{,\nabla d}, \quad (2.35)$$

where ψ^{e*} is the elastic dual kinetic potential describing rate-sensitivity of the deformation, e.g. Newtonian viscosity; ψ^{p*} is the plastic dual kinetic potential describing

the rate-sensitivity of cold work, e.g. viscoplasticity; ψ^{f*} is the fracture dual kinetic potential describing viscous regularization of fracture propagation.

To satisfy the second law (2.13), the material is assumed to be *strictly dissipative* in the sense that every thermodynamic process results in an increase in entropy for nonzero rates, i.e. $\mathcal{F}^{\text{dis}} \cdot \dot{\Lambda} > \mathbf{0}$, $\forall \dot{\Lambda} \neq 0$. These constraints are subject to later verification.

The external power expenditure $\mathcal{P}^{\text{ext}}(\dot{\Phi}, T)$ is defined as

$$\begin{aligned} \mathcal{P}^{\text{ext}} = & \underbrace{\int_{\Omega_0} \rho_0 \mathbf{b} \cdot \dot{\Phi} \, dV}_{\text{body force}} + \underbrace{\int_{\partial_t \Omega_0} \mathbf{t} \cdot \dot{\Phi} \, dA}_{\text{surface traction}} + \underbrace{\int_{\partial_h \Omega_0} \bar{h}_n \ln \left(\frac{T}{T_0} \right) \, dA}_{\text{external heat flux}} \\ & + \underbrace{\int_{\partial_r \Omega_0} h \left[T - T_0 \ln \left(\frac{T}{T_0} \right) \right] \, dA}_{\text{external heat convection}} - \underbrace{\int_{\Omega_0} \rho_0 q \ln \left(\frac{T}{T_0} \right) \, dV}_{\text{heat source}}, \end{aligned} \quad (2.36)$$

where the subscripts in ∂_t , ∂_h and ∂_r denote the corresponding subsets of the surface with the associated Neumann/Robin boundary conditions. \bar{h}_n is the heat flux, h is the heat transfer coefficient, and T_0 is the reference or the ambient temperature.

To account for heat generation due to dissipations (i.e. from dual kinetic potentials), it is necessary to introduce the concept of the *equilibrium temperature* corresponding to the thermodynamic state $\{\Lambda, s\}$ defined as

$$T^{\text{eq}} = u_{,s}(\Lambda, s), \quad (2.37)$$

and the *external temperature* T , along with a dummy integration factor T/T^{eq} . It will be shown later that the equilibrium temperature will be equal to the external temperature at equilibrium, and that the integration factor brings the effect of dissipation mechanisms into heat generation.

The total potential is constructed such that given the current kinematic state variables Λ and the current temperature, the velocities \mathcal{V} and the rate of temperature

change can be obtained as a critical point following the first variations, which can then be used to update the state variables. The total potential L is constructed as

$$L(\dot{\Lambda}, \dot{s}, T, \nabla T) = \int_{\Omega_0} \varphi(\dot{\Lambda}, \dot{s}, T) \, dV - \mathcal{P}^{\text{ext}}(\dot{\Lambda}, T), \quad (2.38a)$$

$$\varphi(\dot{\Lambda}, \dot{s}, T, \nabla T) = \dot{u}(\dot{\Lambda}) + \dot{u}(\dot{\Lambda}, \dot{s}) + \Delta^* \left(\frac{T}{T^{\text{eq}}} \dot{\Lambda}, T^{\text{eq}} \right) - T \dot{s} - \chi(\mathbf{g}), \quad (2.38b)$$

where \dot{u} is the rate of change in the internal energy, \dot{s} is the rate of change in the entropy, Δ^* is the sum of dual kinetic potentials:

$$\Delta^*(\dot{\Lambda}, T; \Lambda) = \psi^{e*}(\dot{\mathbf{F}}, T; \Lambda) + \psi^{p*}(\dot{\mathbf{F}}^p, \dot{\varepsilon}^p, T; \Lambda) + \psi^{f*}(\dot{d}, \nabla \dot{d}, T; \Lambda), \quad (2.39)$$

and χ is the Fourier potential defined in terms of the normalized temperature gradient $\mathbf{g} = -\frac{1}{T} \nabla T$, with the property $-\mathbf{h} = \chi_{,\mathbf{g}}$. Finally, the entire problem can be cast variational into the following inf-sup problem as

$$(\mathcal{V}, \dot{s}, T) = \arg \left[\inf_{\mathcal{V}, \dot{s}} \sup_T L(\dot{\Lambda}, \dot{s}, T, \nabla T) \right]. \quad (2.40)$$

Owing to [2, 3], the solutions of (2.40) have the following properties: Assume Ω_0 is open and bounded with only Dirichlet boundary conditions, and let $\hat{T} \equiv \ln(T/T_0)$, $\hat{T} \in \mathbb{R}$. If χ is convex in $\nabla \hat{T}$ and grows as a power $|\nabla \hat{T}|^p$, $1 < p < \infty$, then $L(\dot{\Lambda}, \dot{s}, T)$ attains its supremum $L(\dot{\Lambda}, \dot{s})$ in the Sobolev space $W^{1,p}(\Omega_0)$. If χ is *strictly convex* in ∇u , then the solution T is unique. The existence of the solution $\dot{\Lambda}$ is endorsed by the polyconvexity of the potentials $\dot{u}(\dot{\Lambda}, \dot{s})$ and $\Delta^*(\dot{\Lambda})$. In addition, the dissipation inequality (e.g. (2.12e)) is satisfied if $\Delta^*(\dot{\Lambda}, T)$ attains its infimum for every $\dot{\Lambda}$ when the rate is zero.

Remark. One may attempt to state the variational inf-sup problem without relying on the concept of the equilibrium temperature, the external temperature, and the integration factor:

$$(\mathcal{V}, \dot{s}, T) = \arg \left[\inf_{\mathcal{V}, \dot{s}} \sup_T L'(\dot{\Lambda}, \dot{s}, T, \nabla T) \right], \quad (2.41a)$$

$$L'(\dot{\Lambda}, \dot{s}, T, \nabla T) = \int_{\Omega_0} \varphi'(\dot{\Lambda}, \dot{s}, T, \nabla T) \, dV - \mathcal{P}^{\text{ext}}(\dot{\Lambda}, T), \quad (2.41b)$$

$$\varphi'(\dot{\Lambda}, \dot{s}, T, \nabla T) = k(\dot{\Phi}) + \dot{u}(\dot{\Lambda}, \dot{s}) + \Delta^*(\dot{\Lambda}, T) - T\dot{s} - \chi(\mathbf{g}). \quad (2.41c)$$

However, it immediately follows that the supremum of (2.41a) in T does not include contributions from dissipation mechanisms:

$$\rho_0 c_v \dot{T} = \rho_0 q - \nabla \cdot \mathbf{h}, \quad (2.42)$$

which clearly violates the first law of thermodynamics (2.29).

To find the critical points of the inf-sup problem (2.40), we first isolate the local state variables from the global state variables. That is, (2.40) can be reorganized as

$$(\mathcal{V}, \dot{s}, T) = \arg \left[\inf_{\dot{\Phi}, \dot{d}} \sup_T L \left(\inf_{\dot{\mathbf{F}}^p, \dot{\varepsilon}^p, \dot{s}} \varphi \right) \right], \quad (2.43)$$

since the updates of \mathbf{F}^p , $\dot{\varepsilon}^p$ and s can be performed point-wise. Expanding \dot{u} in (2.38b) and substituting the constitutive restrictions (2.25) yield

$$\begin{aligned} \varphi(\dot{\Lambda}, \dot{s}, T, \nabla T) &= \rho_0 \mathbf{a} \cdot \dot{\Phi} + \mathbf{P}^{\text{eq}} : \dot{\mathbf{F}} + \mathbf{T}^{\text{eq}} : \dot{\mathbf{F}}^p + Y^{\text{eq}} \dot{\varepsilon}^p + f^{\text{eq}} \dot{d} + \boldsymbol{\xi}^{\text{eq}} \cdot \nabla \dot{d} \\ &\quad + T^{\text{eq}} \dot{s} + \Delta^* \left(\frac{T}{T^{\text{eq}}} \dot{\Lambda}, T^{\text{eq}} \right) - T \dot{s} - \chi(\mathbf{g}). \end{aligned} \quad (2.44)$$

The minimizer in \dot{s} follows as

$$T^{\text{eq}} - T = 0. \quad (2.45)$$

The infimum in $\dot{\mathbf{F}}^p$ and $\dot{\varepsilon}^p$ shall follow from the joint minimization problem subject

to the flow rule (2.3), i.e.

$$\begin{aligned} \left(\dot{\mathbf{F}}^p, \dot{\bar{\varepsilon}}^p \right) = \arg \inf_{\dot{\mathbf{F}}^p, \dot{\bar{\varepsilon}}^p} & \left[\mathbf{T}^{\text{eq}} : \dot{\mathbf{F}}^p + Y^{\text{eq}} \dot{\bar{\varepsilon}}^p + \Delta^* \right] \\ \text{subject to} & \quad \mathbf{L}(\mathbf{Z}) \dot{\mathbf{Z}} = \mathbf{0}. \end{aligned} \quad (2.46)$$

To find the infimum in T , substitute the definition of the free energy (2.31), the definition of the dual kinetic potential (2.39), the definition of the external power (2.36), and the constitutive restrictions (2.25) into (2.38a) to obtain

$$\begin{aligned} L(\dot{\Lambda}, \dot{s}, T, \nabla T) = & \int_{\Omega_0} \left[\rho_0 \mathbf{a} \cdot \dot{\boldsymbol{\phi}} + \mathbf{P}^{\text{eq}} : \dot{\mathbf{F}} + \mathbf{T}^{\text{eq}} : \dot{\mathbf{F}}^p + Y^{\text{eq}} \dot{\bar{\varepsilon}}^p + f^{\text{eq}} \dot{d} \right. \\ & \left. + \boldsymbol{\xi}^{\text{eq}} \cdot \nabla \dot{d} + T^{\text{eq}} \dot{\Lambda}, T^{\text{eq}} \right] - T \dot{s} - \chi(\mathbf{g}) \, dV \\ & - \int_{\Omega_0} \rho_0 \mathbf{b} \cdot \dot{\boldsymbol{\phi}} \, dV - \int_{\partial_t \Omega_0} \mathbf{t} \cdot \dot{\boldsymbol{\phi}} \, dA - \int_{\partial_h \Omega_0} \bar{h}_n \ln \left(\frac{T}{T_0} \right) \, dA \\ & - \int_{\partial_r \Omega_0} h \left[T - T_0 \ln \left(\frac{T}{T_0} \right) \right] \, dA + \int_{\Omega_0} \rho_0 q \ln \left(\frac{T}{T_0} \right) \, dV \end{aligned} \quad (2.47)$$

The variation of (2.47) in T in the admissible space (admissible with respect to Dirichlet boundary conditions) is

$$T \dot{s} = \rho_0 q - \nabla \cdot \mathbf{h} + \delta, \quad \forall \mathbf{X} \in \Omega_0, \quad (2.48a)$$

$$\mathbf{h} \cdot \mathbf{n}_0 = \bar{h}_n, \quad \forall \mathbf{X} \in \partial_h \Omega_0, \quad (2.48b)$$

$$\mathbf{h} \cdot \mathbf{n}_0 = h(T - T_0), \quad \forall \mathbf{X} \in \partial_r \Omega_0. \quad (2.48c)$$

With the substitution of (2.27) and the definition of heat capacity (2.28), the first law in the form of (2.29) is recovered

$$\rho_0 c_v \dot{T} = \rho_0 q - \nabla \cdot \mathbf{h} + \delta + \delta_T. \quad (2.49)$$

Next, the balance of linear momentum and traction boundary conditions are recov-

ered from variations in the admissible fields of $\dot{\Phi}$:

$$\rho_0 \mathbf{a} = \nabla \cdot \mathbf{P} + \mathbf{b}, \quad \forall \mathbf{X} \in \Omega_0, \quad (2.50a)$$

$$\mathbf{P} \mathbf{n}_0 = \mathbf{t}, \quad \forall \mathbf{X} \in \partial_t \Omega_0. \quad (2.50b)$$

Finally, variation in the admissible space of \dot{d} yields the fracture evolution equation on the inactive set

$$\nabla \cdot \boldsymbol{\xi} - f = 0, \quad \forall \mathbf{X} \in \mathcal{I}(\Omega_0), \quad (2.51)$$

$$\boldsymbol{\xi} \cdot \mathbf{n}_0 = 0, \quad \forall \mathbf{X} \in \mathcal{I}(\partial_d \Omega_0). \quad (2.52)$$

2.4 Discretization

We begin this section by summarizing the strong form of the general initial boundary value problem of interest:

The initial boundary value problem for the time interval $t \in I = [t_0, t_f]$

Linear momentum balance: $\rho_0 \mathbf{a} = \nabla \cdot \mathbf{P} + \rho_0 \mathbf{b},$	$\Omega_0 \times]t_0, t[,$
$\mathbf{P} \mathbf{n}_0 = \mathbf{t},$	$\partial_t \Omega_0 \times]t_0, t[,$
$\boldsymbol{\Phi} = \boldsymbol{\Phi}_g,$	$\partial_u \Omega_0 \times]t_0, t[,$
Fracture evolution: $\nabla \cdot \boldsymbol{\xi} - f = 0,$	$\mathcal{I}_t(\Omega_0) \times]t_0, t[,$
$\boldsymbol{\xi} \cdot \mathbf{n}_0 = 0,$	$\mathcal{I}_t(\partial_d \Omega_0) \times]t_0, t[,$
Heat transfer: $\rho_0 c_v \dot{T} = \rho_0 q - \nabla \cdot \mathbf{h} + \delta + \delta_T,$	$\Omega_0 \times]t_0, t[,$
$\mathbf{h} \cdot \mathbf{n}_0 = \bar{h}_n,$	$\partial_h \Omega_0 \times]t_0, t[,$
$\mathbf{h} \cdot \mathbf{n}_0 = h(T - T_0),$	$\partial_r \Omega_0 \times]t_0, t[,$
$T = T_g,$	$\partial_T \Omega_0 \times]t_0, t[,$
Initial conditions: $\boldsymbol{\Phi} = \boldsymbol{\Phi}_0,$	$\Omega_0, t = t_0,$
$\dot{\boldsymbol{\Phi}} = \mathbf{v}_0,$	$\Omega_0, t = t_0,$
$d = d_0,$	$\Omega_0, t = t_0,$
$T = T_0,$	$\Omega_0, t = t_0.$

The yield surface and the flow rule (and their corresponding constitutive updates)

are defined only after specific constitutive assumptions are made in the following chapters (e.g. Chapter 5).

To derive the weak form, we begin by introducing the trial spaces \mathcal{U}_t , \mathcal{D}_t and \mathcal{T}_t

$$\mathcal{U}_t = \{\boldsymbol{\Phi} \in \mathcal{H}^1(\Omega_0)^d \mid \mathbf{u} = \mathbf{u}_g \text{ on } \partial_u \Omega_0\}, \quad (2.53a)$$

$$\mathcal{D}_t = \{d \in \mathcal{H}^1(\Omega_0) \mid \dot{d} > 0 \text{ on } \mathcal{I}_t(\Omega_0)\}, \quad (2.53b)$$

$$\mathcal{T}_t = \{T \in \mathcal{H}^1(\Omega_0) \mid T = T_g \text{ on } \partial_T \Omega_0\}, \quad (2.53c)$$

and the weighting spaces \mathcal{V} , \mathcal{C} and \mathcal{E}

$$\mathcal{V} = \{\mathbf{w} \in \mathcal{H}^1(\Omega_0)^d \mid \mathbf{w} = \mathbf{0} \text{ on } \partial_u \Omega_0\}, \quad (2.54a)$$

$$\mathcal{C} = \{c \in \mathcal{H}^1(\Omega_0)\}, \quad (2.54b)$$

$$\mathcal{E} = \{e \in \mathcal{H}^1(\Omega_0) \mid T = 0 \text{ on } \partial_T \Omega_0\}. \quad (2.54c)$$

The weak form can be derived as:

The weak form

Given parameters in the IBVP, find $\boldsymbol{\Phi} \in \mathcal{U}_t$, $d \in \mathcal{D}_t$ and $T \in \mathcal{T}_t$, $t \in [t_0, t_f]$, such that $\forall \mathbf{w} \in \mathcal{V}$, $\forall c \in \mathcal{C}$ and $\forall e \in \mathcal{E}$,

$$(\mathbf{w}, \rho_0 \mathbf{a}) + (\nabla \mathbf{w}, \mathbf{P}) - (\mathbf{w}, \rho_0 \mathbf{b}) - \langle \mathbf{w}, \mathbf{t} \rangle_{\partial_t \Omega_0} = 0, \quad (2.55a)$$

$$(\nabla c, \boldsymbol{\xi}) + (c, f) = 0, \quad (2.55b)$$

$$\begin{aligned} - \left(e, \rho_0 c_v \dot{T} \right) + (e, \rho_0 q) + (\nabla e, \mathbf{h}) + (e, \delta + \delta_T) \\ - \langle e, \bar{h}_n \rangle_{\partial_h \Omega_0} - \langle e, h(T - T_0) \rangle_{\partial_r \Omega_0} = 0, \end{aligned} \quad (2.55c)$$

with projections of initial conditions

$$(\mathbf{w}, \boldsymbol{\Phi} - \boldsymbol{\Phi}_0) = 0, \quad (2.56a)$$

$$\left(\mathbf{w}, \dot{\boldsymbol{\Phi}} - \mathbf{v}_0 \right) = 0, \quad (2.56b)$$

$$(c, d - d_0) = 0, \quad (2.56c)$$

$$(e, T - T_0) = 0. \quad (2.56d)$$

Using the Galerkin method, with finite dimensional function spaces $\tilde{\mathcal{U}}_t \subset \mathcal{U}_t$, $\tilde{\mathcal{V}} \subset \mathcal{V}$, $\tilde{\mathcal{D}}_t \subset \mathcal{D}_t$, $\tilde{\mathcal{C}} \subset \mathcal{C}$, $\tilde{\mathcal{T}}_t \subset \mathcal{T}_t$, $\tilde{\mathcal{E}} \subset \mathcal{E}$, we arrive at the spatially discrete form of the problem:

The semidiscrete Galerkin form

Given parameters in the IBVP, find $\Phi^h \in \tilde{\mathcal{U}}_t$, $d^h \in \tilde{\mathcal{D}}_t$ and $T^h \in \tilde{\mathcal{T}}_t$, $t \in [t_0, t_f]$, such that $\forall \mathbf{w}^h \in \tilde{\mathcal{V}}$, $\forall q^h \in \tilde{\mathcal{C}}$ and $\forall e^h \in \tilde{\mathcal{E}}$,

$$(\mathbf{w}^h, \rho_0 \mathbf{a}) + (\nabla \mathbf{w}^h, \mathbf{P}) - (\mathbf{w}^h, \rho_0 \mathbf{b}) - \langle \mathbf{w}^h, \mathbf{t} \rangle_{\partial_t \Omega_0} = 0, \quad (2.57a)$$

$$(\nabla c^h, \boldsymbol{\xi}) + (c^h, f) = 0, \quad (2.57b)$$

$$\begin{aligned} & - (e^h, \rho_0 c_v \dot{T}) + (e^h, \rho_0 q) + (\nabla e^h, \mathbf{h}) + (e^h, \delta + \delta_T) \\ & - \langle e^h, \bar{h}_n \rangle_{\partial_h \Omega_0} - \langle e^h, h(T^h - T_0) \rangle_{\partial_r \Omega_0} = 0, \end{aligned} \quad (2.57c)$$

with projections of initial conditions

$$(\mathbf{w}^h, \Phi^h - \Phi_0) = 0, \quad (2.58a)$$

$$(\mathbf{w}^h, \dot{\Phi} - \mathbf{v}_0) = 0, \quad (2.58b)$$

$$(c^h, d^h - d_0) = 0, \quad (2.58c)$$

$$(e^h, T^h - T_0) = 0. \quad (2.58d)$$

The discrete inequality for crack irreversibility is satisfied node-wise with a primal-dual active set strategy. See e.g. Heister et al. [4] for implementational details of such a solver. The solver is also generally available in numerical toolboxes, e.g. PETSc [5]. The discrete approximation is calculated using a fixed-point iterative solution scheme outlined from [6]. The semidiscrete momentum balance equation (2.57a) is further discretized using the generalized- α method. The semidiscrete fracture evolution equation (2.57b) and the heat conduction equation (2.57c) are further discretized using the backward-Euler time integration. Discretizations of the plasticity constitutive updates are discussed in Chapter 5.

3

Brittle and Quasi-Brittle Fracture: Fracture Evolution in Polycrystalline Materials

3.1 Introduction

During the operation of commercial light water reactors, fission of uranium dioxide (UO_2) produces a variety of fission products within the fuel matrix. The fracture behavior of brittle materials is strongly influenced by their underlying microstructural features such as gas bubbles, second-phase particles, pre-existing micro-cracks, grains, grain boundaries, etc. For example, the bubbles at the grain boundaries alter the fracture properties, and subsequently affects the pellet-cladding mechanical interaction (PCMI), fission gas release and swelling. Therefore, it is important to develop a fracture model that incorporates the effects of microstructural features to better understand how fission changes the fracture response of the nuclear fuel.

On the other hand, to improve the economics of commercial nuclear power production, utilities are seeking to increase the allowable burnup limit for UO_2 fuel. A main factor contributing to the current burnup limit in commercial light-water reactors is the risk of fragmentation during a loss-of-coolant accident (LOCA). To allow

the industry to pursue an increased burnup limit and develop mitigation strategies, an improved capability for predicting the onset of fragmentation is essential.

A thorough review of high-burnup fuel fragmentation is provided in [7]. In the current work, we focus on the fine fragmentation that results in fuel fragments typically less than 0.1 mm in size. It has been reported that fine fragmentation primarily occurs at high burnups—especially when the high-burnup structure (HBS) has formed. The HBS is typically characterized by small newly formed grains with sizes of 100–300 nm and round fission gas pores of micrometric size [8]. It is hypothesized that over-pressurization of fission gas bubbles in the UO₂ HBS could result in fine fragmentation during typical LOCA transients.

In general, fuel fracture can be modeled using phenomenological [9] and mechanical models [10]. Various criteria have been used to determine whether fine fragmentation will occur during a LOCA, but such criteria are all based on simple analytical models [11, 12]. For additional insights into gas-bubble-induced fracture in polycrystalline materials and HBS fine fragmentation (including crack topology, fragment morphology, and fragment topography), a physics-based model is needed to simulate over-pressurization of fission gas bubbles.

Recently, the phase-field fracture models have been applied to study gas-bubble-induced fracture in polycrystalline materials. Chakraborty et al. [13] developed a hierarchical multi-scale approach to model microstructure-sensitive brittle fracture, and 2D simulations are performed to relate fracture strength to porosity. Often-times a 2D approximation over-simplifies the actual microstructure and results in inaccurate measurement of porosity. Diehl et al. [14] proposed 3D models of damage evolution around a single bubble and investigated the influence of the bubble geometry on the fracture response. 3D simulations provide important insights into the influence of porosity on fracture. In this chapter, a phase-field fracture model is employed to address intergranular cracking with multiple bubbles on the grain

boundaries in 3D and is used to model over-pressurized fission-gas-induced fragmentation at the microstructural level.

In HBS, following crack initiation, the cracks will fill with fission gas, and the crack surfaces will become pressurized. To account for pressurized crack surfaces, we present an extension of the quasi-brittle model by including regularized external work done by pressure into the total energy of the system. The regularized external work can be derived either based on a phase-field approximation of the sharp interface [15], or by modifying the free energy in a Biot system via an indicator function based on the phase-field [16]. In this chapter, the former approach is used to derive the phase-field model for brittle and quasi-brittle fracture with pressurized cracks.

3.2 Theory

3.2.1 Constitutive choices

Following the variational framework presented in Chapter 2, to account for elastic deformation and fracture in polycrystalline materials, the Helmholtz free energy density is decomposed as

$$\psi = \psi^e + \psi^f. \quad (3.1)$$

Recall that ψ^e is the strain energy density, and ψ^f is the fracture energy density.

Strain energy density

For small deformation elasticity considered in this chapter, the state variable Φ enters the strain energy density only through the infinitesimal strain tensor

$$\boldsymbol{\varepsilon} = \frac{1}{2} (\nabla \Phi + \nabla^T \Phi). \quad (3.2)$$

The material is assumed to be isotropic, characterized by the Lamé parameter λ and the shear modulus G . The strain energy density is defined as

$$\psi^e = g\psi_{\langle A \rangle}^e + \psi_{\langle I \rangle}^e, \quad (3.3a)$$

$$\psi_{\langle A \rangle}^e = \frac{1}{2}\lambda \langle \text{tr}(\boldsymbol{\varepsilon}) \rangle_+^2 + G\boldsymbol{\varepsilon}^+ : \boldsymbol{\varepsilon}^+, \quad (3.3b)$$

$$\psi_{\langle I \rangle}^e = \frac{1}{2}\lambda \langle \text{tr}(\boldsymbol{\varepsilon}) \rangle_-^2 + G\boldsymbol{\varepsilon}^- : \boldsymbol{\varepsilon}^-, \quad (3.3c)$$

where $g = \hat{g}(d)$ is the degradation function to be defined in Section 3.2.1, and $\boldsymbol{\varepsilon}^\pm$ denotes the positive or the negative part of the strain projected onto the spectrum associated with positive or negative eigenvalues. In the context of small deformation, the Cauchy stress $\boldsymbol{\sigma}$ can be viewed as the thermodynamic conjugate to the infinitesimal strain $\boldsymbol{\varepsilon}$, and can be written as

$$\boldsymbol{\sigma} = \psi_{,\boldsymbol{\varepsilon}}^e = g\boldsymbol{\sigma}_{\langle A \rangle} + \boldsymbol{\sigma}_{\langle I \rangle}, \quad (3.4a)$$

$$\boldsymbol{\sigma}_{\langle A \rangle} = \lambda \langle \text{tr}(\boldsymbol{\varepsilon}) \rangle_+ \mathbf{I} + 2G\boldsymbol{\varepsilon}^+, \quad (3.4b)$$

$$\boldsymbol{\sigma}_{\langle I \rangle} = \lambda \langle \text{tr}(\boldsymbol{\varepsilon}) \rangle_- \mathbf{I} + 2G\boldsymbol{\varepsilon}^-. \quad (3.4c)$$

Fracture energy density

With a sharp crack set Γ , the fracture energy is defined as $\Psi^f = \int_{\Gamma} \mathcal{G}_c \, dA$, where \mathcal{G}_c is the fracture toughness. An approximation of the sharp crack set using a phase-field can be written as

$$\Psi^f \approx \int_{\Omega_0} \mathcal{G}_c \gamma_l(d, \nabla d) \, dV, \quad (3.5)$$

where γ_l is often referred to as the crack surface density parameterized by a regularization length l . An Allen-Cahn type approximation can be expressed as

$$\gamma_l(d, \nabla d) = \frac{1}{c_0 l} (\alpha + l^2 \nabla d \cdot \nabla d), \quad (3.6)$$

where $\alpha = \hat{\alpha}(d)$ is the crack geometric function. According to the discussion in Chapter 2, existence requires $\hat{\alpha}(d)$ to be convex in d , and the phase-field irreversibility condition (2.6) assumes $\hat{\alpha}(d)$ attains its minimum at $d = 0$.

In the current variational framework, the fracture response, e.g. the critical fracture strength and the softening behavior, is determined by the crack geometric function and the degradation function. In this chapter, to model brittle fracture, where crack only nucleates at stress singularities, i.e. $\psi_c \rightarrow \infty$, the following combination of crack geometric function and degradation function is used,

$$\alpha = d^2, \quad g = (1 - d)^2. \quad (3.7)$$

To model quasi-brittle fracture in polycrystalline materials, where the post-fracture behavior can be characterized by certain softening law, the following combination is used,

$$\alpha = \xi d - (1 - \xi)d^2, \quad g = \frac{1}{1 + \phi}, \quad \phi = \frac{a_1 d + a_1 a_2 d^2 + a_1 a_2 a_3 d^3}{(1 - c)^p}, \quad (3.8)$$

where ψ_c is the critical fracture energy density, α is parameterized by ξ (ξ is conveniently its derivative at $d = 0$), and the degradation function g is parameterized by p , a_1 , a_2 and a_3 . Based on 1-D analyses, the optimal profile of the phase-field is controlled by ξ . For a given ξ , the approximated traction-separation law is determined by p , a_1 , a_2 and a_3 . In this chapter, the following parameters are chosen:

$$\xi = 2, \quad p = 2, \quad a_1 = \frac{\mathcal{G}_c}{c_0 l \psi_c}, \quad a_2 = -\frac{1}{2}, \quad a_3 = 0, \quad (3.9)$$

such that the phase-field is compactly supported by a constant half interfacial width of $D_u = \frac{\pi}{2}l$, and a linear traction-separation law is approximated with a slope of $-\frac{E\psi_c}{\mathcal{G}_c}$.

3.2.2 Approximation of the pressure boundary condition

Starting from the sharp representation of the crack set, the external power expenditure on the crack set due to pressure can be written as

$$\mathcal{P}^{\text{ext}} = \int_{\Gamma} \bar{p} \mathbf{n}_0 \cdot \dot{\Phi} \, dA, \quad (3.10)$$

where \bar{p} is the magnitude of the pressure. Following [15], the external work is approximated as per:

$$\begin{aligned} \mathcal{P}^{\text{ext}} &= \int_{\Omega_0} \rho^{\text{ext}} \, dV = \int_{\Omega_0} \bar{p} \left(-\frac{\nabla d}{\|\nabla d\|} \right) \cdot \dot{\Phi} \|\nabla I\| \, dV \\ &= \int_{\Omega_0} \bar{p} \left(-\frac{\nabla d}{\|\nabla d\|} \right) \cdot \dot{\Phi} \|\nabla d\| I_{,d} \, dV = - \int_{\Omega_0} \bar{p} \nabla d \cdot \dot{\Phi} I_{,d} \, dV \end{aligned} \quad (3.11)$$

where the surface normal \mathbf{n} is approximated using the gradient of the phase-field, and a crack indicator function $I(d) \in C^1([0, 1])$ is introduced so that the approximation respects the Γ -convergence properties.

Remark. Based on (3.11), the effective pressure approximated by the phase-field can be defined as:

$$\tilde{p} = \int_{\Omega_0} \frac{\partial \rho^{\text{ext}}}{\partial \dot{\Phi}} \cdot \left(-\frac{\nabla d}{\|\nabla d\|} \right) \, dV = \int_{\Omega_0} \bar{p} \|\nabla I\| \, dV \quad (3.12)$$

Assuming that $I(0) = 0$ and $I(1) = 1$, the proof of Γ -convergence can be sketched via the following method. Consider the approximated external power expenditure due to pressure (parameterized by the phase-field regularization length l). The phase-field profile can always be expressed by $d = \bar{d}(d_{\Gamma}(\mathbf{X})/l)$, where $d_{\Gamma}(\mathbf{X})$ is the unsigned distance function for the crack set Γ [17]. Substituting the phase-field profile into

(3.11) yields:

$$\begin{aligned}\mathcal{P}^{\text{ext}} &= - \int_{\Omega_0} \bar{p} \nabla \tilde{d} \cdot \dot{\Phi} I_d(\tilde{d}) \, dV = - \int_{\Omega_0} \bar{p} \nabla I \cdot \dot{\Phi} \, dV \\ &= - \int_{\Omega_0} \bar{p} \frac{dI}{d(d_\Gamma/l)} \frac{1}{l} \nabla d_\Gamma(\mathbf{X}) \cdot \dot{\Phi} \, dV.\end{aligned}\quad (3.13)$$

The domain integral can be converted to a set of path integrals along the level set (phase-field), using the co-area formula, as follows:

$$\mathcal{P}^{\text{ext}} = - \int_0^\infty \int_{\{\mathbf{X} \in \Omega_0, d_\Gamma(\mathbf{X}) = r\}} \bar{p} \frac{dI}{d(r/l)} \frac{1}{l} \nabla d_\Gamma(\mathbf{X}) \cdot \dot{\Phi} \, ds \, dr \quad (3.14)$$

A simple change of variables with $\tilde{r} = r/l$ yields:

$$\begin{aligned}\mathcal{P}^{\text{ext}} &= - \int_0^\infty \left(\int_{\{\mathbf{X} \in \Omega_0, d_\Gamma(\mathbf{X}) = r\}} \bar{p} \nabla d_\Gamma(\mathbf{X}) \cdot \dot{\Phi} \, ds \right) \frac{dI}{d(r/l)} \frac{1}{l} \, dr \\ &= - \int_0^\infty \left(\int_{\{\mathbf{X} \in \Omega_0, d_\Gamma(\mathbf{X}) = l\tilde{r}\}} \bar{p} \nabla d_\Gamma(\mathbf{X}) \cdot \dot{\Phi} \, ds \right) \frac{dI}{d\tilde{r}} \, d\tilde{r}\end{aligned}\quad (3.15)$$

Next, as the phase-field regularization length diminishes (i.e., $l \rightarrow 0$), the approximation of the pressure power expenditure converges to:

$$\lim_{l \rightarrow 0} \mathcal{P}^{\text{ext}} = - \int_0^\infty \frac{dI}{d\tilde{r}} \, d\tilde{r} \left[\int_{\Gamma^+} \bar{p}(-\mathbf{n}_0) \cdot \dot{\Phi} \, dA + \int_{\Gamma^-} \bar{p}(-\mathbf{n}_0) \cdot \dot{\Phi} \, dA \right] \quad (3.16a)$$

where it is apparent that the path integral along the level set converges to the surface integral on two opposite sides of the crack surface, while the gradient of the unsigned distance function converges to the normal on the crack surfaces Γ (i.e., $\lim_{l \rightarrow 0} \nabla d_\Gamma(\mathbf{X}) = -\mathbf{n}_0(\mathbf{X})$). Recall that the support of the phase-field depends on

the form of the crack geometric function α [17]; the integral shall be split according to the the ultimate phase-field half interfacial width D_u :

$$\begin{aligned}
& \lim_{l \rightarrow 0} \mathcal{P}^{\text{ext}} \\
&= - \left(\int_0^{D_u/l} \frac{dI}{d\tilde{r}} d\tilde{r} + \int_{D_u/l}^{\infty} \frac{dI}{d\tilde{r}} d\tilde{r} \right) \left[\int_{\Gamma^+} \bar{p}(-\mathbf{n}_0) \cdot \dot{\Phi} dA + \int_{\Gamma^-} \bar{p}(-\mathbf{n}_0) \cdot \dot{\Phi} dA \right] \\
&= - \left[I\left(\tilde{r} = \frac{D_u}{l}\right) - I(\tilde{r} = 0) \right] \left[\int_{\Gamma^+} \bar{p}(-\mathbf{n}_0) \cdot \dot{\Phi} dA + \int_{\Gamma^-} \bar{p}(-\mathbf{n}_0) \cdot \dot{\Phi} dA \right] \quad (3.17) \\
&= - [I(0) - I(1)] \left[\int_{\Gamma^+} \bar{p}(-\mathbf{n}_0) \cdot \dot{\Phi} dA + \int_{\Gamma^-} \bar{p}(-\mathbf{n}_0) \cdot \dot{\Phi} dA \right]
\end{aligned}$$

Finally, recall our previous restrictions on the indicator function $I(c)$; the limit reduces to:

$$\lim_{l \rightarrow 0} \mathcal{P}^{\text{ext}} = \int_{\Gamma^+} \bar{p}(-\mathbf{n}_0) \cdot \dot{\Phi} dA + \int_{\Gamma^-} \bar{p}(-\mathbf{n}_0) \cdot \dot{\Phi} dA. \quad (3.18)$$

3.2.3 Governing equations

Following the variational framework, substituting (3.1), (3.3a), (3.5), (3.6), and (3.11) into the problem statement (2.40), under the isothermal conditions, the governing equations can be obtained as

$$\nabla \cdot \boldsymbol{\sigma} - \bar{p} \nabla dI_{,d} = \mathbf{0}, \quad (3.19)$$

$$\nabla \cdot \boldsymbol{\xi} - f = 0, \quad (3.20)$$

supplemented by the constitutive relations (3.4a) and

$$\boldsymbol{\xi} = \frac{2\mathcal{G}_c l}{c_0}, \quad f = g_{,d} \psi_{\langle A \rangle}^e + \frac{\mathcal{G}_c}{c_0 l} \alpha_{,d}. \quad (3.21)$$

3.3 Verification

3.3.1 Uniaxial traction of a bar

We first verify the uniaxial response of the quasi-brittle fracture model with pressurization. Consider a bar of length $L = 400$ mm and width $W = 2$ mm that is subject to uniaxial tension. Plane strain conditions are assumed to hold. A similar example without crack pressurization can be found in [17]. Boundary conditions are shown in Figure 3.1. Both ends of the bar are subject to monotonically increasing horizontal displacements. Only a quarter of the domain is simulated utilizing the two symmetry conditions. The domain is uniformly discretized using QUAD4 elements, with 200 elements along the length and 1 element along the width. Included are the Young's modulus $E = 3 \times 10^4$ MPa, Poisson's ratio $\nu = 0.2$, critical fracture strength $\psi_c = 1.5 \times 10^{-4}$ mJ mm $^{-3}$, fracture toughness $\mathcal{G}_c = 0.12$ mJ mm $^{-2}$, and the Griffith's characteristic length $l_{ch} = \frac{\mathcal{G}_c}{2\psi_c} = 400$ mm.

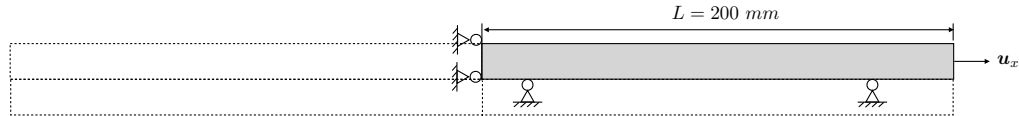


FIGURE 3.1. A bar under uniaxial tension.

FIGURE 3.2. Phase-field variable in initial conditions (for internal length scale $l = 20$ mm). The red and blue color correspond to value of 10^{-3} and 0, respectively.

An arbitrarily small imperfection, $d_0 = \mathcal{O}(\epsilon)$, is introduced on the left side of the computational domain to induce localization (Figure 3.2). To study the effect of the pressure, different pressure values

$$\bar{p} \in \{0.2 \text{ MPa}, 0.4 \text{ MPa}, 0.6 \text{ MPa}, 0.8 \text{ MPa}, 1 \text{ MPa}\}$$

are considered, with a fixed phase-field regularization length of $l = 20$ mm. In the context of fuel fracture, the pressure on the crack surfaces can result from a pressurized gas environment. The reaction force on the left boundary in Figure 3.3a shows that softening occurs simultaneously for different pressure values. With a larger pressure value, the damage grows more quickly. As is seen in Figure 3.3b, the reaction force on the right boundary is balanced with the prescribed pressure once the crack has fully developed. Figure 3.3c plots the approximated effective pressure \tilde{p} (3.12), which shows good agreement with prescribed values \bar{p} .

Wu [17] demonstrated that the numerical results are independent of the phase-field regularization length for a quasi-brittle fracture model without pressure [17]. Here, we consider a series of values of phase-field regularization length

$$l \in \{5 \text{ mm}, 10 \text{ mm}, 20 \text{ mm}, 50 \text{ mm}\}$$

with a fixed pressure of $\bar{p} = 0.4$ MPa. Figure 3.4 reveals the softening behaviors to be essentially the same, regardless of the chosen regularization length l . This feature allows for choosing \mathcal{G}_c and ψ_c values independently from the regularization length.

3.3.2 Pressurized crack propagation

Next, we verify fracture propagation conditions predicted by the quasi-brittle fracture model using a benchmark problem proposed by Wilson and Landis [18]. This problem serves to verify whether cracks should propagate once a critical pressure loading is applied. In Figure 3.5d, an initial crack is prescribed in the center with a length of $2a$. As shown in Figure 3.5a, the phase-field is initialized to be 1.0 only for those nodes on the bottom boundary belonging to the crack set, the phase-field variable is regularized to satisfy the governing equations, as shown in Figure 3.5b. Note that this differs from the approach suggested in [18, 19] which involves imposing initial values for a set of elements. Utilizing the symmetry, only half of the domain with

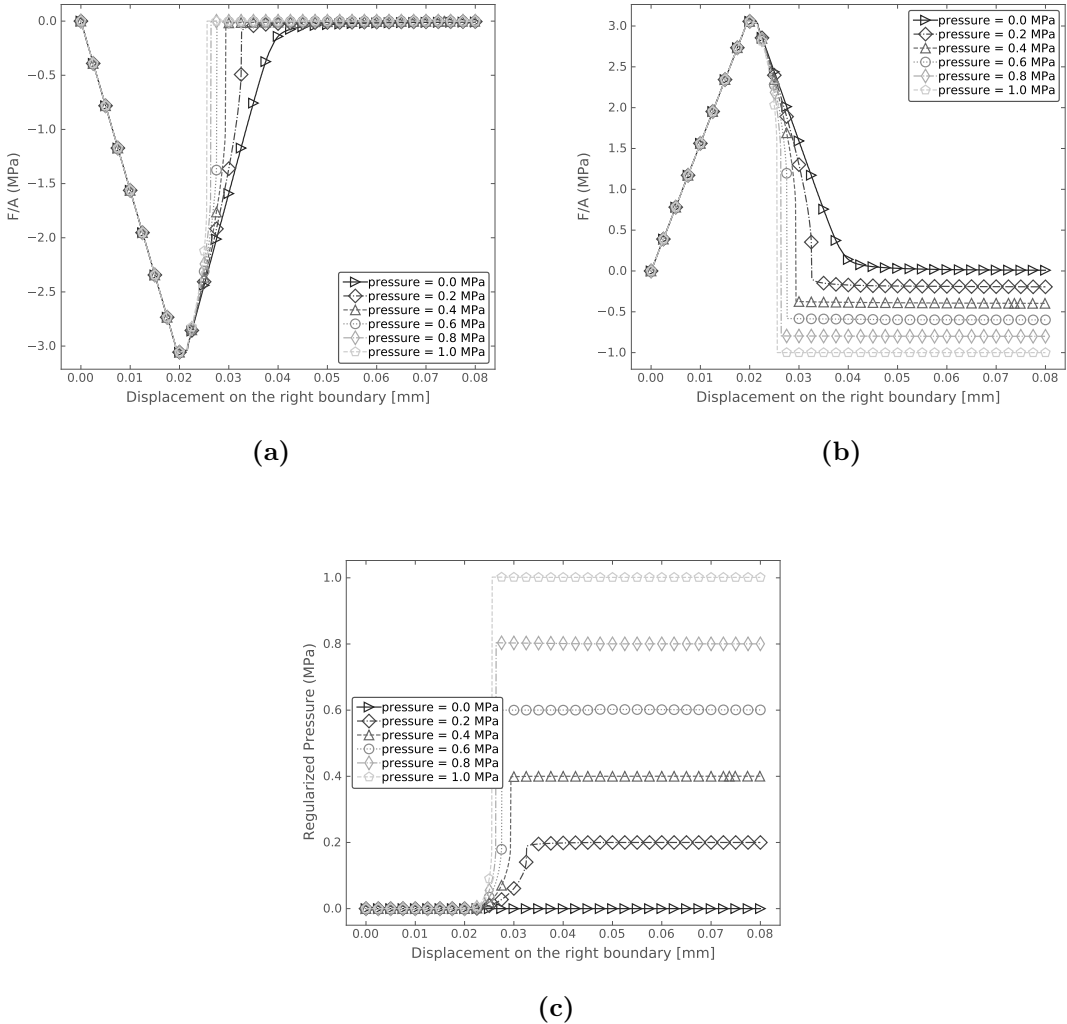


FIGURE 3.3. A bar under uniaxial tension with different pressure values \bar{p} : (a) Reaction force on the left boundary. (b) Reaction force on the right boundary. (c) Regularized pressure value.

size $L \times L/2$ is used (Figure 3.5c). The ratio L/a is taken to be 20. All outer surfaces are fixed. A prescribed pressure is increased until the crack starts to propagate. The propagation of the crack at fixed pressure conditions is unstable. According to the linear elastic fracture mechanics (LEFM) solution, the normalized critical pressure

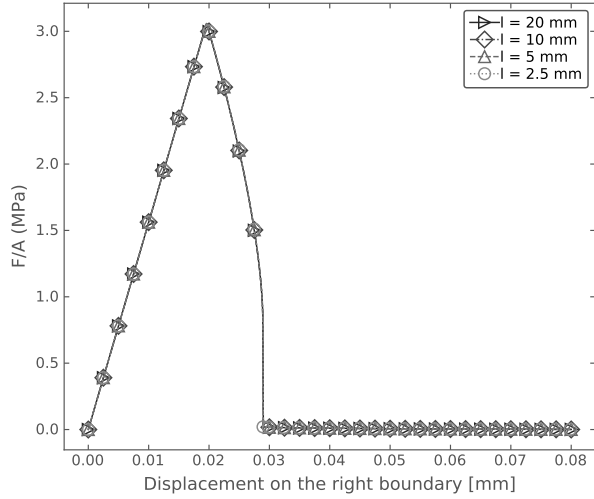


FIGURE 3.4. A bar under uniaxial tension with different internal lengths l .

is given as:

$$\frac{p_c}{\sigma_0} = \sqrt{\frac{l}{\pi a}}, \quad \sigma_0 = \sqrt{\frac{E}{(1 - \nu^2)} \frac{\mathcal{G}_c^{\text{eff}}}{l}}, \quad (3.22)$$

where $\mathcal{G}_c^{\text{eff}}$ is the effective fracture toughness in the phase-field fracture model and is given as [20, 19]:

$$\mathcal{G}_c^{\text{eff}} = \mathcal{G}_c \left(\frac{h}{4c_0 l} + 1 \right). \quad (3.23)$$

Note that the LEFM solution is based on a brittle fracture model. A comparison between the numerical results and the LEFM solution for the critical pressure values is shown in Figure 3.6. The phase-field solution converges as ψ_c increases, and shows good agreement with the LEFM solution.

3.4 Numerical examples

3.4.1 Predicting the critical fracture strength

This phase-field for brittle fracture model is readily applicable to three dimensional intergranular fracture. In this section, as an example, we simulate UO₂ intergranular

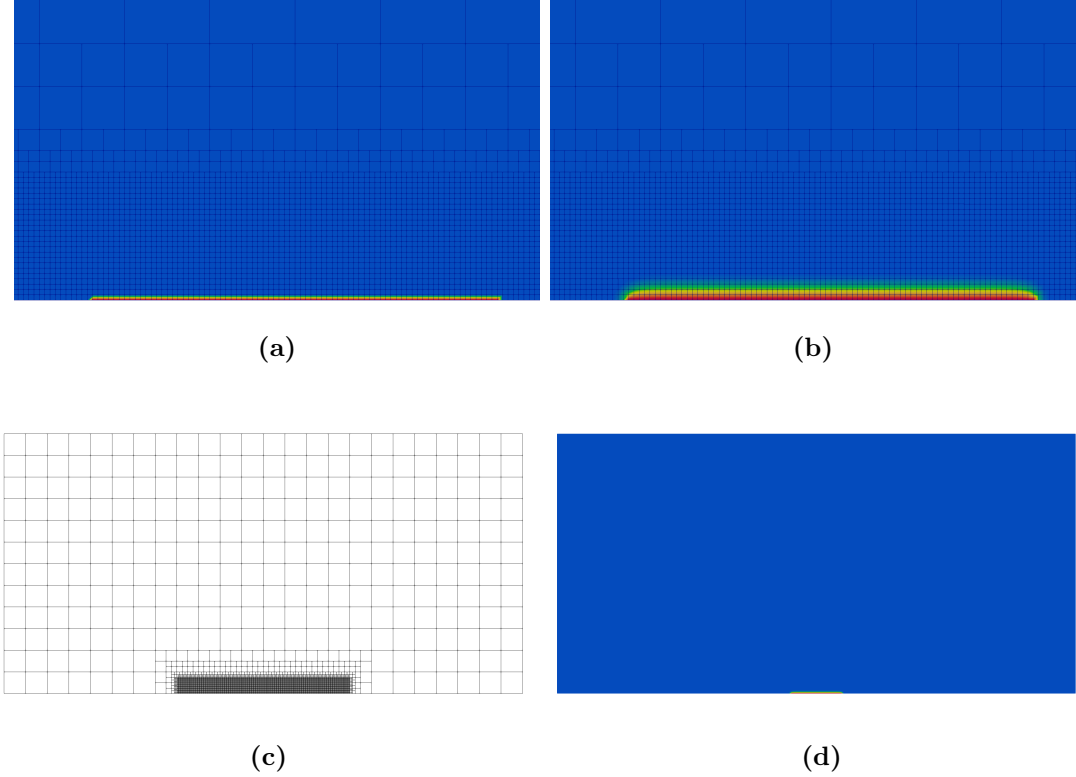


FIGURE 3.5. Pressurized crack propagation problem: (a) Initial values are imposed on crack surface nodes (zoomed view). (b) Regularized phase-field variable after one time step (zoomed view). (c) Mesh with five levels of local refinement. (d) Pre-existing crack. The red and blue color correspond to value of 1.0 and 0, respectively.

fracture and compare with experimental results. Material properties and model parameters are summarized in Table 3.3. We show how the presence of gas bubbles can alter the critical fracture strength of the specimen. The fracture toughness $G_c^b = 2 \times 10^{-3} \text{ mJ mm}^{-2}$ is calibrated based on Molecular Dynamics simulations [13], and is assumed to be homogeneous over the grain boundaries.

Without further calibration, to facilitate intergranular crack propagation, the fracture toughness of grain need to satisfy $G_c^g \gg G_c^b$ so that crack propagation is predominately driven by intergranular elastic energy. In this chapter, the polycrystalline microstructure is described by a set of non-conserved variables in a diffuse manner, obtained from a phase field grain growth model [22]. The phase-field $\phi_i = 1$

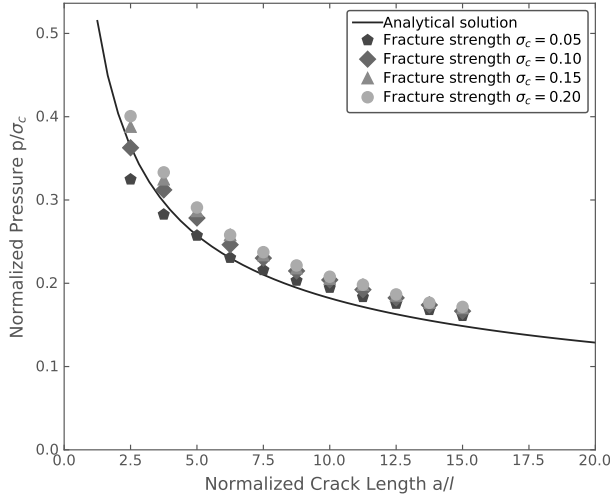


FIGURE 3.6. Comparison between the numerical results and the LEFM solution for the critical pressure values.

Table 3.1. Parameters and material properties used in the intergranular fracture simulations

Property	Symbol	Value	Unit	Reference
Young's modulus	E	385	GPa	[21]
Grain boundary fracture toughness	\mathcal{G}_c^b	0.002	mJ mm^{-2}	[13]
Grain fracture toughness	\mathcal{G}_c^g	0.01	mJ mm^{-2}	
Phase-field regularization length	l	0.5	μm	

within the i -th grain, and $\phi_i = 0$ elsewhere. Regions where ϕ_i varies between 0 and 1 correspond to grain boundaries. The grain boundaries are computed as $B = \sum \phi_i^2$.

The fracture toughness \mathcal{G}_c is then defined as

$$\mathcal{G}_c(\mathbf{X}) = \begin{cases} \mathcal{G}_c^b, & B(\mathbf{X}) < \bar{B}, \\ \mathcal{G}_c^g, & B(\mathbf{X}) \geq \bar{B}, \end{cases} \quad (3.24)$$

where \bar{B} is the threshold to distinguish between grains and grain boundaries. For simulations considered in this chapter, $\bar{B} = 0.75$ has been observed to be an appropriate choice. In this chapter, the elastic properties for the grain is assumed to be isotropic, e.g. independent of the crystal orientations. An arbitrarily small Young's

modulus of $10^{-9}E$ is assigned to the bubbles to remove zero energy modes. The domain is uniformly discretized with HEX8 elements with element size of $0.25\text{ }\mu\text{m}$.

Effect of gas bubble geometry

Gas bubbles on the grain boundaries act as crack initiators, and an accurate representation of their geometry is necessary to capture the stress concentration on the interface between the bubbles and the grain boundaries.

In equilibrium, gas bubbles on the grain boundaries have a lenticular shape. A 2D schematic of the lenticular bubble is shown in Figure 3.7a. The lenticular geometry is characterized by its length, thickness and dihedral angle. The dihedral angle is determined by the ratio of grain boundary energy to surface energy and it can vary over a wide range for UO_2 [23, 24].

To study the effect of gas bubble geometry on the critical fracture strength, three frequently adopted geometries are considered:

- (i) A lenticular gas bubble with length $22.4\text{ }\mu\text{m}$, thickness $16\text{ }\mu\text{m}$ and dihedral angle 142.6° .
- (ii) A lenticular gas bubble with length $22.4\text{ }\mu\text{m}$, thickness $10\text{ }\mu\text{m}$ and dihedral angle 96.6° .
- (iii) A spherical gas bubble with radius $7.9\text{ }\mu\text{m}$ which has the same volume as the lenticular gas bubble.

Consider a representative elementary volume (REV) with side length $120\text{ }\mu\text{m}$. The gas bubbles are placed over the grain boundaries such that the middle plane of the lenticular- or spherical- shaped bubbles are tangent to the grain boundaries. Symmetric boundary conditions are prescribed and a uniform displacement is applied on the top of the REV.

The variations in the critical fracture strength (Figure 3.7c) suggest that the shape of gas bubble affects the predicted fracture properties. A lenticular-shaped bubble has higher stress concentration at the edges of grain boundary bubbles, which lowers the critical fracture strength.

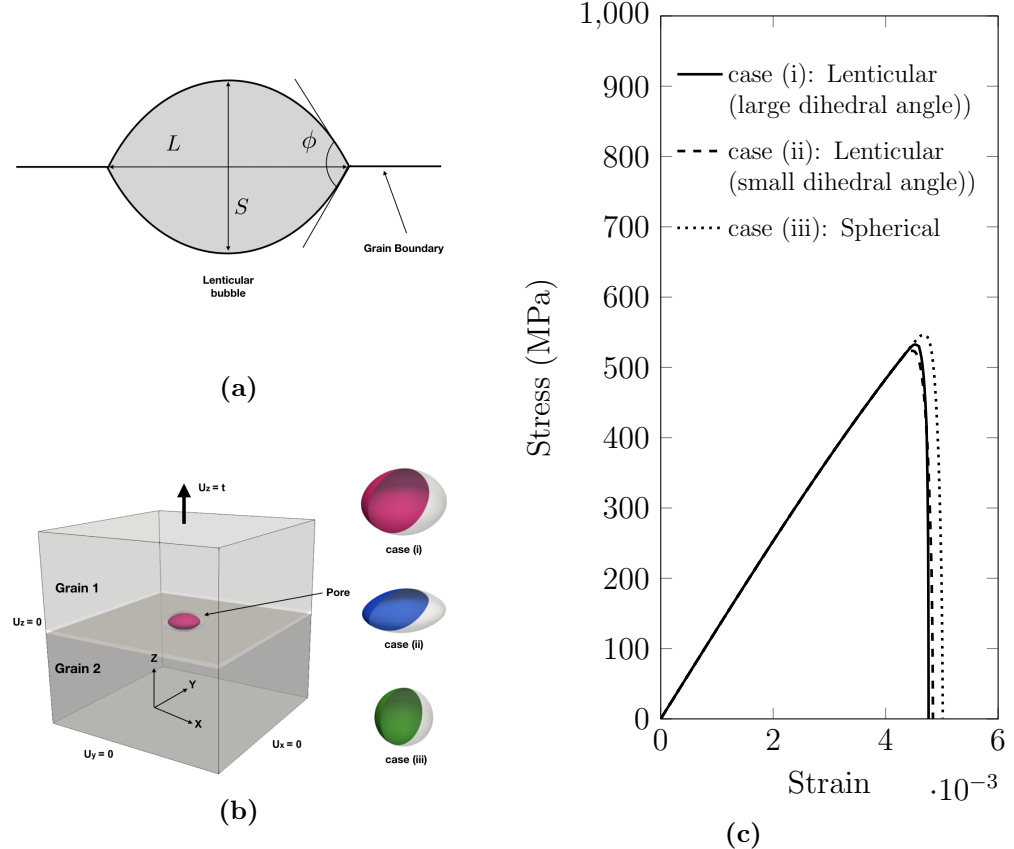


FIGURE 3.7. (a) The lenticular geometry is described by the length L , the thickness S and the dihedral angle ϕ . (b) Gas bubble geometry and boundary conditions. (c) Comparison of stress-strain curves for different gas bubble geometries.

Effect of loading

Next, we study the effect of different loading conditions. Uniaxial, biaxial and triaxial loading conditions are considered. The final crack configurations are shown in Figure 3.8. A change in crack path due to a different loading condition is evident from the figure. For uniaxial loading, cracks propagate along the grain boundaries

that are mainly perpendicular to the loading direction. For biaxial loading, crack branching occurs because biaxial loading results in two positive principal components of the strain tensor of the same order of magnitude. For triaxial loading, cracks propagate along all three directions.

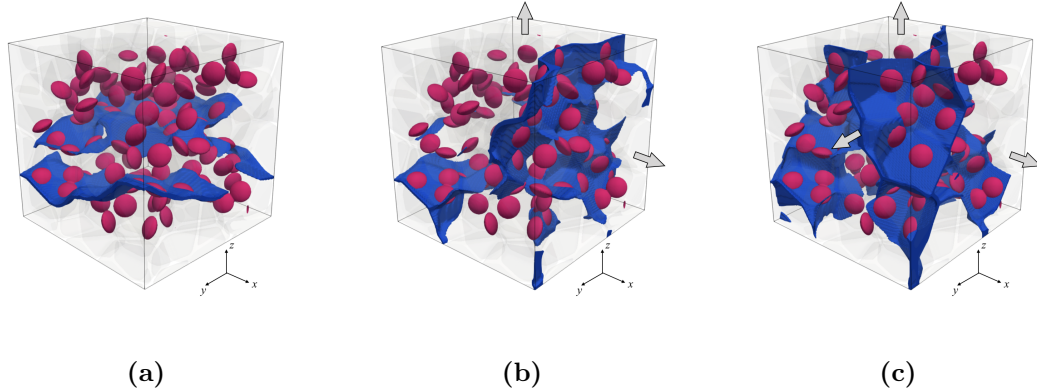


FIGURE 3.8. Final configuration (crack surfaces highlighted in blue) for different loading (a) uniaxial (b) biaxial (c) triaxial.

The stress-strain curves are shown in Figure 3.9. The difference in the slopes during loading is due to the Poisson's effect. The sample under the biaxial and triaxial loading conditions manifest a lower critical fracture strength compared to that under the uniaxial loading condition. The critical strain corresponding to the critical fracture strength under triaxial loading is about half of that under uniaxial loading.

Effect of porosity

In 2D, under plane-strain assumptions, the porosity represented by a planar bubble is computed by extruding it along the out-of-plane direction, which overestimates the actual porosity. In order to obtain a reasonable correlation between the critical fracture strength and the porosity, a 3D model is necessary.

To study the effect of porosity, consider an REV with side length 40 μm . Grain

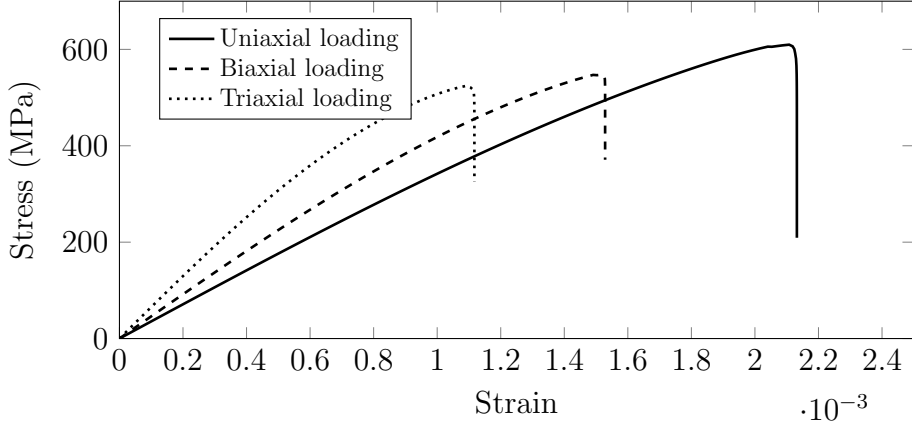


FIGURE 3.9. Comparison of stress-strain curves for different loading conditions.

centroids are generated from a random close-packing (RCP) voronoi structure. The RCP structures can be realized by a spatial sampling process known as Maximal Poisson-disk Sampling (MPS) [25]. For the RCP voronoi structure, the average aspect ratio of each voronoi cell is approximately 1 and an equiaxed grain structure is provided.

The influence of the voronoi structure on fracture properties can be isolated by considering a specific realization of RCP. The realization under consideration consists of 77 grains and the average radius of grains is $9.4 \mu\text{m}$. As shown in Figure 3.10, 50, 100 and 150 gas bubbles are randomly distributed over the grain boundaries, with corresponding porosity values 2.02%, 4.04% and 6.06%, respectively. All gas bubbles have a lenticular shape with $L = 6.4 \mu\text{m}$, $S = 4 \mu\text{m}$, and $\phi = 128^\circ$. Symmetric boundary conditions are prescribed and a uniform displacement is applied on the top of the RVE.

Final configurations of the approximated crack surfaces are shown in Figure 3.10, where, in general, cracks propagate perpendicular to the direction of the applied load.

It is worth noting that cracks keep propagating after initiation without any increase in the applied stress, which suggests that a snap-back is likely to take place

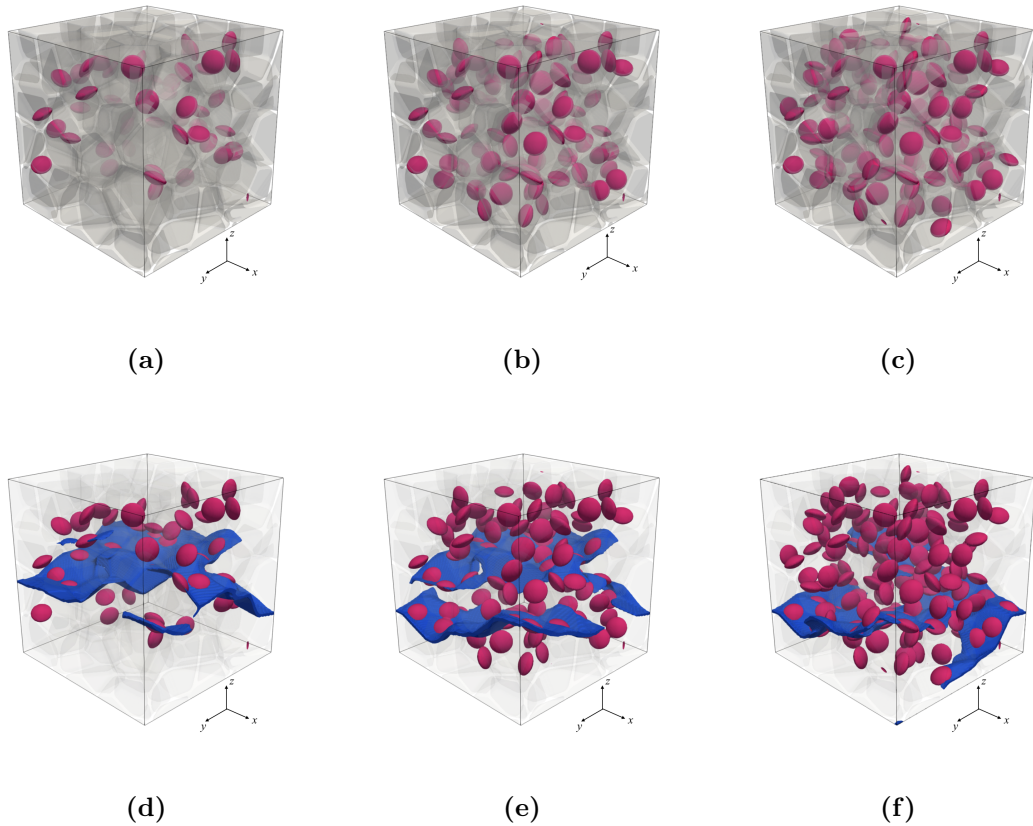


FIGURE 3.10. (a-c) Initial configuration of REVs with an average grain size of $9.4 \mu\text{m}$. (d-f) Final configuration (crack surfaces highlighted in blue) for REVs. Different porosity values are considered: (a, d) 2.02%, (b, e) 4.04%, (c, f) 6.06%.

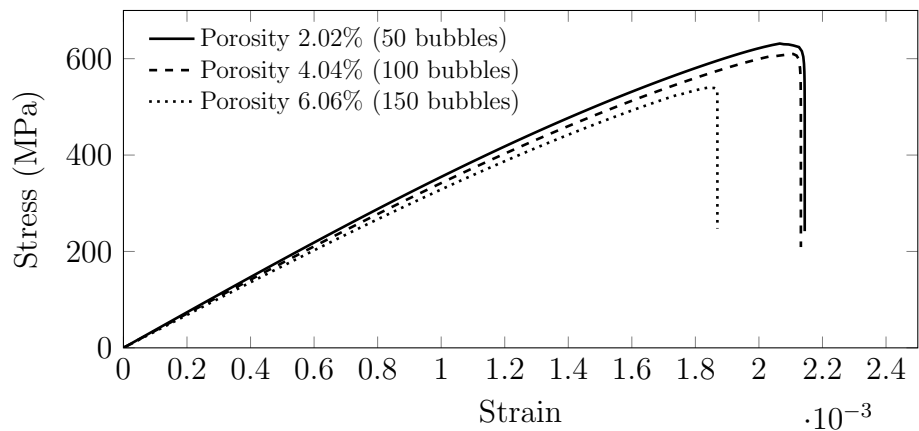


FIGURE 3.11. Comparison of stress-strain curves for different porosity values.

after crack initiation and a mixed force-displacement control is necessary to follow the actual stress-strain curve without loss of information. However, we argue that the a simple displacement control suffices to obtain the critical fracture strength – the maximum stress value along the stress-strain curve. From Figure 3.11, we conclude that an increase in porosity leads to a higher probability of crack initiation at lower stress state and consequently a decrease in the critical fracture strength.

To describe the porosity, average gas bubble and grain size effect on fracture strength, an exponential functional form obtained from biaxial flexure test has been reported in [26]:

$$\frac{\sigma_c}{\sigma_0} = \exp(-a \times \text{porosity}) \quad (3.25)$$

The critical fracture strength is normalized with respect to σ_0 . To benchmark with experiments, σ_0 is obtained by substituting the average grain and bubble size of 9.4 μm and 5.2 μm . To give proper error bounds on our numerical predictions, five trial calculations were performed on five different realizations of the spatial distribution of bubbles for each porosity level. The fracture strength obtained from 15 realizations of 3 porosity levels is summarized in Table 3.2. The obtained σ_0 is 198 MPa, 693 MPa and 697.8 MPa and the coefficient a is 0.057, 0.14 and 0.04, for experiment, 2D simulations and 3D simulations, respectively. A comparison of the experimental model, previous 2D simulations [13] and current 3D simulations is shown in Figure 3.12. In particular, the 95% confidence interval for the 3D simulations is shown in stripes. It shows that the 3D simulation has significant improvement towards the prediction of the dependence of the critical fracture strength on porosity. It is worth mentioning that the difference between simulation predictions of σ_0 and experimental values could be due to the fact that the transgranular fracture observed in experiments [27] has not been incorporated into the current numerical model.

Table 3.2. Summary of fracture strength obtained from 15 realizations of 3 porosity values. R denotes the realization index.

Porosity (%)	Critical fracture strength (MPa)				
	R1	R2	R3	R4	R5
2.02	631.4	657.4	645.6	663.4	630.7
4.04	609.8	555.6	605.5	611.2	589.2
6.06	540.0	530.8	557.0	563.2	567.9

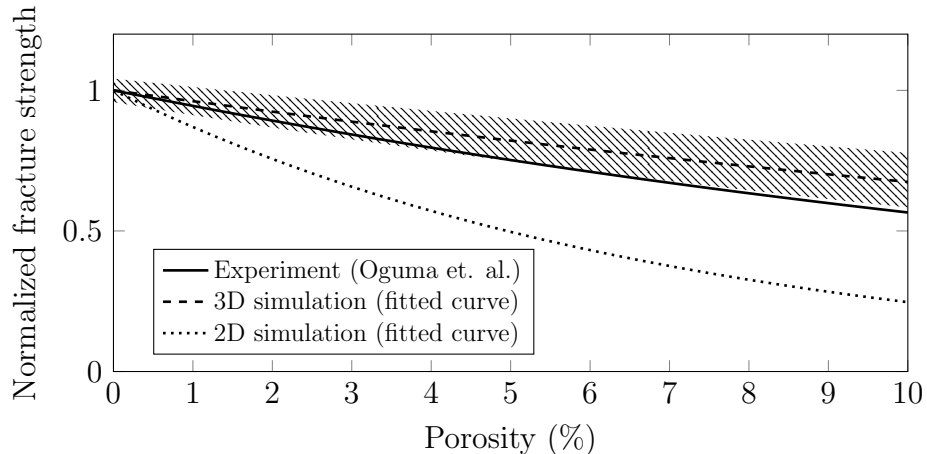


FIGURE 3.12. Variation in normalized fracture strength with changing porosity. In the current chapter, five trial calculations were performed for each porosity level, and each calculation was based on one realization of the spatial distribution of bubbles. The 95% confidence interval is shown in stripes.

3.4.2 High burnup structure fragmentation

Next, we adopt the quasi-brittle fracture model to simulate fission-gas-induced intergranular fracture of UO₂ HBS. A two-dimensional REV with side length $L = 3\text{ }\mu\text{m}$ is considered, and plane-strain conditions are assumed to hold. The material properties and model parameters are summarized in Table 3.3. The critical fracture energy of UO₂ is taken to be 0.022 mJ mm⁻³ [28]. Due to the lack of experimental data, the fracture toughness \mathcal{G}_c^g is assumed to be $1.2 \times 10^{-6}\text{ mJ mm}^{-3}$ and the Griffith's characteristic length $l_{ch} = \frac{\mathcal{G}_c}{2\psi_c} \approx 22.78\text{ nm}$. The domain is uniformly discretized with QUAD4 elements with element size of 0.005 μm.

Table 3.3. Parameters and material properties used in the fission-gas-induced HBS fracture simulations.

Property	Symbol	Value	Unit	Reference
Young's modulus	E	385	GPa	[21]
Critical fracture energy	ψ_c	0.022	mJ mm^{-3}	[28]
Grain boundary fracture toughness	\mathcal{G}_c^g	1.2×10^{-6}	mJ mm^{-3}	
Grain fracture toughness	\mathcal{G}_c^b	1.2×10^{-5}	mJ mm^{-3}	
Phase-field regularization length	l	0.01	μm	

LOCA pressure transients

We begin by investigating gas-pressure-induced fracture during LOCA-driven temperature transients. During a LOCA transient, temperatures in the fuel rod increase rapidly, leading to increased pressure in the gas contained within the bubbles. The temperature as a function of time at the edge of a representative pellet for each rod is obtained from simulation of the Studsvik Rod 196 experiment [29] using the engineering-scale fuel performance code BISON [30]. The temperature transient is used as an input to the Kim-Kim-Suzuki (KKS) phase-field model [31] to determine the pressure as a function of time. In the KKS model, the gas pressure is assumed to be 100 MPa during steady-state reactor operation at 700 K. The Studsvik experiment is initialized with a fixed temperature $T = 572.6$ K at the outer surface prior to the transient, resulting in a decrease in the pressure from 100 MPa to below 80 MPa. The pressure is assumed to be known in the quasi-brittle fracture model to simulate crack nucleation and propagation in the surrounding regions of the individual bubbles.

Two bubble radii ($0.25 \mu\text{m}$ and $0.5 \mu\text{m}$) are considered, and no loading is applied on the exterior. The resulting fracture patterns are shown in Figure 3.13. With the smaller bubble, two cracks propagate from the bubble towards the outer surface. With a larger bubble, only one major crack propagates to the free surface, and other minor cracks are arrested. Cracks nucleate when tensile stress on the bubble-matrix

interface reaches the critical fracture strength. The critical pressures are 120.17 MPa and 89.69 MPa for the small and large bubbles, respectively. The critical pressure is significantly lower for the larger bubble.

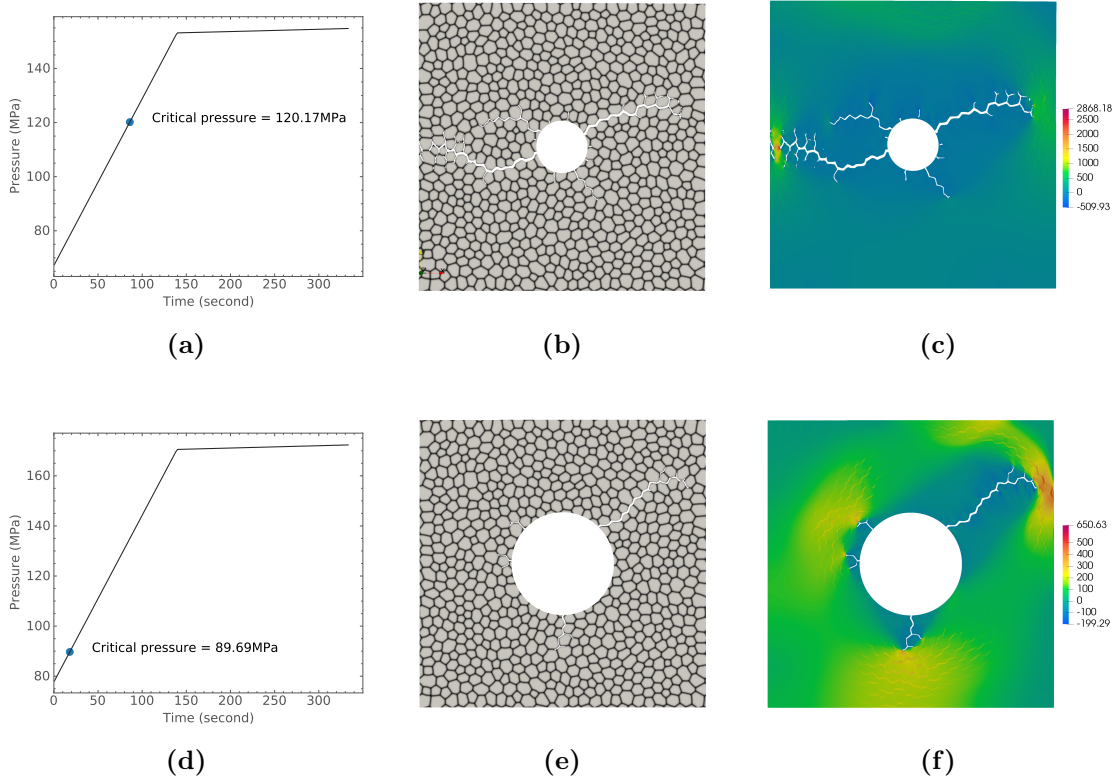


FIGURE 3.13. Results for (a-c) the small bubble with radius 0.25 μm and (d-f) the large bubble with radius 0.25 μm (a, d) Pressure history. (b, e) Crack paths superimposed on the voronoi structure. (c, f) Contour plot of the maximum principal stress.

In a fuel pellet system, external pressure can arise from fuel-cladding mechanical interaction. To study the effect of external pressure, different external pressures are applied on the top and right boundaries. The results from using three different external pressures, 0, 30 MPa, 60 MPa, are shown in Figure 3.14. The critical pressure is significantly higher for larger external pressure values, while there is no qualitative change in the crack pattern.

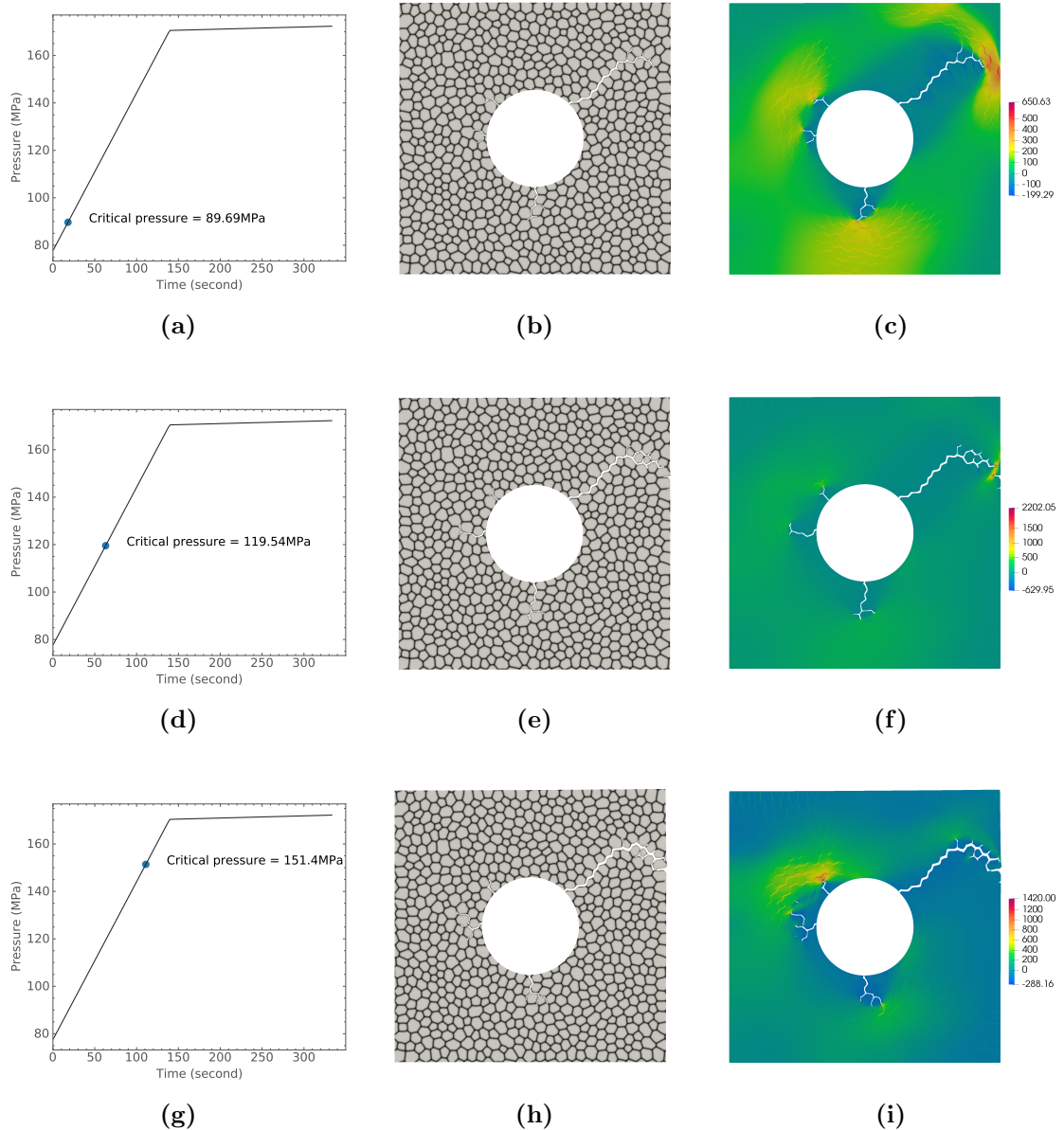


FIGURE 3.14. Results for bubble radius $0.5 \mu\text{m}$ and external pressure (a-c) 0 MPa, (d-f) 30 MPa, (g-i) 60 MPa. (a, d, g) Pressure history. (b, e, h) Crack paths superimposed on the voronoi structure. (c, f, i) Contour plot of the maximum principal stress.

Multi-bubble interaction

We next investigate the effect of the spatial distribution of the gas bubbles on fragment size. To that end, dimensions are expressed in dimensionless form in this

section. With the origin of the coordinate system placed at the lower left corner of the REV, two cases are considered:

- Two bubbles with centers at $\left(\frac{2}{15}L, \frac{7}{15}L\right)$ and $\left(\frac{7}{15}L, \frac{2}{15}L\right)$.
- Three bubbles with centers at $\left(\frac{1}{6}L, \frac{8}{15}L\right)$, $\left(\frac{8}{15}L, \frac{1}{6}L\right)$, and $\left(\frac{8}{15}L, \frac{8}{15}L\right)$.

All bubbles have a radius of $\frac{1}{12}L$. Results are shown in Figure 3.15. It is observed that the crack paths in cases involving multiple bubbles is strongly affected by the positions of the bubbles relative to each other: Cracks prefer to connect neighboring bubbles. Fully developed cracks and bubbles form a fragment at the lower-left corner in both cases. These fragments consist of multiple grains, and their sizes are affected by the spatial distribution of bubbles.

Partial HBS

Lastly, we incorporate defect evolution and recrystallization into the quasi-brittle fracture model. A phase-field model is used to simulate the defect evolution and the recrystallization behavior leading to HBS formation. A detailed description of the phase-field model is available in [31]. The quasi-brittle fracture model is applied directly on the microstructure resulting from simulations of the HBS formation process. Considering the fact that fragmentation can be observed in partially recrystallized zones, we focus on the fracture behavior of partial HBS. Three HBS at different recrystallization stages with 25%, 60%, and 100% recrystallization fraction are considered. A linearly increasing gas pressure is applied. Results are shown in Figure 3.16. In all three cases, cracks nucleate at around 60 MPa, owing to their similar defect sizes. Crack nucleation locations vary among the three cases, as more grains form around the defect during recrystallization and their intersections with

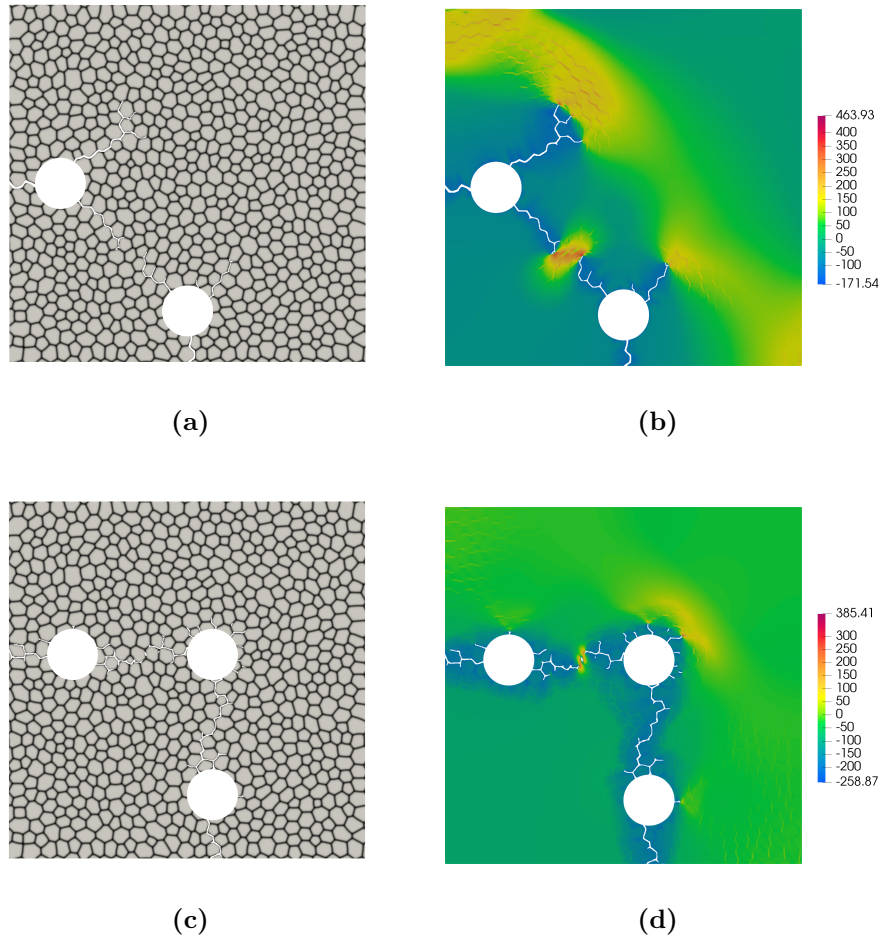


FIGURE 3.15. Results for (a-b) the two-bubble case and (c-d) the three-bubble case. (a, c) Crack paths superimposed on the voronoi structure. (b, d) Contour plot of the maximum principal stress.

the defect become possible nucleation sites. Furthermore, recrystallization changes the grain morphology, leading to different crack paths.

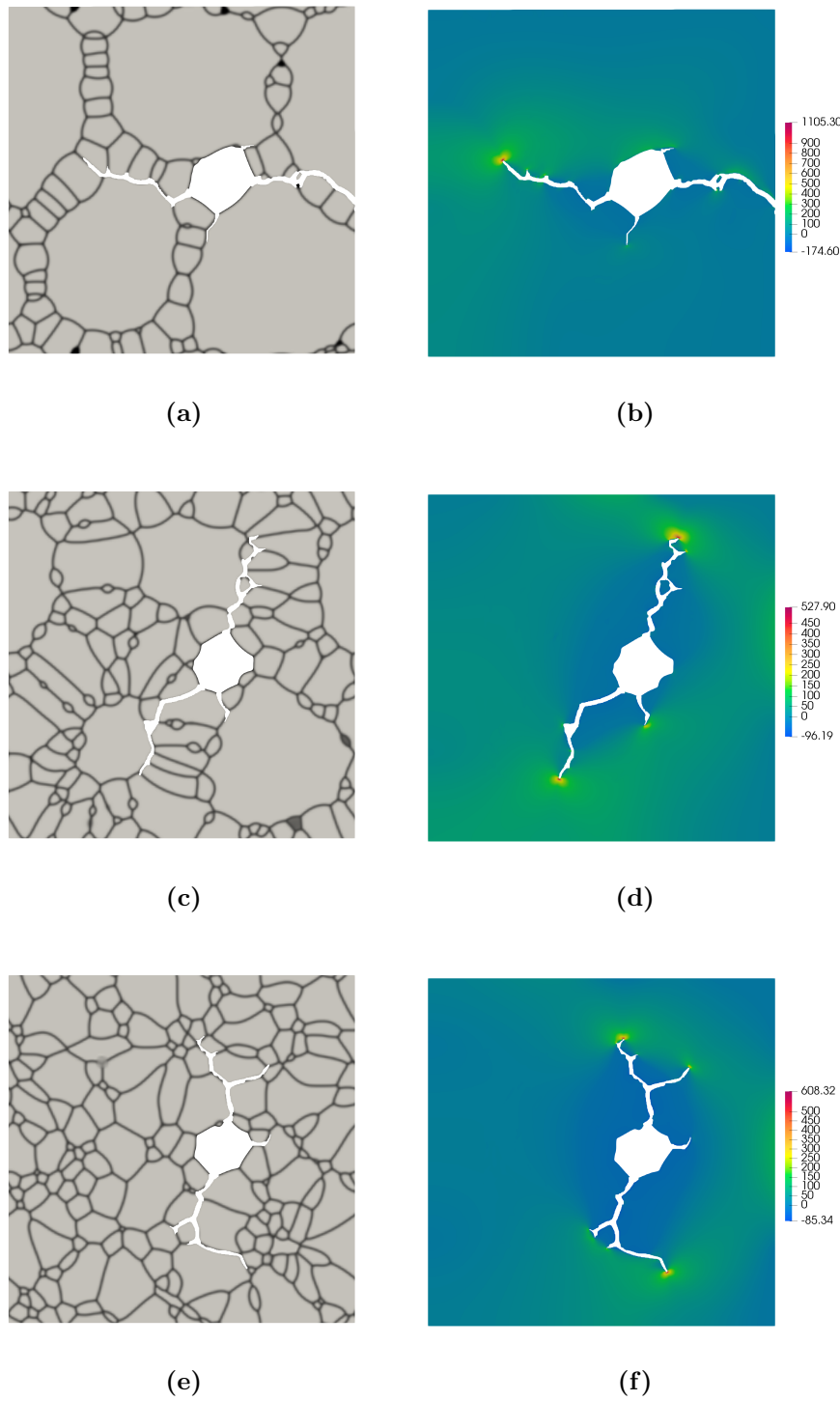


FIGURE 3.16. (a, c, e) Crack paths superimposed on the microstructure and (b, d, f) contour plots of the maximum principal stress assuming different recrystallization stages: (a-b) 25% recrystallization, (c-d) 60% recrystallization, (e-f) 100% recrystallization.

4

Cohesive Fracture: Soil Dessication

4.1 Introduction

In this work, a phase-field for cohesive fracture model is used to simulate pervasive cracking in thin films. A new elastic energy split is proposed to enforce frictionless contact conditions in the vicinity of diffuse fracture surfaces. In contrast to existing splits that have been proposed, our approach completely prevents tractions from being transmitted across fully damaged surfaces that are loaded in tension. Spatial variations of material properties are incorporated into our model, and we demonstrate, through forward analysis and by solving an inverse problem, how crack network morphology can be influenced by stochastic spatially-varying material properties.

The variational approach to fracture was proposed by Francfort and Marigo [32], and the phase-field implementation is attributed to Bourdin et al. [33]. Bourdin et al. [34] provides an overview. In the variational approach, crack surfaces are represented by a surface density function in terms of an auxiliary phase-field. This naturally gives rise to a regularization involving a length scale parameter. Such an

approach is known to be thermodynamically consistent and recent works have illustrated its potential to be predictive for a wide range of fracture problems. Phase-field for fracture models have succeeded in capturing complex crack patterns, including branching and coalescence in both two and three dimensions [35, 36, 37, 38, 39]. The approach has also been used to study the fracture of thin films, for example by Baldelli et al. [40, 41].

To prevent crack growth under compression, phase-field models of fracture typically employ some form of tension-compression asymmetric split in the elastic energy. Two popular approaches are the spectral decomposition [42, 43] and the volumetric-deviatoric decomposition [44]. Both the spectral decomposition and the volumetric-deviatoric decomposition are variational and lead to thermodynamically consistent fracture models. Although these variational approaches represent crack growth reasonably well for a broad range of problems, they do not completely preclude the transmission of tractions across fully damaged surfaces. In part, this is by design. The decompositions are designed to allow compressive tractions to be transmitted across fully damaged surfaces. But since they are developed from the full stress or strain as opposed to the surface tractions, they can also allow unwanted tensile or shear tractions to be transmitted. This can give rise to spurious macro-scale responses in some situations. Strobl and Seelig [45] proposed constitutive relations that satisfy the boundary conditions on diffuse crack surfaces by taking into account the crack orientation. Although the use of such a constitutive model violated the fundamental variational structure of phase-field models, it was shown to yield better results in some fracture problems [46]. A similar approach was presented by Fei and Choo [47, 48] to extend the model to better account for frictional contact conditions at crack surfaces. Finally, we mention the recent work of Lo et al. [49], in which the standard spectral split was modified to better guard against crack growth in compression.

In this work, we propose a variational elastic energy split that enforces frictionless contact conditions. Importantly, the split effectively prevents the transmission of tractions across fully-damaged surfaces that are loaded in tension. The proposed split leads to a decomposition that is shown to be important in mode II and mixed-mode fracture problems. The new phase-field model is then applied to study the classical problem of the fracture of thin films bonded to thick substrates. Due to the accumulation of inelastic strain and the stiffness mismatch between the film and the substrate, cracks form either transversely through the thickness of the film, referred to as “channeling”, or at the interface, referred to as “debonding”. Film-substrate systems exist across a wide span of application problems, from technological systems such as nuclear fuel pellet–cladding interactions (PCI) [50, 51, 52, 53, 54] to more common civil infrastructure examples such as pavement asphalts [55, 56, 57, 58, 59]. The study of fracture in these systems is driven by an interest in both understanding the underlying mechanisms and in preventing crack nucleation and evolution. In the current work, we confine attention to transverse channeling cracks in the film. When a system of cracks nucleate, branch and coalesce, complicated crack networks appear in the thin films. Hutchinson and Suo [60] provides a comprehensive review of crack patterns in film-substrate systems.

The fracture of thin films bonded to substrates has been studied using model-based simulations based on a wide range of methodologies. These problems are challenging to simulate because they involve pervasive crack nucleation, branching, and coalescence. Phenomenological spring models were developed and employed by Crosby and Bradley [61], Leung and Néda [62] and Sadhukhan et al. [63]. Zhang et al. [64] applied a cohesive zone method to study the film-substrate interface debonding, and Sánchez et al. [65] proposed a mesh fragmentation technique to simulate three-dimensional crack morphologies. Although such techniques are known to produce mesh-dependent results, the resulting crack networks were found to be satisfactory.

Liang et al. [66], Sukumar and Prévost [67] and Huang et al. [68] modeled thin film cracking using the eXtended Finite Element Method (XFEM) which allowed for the cracks to evolve independently of the finite-element mesh.

The aforementioned analytical and numerical efforts have provided a great deal of insight into the factors controlling the fracture of thin films. In particular, the mechanical properties that govern the spacing between cracks have been studied by Hutchinson and Suo [60], Xia and Hutchinson [69] and most recently by Yin et al. [70]. In contrast, the connection between spatial variations in material properties and the morphology of the resulting crack patterns has received fairly little attention. This is despite experimental evidence that crack morphologies are sensitive to spatial variations in material properties, see, e.g. Kitsunezaki et al. [71, 72], Halász et al. [73], Kitsunezaki et al. [74] and Nakahara et al. [75]. To our knowledge, while some previous model-based simulations of thin-film fracture have incorporated random material properties, they have not specifically considered spatial fluctuations and the construction of proper stochastic models. More broadly, the literature on probabilistic modeling for fracture simulations remains scarce. In [76], variability in fracture strength was estimated from multiscale simulations, and spatially-varying mesoscale properties were subsequently integrated into an asynchronous spacetime discontinuous Galerkin finite element based fracture model to study the impact on fragmentation. The integration of apparent elasticity coefficients in a multiscale-informed phase-field formulation was investigated in [77], with the aim of reproducing variability in the macroscopic response. The fracture toughness was modeled as deterministic and homogeneous, and was identified by solving an inverse problem. In [78], a continuum mapping of the meso-scale structure to the packing fraction at the macro-scale was employed to introduce a random component to phase-field simulations of surfactant-induced fracture of particle rafts. In this work, we construct a probabilistic model for the critical fracture energy and the fracture toughness, mod-

eled as (potentially correlated) random fields, and examine their influence on the random morphology of the resulting fracture patterns.

Our model-based simulations of thin-film fracture for systems with spatially-variable material properties are facilitated in this work through the adoption of an extension of phase-field models to cohesive fracture [79, 80, 81]. Phase-field for cohesive fracture models incorporate the original proposition by Xia and Hutchinson [69] regarding a “critical fracture energy”. The regularization length is decoupled from the material properties in these approaches, and the critical strength and the fracture toughness of the material are no longer strongly correlated. This independence permits simulations of drying in systems with realistic material properties for typical clays or soils, for example, without compromising the magnitude of the critical strength or requiring regularization lengths that are larger than the specimen dimensions. It also allows systems with spatially-variable fracture properties to be studied using a spatially-constant regularization length, greatly improving the fidelity of the numerical calculations.

This paper is organized as follows. ?? provides the theoretical background for phase-field models of fracture, the new decomposition, associated solution algorithms, and stochastic models for fracture properties. In ??, several numerical examples of benchmark problems in quasi-static fracture mechanics are provided to illustrate the efficacy of the new approach to enforcing frictionless contact conditions. The main results of this work are provided in ??, where the new model is used to study the formation of crack networks in thin films and in soil dessication problems. In particular, model-based simulations are used to examine how the fragment statistics and fracture morphologies are influenced by spatial variations in the fracture properties. Comparisons with both theory and experimental observations are provided. Finally, a summary and some concluding remarks are provided in the last section.

4.2 Theory

4.2.1 Constitutive choices

To solve the energy minimization problem, we first find the necessary conditions for the minimizer of the objective function by temporarily relaxing the constraint, i.e. by solving the unconstrained version as:

$$\min_{\mathbf{u}, d} \tilde{\Psi}_{\text{total}} = -\tilde{\Psi}_{\text{external}} + \tilde{\Psi}_{\text{internal}} + \tilde{\Psi}_{\text{fracture}}. \quad (4.1)$$

The Euler-Lagrange equations for this unconstrained minimization problem state that the minimizer satisfies:

$$-\nabla \cdot \frac{\delta \Psi_{\text{total}}}{\delta \nabla \mathbf{u}} + \frac{\delta \Psi_{\text{total}}}{\delta \mathbf{u}} + \frac{d}{dt} \frac{\delta \Psi_{\text{total}}}{\delta \dot{\mathbf{u}}} = \mathbf{0}, \quad (4.2a)$$

$$-\nabla \cdot \frac{\delta \Psi_{\text{total}}}{\delta \nabla d} + \frac{\delta \Psi_{\text{total}}}{\delta d} + \frac{d}{dt} \frac{\delta \Psi_{\text{total}}}{\delta \dot{d}} = 0. \quad (4.2b)$$

For the quasi-static fracture problems (under the small strain assumption) studied in this work, the total energy can be written in terms of displacements \mathbf{u} and damage d as:

$$\begin{aligned} \Psi_{\text{total}} = & - \underbrace{\left(\int_{\partial\Omega} \boldsymbol{\tau} \cdot \mathbf{u} \, dA + \int_{\Omega} \mathbf{b} \cdot \mathbf{u} \, dV \right)}_{\text{external energy}} + \underbrace{\int_{\Omega} g(d) \psi_{\text{elastic}}^{(A)} \, dV + \int_{\Omega} \psi_{\text{elastic}}^{(I)} \, dV}_{\text{degraded elastic energy}} \\ & + \underbrace{\int_{\Omega} \frac{\mathcal{G}_c}{c_0 l} (w(d) + l^2 \|\nabla d\|^2) \, dV}_{\text{approx. fracture energy}}, \end{aligned} \quad (4.3)$$

where $\boldsymbol{\tau}$ is the surface traction and \mathbf{b} is the body force. Substituting the total energy into the Euler-Lagrange equations, we obtain the necessary conditions of the minimizer, which are essentially the governing equations of the given system together

with boundary conditions:

$$-\boldsymbol{\nabla} \cdot \tilde{\boldsymbol{\sigma}} - \mathbf{b} = \mathbf{0}, \quad \text{in } \Omega, \quad (4.4)$$

$$-\boldsymbol{\nabla} \cdot \boldsymbol{\xi} + Mw'(d) + g'(d)\psi_{\text{elastic}}^{\langle A \rangle} = 0, \quad \text{in } \Omega, \quad (4.5)$$

$$\tilde{\boldsymbol{\sigma}} \cdot \mathbf{n} = \boldsymbol{\tau}, \quad \text{on } \partial\Omega, \quad (4.6)$$

$$\boldsymbol{\xi} \cdot \mathbf{n} = 0, \quad \text{on } \partial\Omega, \quad (4.7)$$

with constitutive relations

$$\tilde{\boldsymbol{\sigma}} = g(d) \frac{\delta \psi_{\text{elastic}}^{\langle A \rangle}}{\delta \boldsymbol{\nabla} \mathbf{u}} + \frac{\delta \psi_{\text{elastic}}^{\langle I \rangle}}{\delta \boldsymbol{\nabla} \mathbf{u}}, \quad (4.8)$$

$$\boldsymbol{\xi} = M\kappa \boldsymbol{\nabla} d + g(d) \frac{\delta \psi_{\text{elastic}}^{\langle A \rangle}}{\delta \boldsymbol{\nabla} d} + \frac{\delta \psi_{\text{elastic}}^{\langle I \rangle}}{\delta \boldsymbol{\nabla} d}, \quad (4.9)$$

where $\tilde{\boldsymbol{\sigma}}$ is the degraded stress tensor, $\boldsymbol{\xi}$ is the thermodynamic conjugate to $\boldsymbol{\nabla} d$ (the dependence of $\psi_{\text{elastic}}^{\langle A \rangle}$ and $\psi_{\text{elastic}}^{\langle I \rangle}$ on $\boldsymbol{\nabla} d$ is defined in ??), $\kappa = 2l^2$ is the interfacial coefficient, and $M = \frac{g_c}{c_0 l}$ is often referred to the mobility in keeping with general Allen-Cahn phase-field models. According to (??), and due to the fact that $\boldsymbol{\xi}|_{d=0} = \mathbf{0}$, the damage begins to accumulate as soon as:

$$\psi_{\text{elastic}}^{\langle A \rangle} > \psi_c = -M \frac{w'(0)}{g'(0)}, \quad (4.10)$$

where ψ_c is a model-specific energy threshold for damage initiation. For example, a brittle fracture model that uses $w(d) = d^2$ results in a critical energy $\psi_c = 0$, and cohesive-type fracture models that use $w(d) = d$ have a critical energy $\psi_c = -M/g'(0)$. In this work, we adopt a cohesive fracture model that uses the local dissipation function $w(d) = d$ in conjunction with the degradation function proposed by Lorentz [82, 83] such that the critical fracture energy is not necessarily correlated with the other material properties and model parameters, i.e. the fracture toughness

\mathcal{G}_c and the length scale l :

$$g(d; p \geq 1) = \frac{(1-d)^2}{(1-d)^2 + \frac{M}{\psi_c} d(1+pd)}, \quad (4.11)$$

where p controls the size of the fracture process zone and is chosen to be 1 in this work.

4.2.2 Enforcing the traction-free boundary condition

For quasi-static mechanical-fracture coupling, the energy balance and thus the corresponding energy minimization problem can be instantiated as:

$$\begin{aligned} & \min_{u,d} \left(-\tilde{\Psi}_{\text{external}}|_{\Omega,\partial\Omega} + \tilde{\Psi}_{\text{internal}}|_{\Omega} + \tilde{\Psi}_{\text{fracture}}|_{\Omega} \right), \\ & \text{subject to } \dot{d} \geq 0. \end{aligned} \quad (4.12)$$

A typical assumption in fracture mechanics is that only tensile/expansive components of the elastic energy contribute to crack initiation and growth. Therefore, the degraded elastic energy is often split into an active part that is coupled with fracture, and an inactive part that is independent of fracture. According to the split of elastic energy, we have:

$$\tilde{\Psi}_{\text{elastic}} = \int_{\Omega} g(d) \psi_{\text{elastic}}^{\langle A \rangle} \, dV + \int_{\Omega} \psi_{\text{elastic}}^{\langle I \rangle} \, dV. \quad (4.13)$$

Widely used active/inactive splits are spectral split [42, 43] and volumetric-deviatoric split [39]. Unfortunately, neither the spectral split nor the volumetric-deviatoric split completely prevent tensile or shear tractions from being transmitted across fully-damaged surfaces. Accordingly, we now develop a split that is motivated by the consideration of frictionless contact conditions along fully damaged surfaces.

We begin by recalling the standard Kuhn-Tucker optimality conditions for frictionless contact under small deformation, which can be written as

$$t_N \geq 0, \quad u_I \leq 0, \quad t_N u_I = 0, \quad (4.14)$$

where t_N is the contact pressure and u_I denotes the interpenetration between the contact surfaces. The contact pressure is typically obtained from the stress and the unit outward normal to the contact surface. In regularized models of fracture, however, it can be difficult to identify a unique surface based on the damage field. Accordingly, we rely on the gradient of the damage field to construct an approximate normal $\tilde{\mathbf{n}}$, viz.

$$\tilde{\mathbf{n}} = \frac{\nabla d}{\|\nabla d\|}, \quad (4.15)$$

and calculate the normal pressure as

$$t_N = -\tilde{\mathbf{n}} \cdot \boldsymbol{\sigma} \cdot \tilde{\mathbf{n}}. \quad (4.16)$$

Our split keys off the sign of the normal pressure, by isolating the cases of a positive pressure (for contact) from a negative pressure (for opening). In particular, we construct a “normal-tangential” stress decomposition of the form

$$\boldsymbol{\sigma} = \boldsymbol{\sigma}_n^+ + \boldsymbol{\sigma}_n^- + \boldsymbol{\sigma}_t, \quad (4.17)$$

where

$$\boldsymbol{\sigma}_n^\pm = \langle -t_N \rangle_\pm \tilde{\mathbf{n}} \otimes \tilde{\mathbf{n}}, \quad \boldsymbol{\sigma}_t = \boldsymbol{\sigma} - \boldsymbol{\sigma}_n^+ - \boldsymbol{\sigma}_n^-, \quad (4.18)$$

with $\langle -t_N \rangle_\pm := (-t_N \pm |-t_N|)/2$ denoting a signed version of the standard Macaulay bracket.

In the vicinity of the regularized crack surface, we then propose the use of a stress-based elastic energy split, hereafter referred to as the *contact split*, that takes

the form:

$$\psi_{\text{elastic}} = \psi_{\text{elastic}}^{\langle A \rangle} + \psi_{\text{elastic}}^{\langle I \rangle}, \quad (4.19a)$$

$$\psi_{\text{elastic}}^{\langle A \rangle} = \frac{1}{2} \boldsymbol{\sigma}^{\langle A \rangle} : \boldsymbol{\varepsilon}, \quad \psi_{\text{elastic}}^{\langle I \rangle} = \frac{1}{2} \boldsymbol{\sigma}^{\langle I \rangle} : \boldsymbol{\varepsilon}, \quad (4.19b)$$

$$\boldsymbol{\sigma}^{\langle A \rangle} = \boldsymbol{\sigma}_n^+ + \boldsymbol{\sigma}_t, \quad \boldsymbol{\sigma}^{\langle I \rangle} = \boldsymbol{\sigma}_n^-. \quad (4.19c)$$

The corresponding constitutive relation follows as:

$$\tilde{\boldsymbol{\sigma}} = \frac{\delta \tilde{\psi}_{\text{elastic}}}{\delta \boldsymbol{\varepsilon}} = g(d) \frac{\delta \psi_{\text{elastic}}^{\langle A \rangle}}{\delta \boldsymbol{\varepsilon}} + \frac{\delta \psi_{\text{elastic}}^{\langle I \rangle}}{\delta \boldsymbol{\varepsilon}}, \quad (4.20a)$$

$$= g(d) \frac{\delta}{\delta \boldsymbol{\varepsilon}} \left(\frac{1}{2} \boldsymbol{\sigma}^{\langle A \rangle} : \boldsymbol{\varepsilon} \right) + \frac{\delta}{\delta \boldsymbol{\varepsilon}} \left(\frac{1}{2} \boldsymbol{\sigma}^{\langle I \rangle} : \boldsymbol{\varepsilon} \right), \quad (4.20b)$$

$$= g(d) \boldsymbol{\sigma}^{\langle A \rangle} + \boldsymbol{\sigma}^{\langle I \rangle}, \quad (4.20c)$$

and

$$\boldsymbol{\xi} = M\kappa \boldsymbol{\nabla} d + g(d) \frac{\delta \psi_{\text{elastic}}^{\langle A \rangle}}{\delta \boldsymbol{\nabla} d} + \frac{\delta \psi_{\text{elastic}}^{\langle I \rangle}}{\delta \boldsymbol{\nabla} d}, \quad (4.21)$$

where

$$\frac{\delta \psi_{\text{elastic}}^{\langle A \rangle}}{\delta \boldsymbol{\nabla} d} = - \frac{\delta \psi_{\text{elastic}}^{\langle I \rangle}}{\delta \boldsymbol{\nabla} d} = \frac{1}{\|\boldsymbol{\nabla} d\|} [2 \langle -t_N \rangle_- \varepsilon_N \tilde{\mathbf{n}} - H(t_N) \varepsilon_N \boldsymbol{\sigma} \cdot \tilde{\mathbf{n}} - \langle -t_N \rangle_- \boldsymbol{\varepsilon} \cdot \tilde{\mathbf{n}}],$$

$$(4.22)$$

and H denotes the Heaviside function.

It bears emphasis that the proposed elastic energy split only serves to enforce the crack surface traction free boundary condition, and it is not reasonable to expect it to reliably govern crack nucleation and growth. In the present work, to ensure that such a normal-tangential split is applied only in the vicinity of the crack surface, we impose a simple threshold d_{critical} such that we apply

$$\begin{cases} \text{the contact split (4.19a) to (4.20c), } d \geq d_{\text{critical}} \\ \text{the strain-based spectral split [42, 43], } d < d_{\text{critical}}. \end{cases}$$

Remark. Alternative to a threshold, in principle a total energy could be constructed using a blending function that transitions between a standard split and the contact split.

It can be shown that the definition of the contact pressure (4.16) follows by relaxing the frictionless constraint into a minimization problem, and t_N is therefore the best scalar quantity one can choose to approximate the traction-free boundary condition:

$$\min_{t_N} \|\boldsymbol{\sigma}_t(t_N) \cdot \tilde{\mathbf{n}}\|^2 \quad (4.23a)$$

$$= \|(\boldsymbol{\sigma} - \langle -t_N \rangle_+ \tilde{\mathbf{n}} \otimes \tilde{\mathbf{n}} - \langle -t_N \rangle_- \tilde{\mathbf{n}} \otimes \tilde{\mathbf{n}}) \cdot \tilde{\mathbf{n}}\|^2 \quad (4.23b)$$

$$= \|(\boldsymbol{\sigma} + t_N \tilde{\mathbf{n}} \otimes \tilde{\mathbf{n}}) \cdot \tilde{\mathbf{n}}\|^2 \quad (4.23c)$$

$$= t_N^2 + 2t_N \tilde{\mathbf{n}} \cdot \boldsymbol{\sigma} \cdot \tilde{\mathbf{n}} + \|\boldsymbol{\sigma} \cdot \tilde{\mathbf{n}}\|^2, \quad (4.23d)$$

and the minimizer is

$$t_N = \arg \min_{t_N} (t_N^2 + 2t_N \tilde{\mathbf{n}} \cdot \boldsymbol{\sigma} \cdot \tilde{\mathbf{n}} + \|\boldsymbol{\sigma} \cdot \tilde{\mathbf{n}}\|^2) = -\tilde{\mathbf{n}} \cdot \boldsymbol{\sigma} \cdot \tilde{\mathbf{n}}. \quad (4.24)$$

4.2.3 Stochastic models for fracture properties

In the current work, we allow for material property inhomogeneity in the macroscopic continuum model. Specifically, we introduce the random field $\{\boldsymbol{P}(\mathbf{x}) = (P_1(\mathbf{x}), P_2(\mathbf{x})), \mathbf{x} \in \Omega\}$ defined on the probability space (Θ, Σ, P) , indexed by Ω and with values in $\mathbb{R}_{>0} \times \mathbb{R}_{>0}$, such that $\{P_1(\mathbf{x}), \mathbf{x} \in \Omega\}$ (respectively $\{P_2(\mathbf{x}), \mathbf{x} \in \Omega\}$) is a prior representation of $\{\mathcal{G}_c(\mathbf{x}), \mathbf{x} \in \Omega\}$ (respectively $\{\psi_c(\mathbf{x}), \mathbf{x} \in \Omega\}$). Due to the restrictions on the state space, the bivariate random field $\{\boldsymbol{P}(\mathbf{x}), \mathbf{x} \in \Omega\}$ is non-Gaussian. In order to model nongaussianity, the random field $\{\boldsymbol{P}(\mathbf{x}), \mathbf{x} \in \Omega\}$ is *defined* as

$$\boldsymbol{P}(\mathbf{x}) := \mathcal{T}(\boldsymbol{\Xi}(\mathbf{x}), \mathbf{x}), \quad \forall \mathbf{x} \in \Omega, \quad (4.25)$$

where \mathcal{T} is a measurable, nonlinear mapping and $\{\boldsymbol{\Xi}(\mathbf{x}), \mathbf{x} \in \Omega\}$ is a centered Gaussian random field with values in \mathbb{R}^2 to be defined momentarily. From a method-

ological standpoint, it should be noticed that the transformation \mathcal{T} is constructed *a priori* and used to define $\{\mathbf{P}(\mathbf{x}), \mathbf{x} \in \Omega\}$ such that the latter constitutes a surrogate capturing some essential features of $\{(\mathcal{G}_c(\mathbf{x}), \psi_c(\mathbf{x})), \mathbf{x} \in \Omega\}$ (while exhibiting a low dimensional parameterization). In general, the existence of a nonlinear mapping \mathcal{T} such that (4.25) holds for a *given* non-Gaussian field is not guaranteed; see, e.g., [84].

Construction of the Non-Gaussian Model

In this work, the transformation \mathcal{T} is constructed by imposing the family $\{f_{\mathbf{x}}\}_{\mathbf{x} \in \Omega}$ of first-order marginal distributions:

$$P_{\mathbf{P}(\mathbf{x})}(d\mathbf{p}) = f_{\mathbf{x}}(\mathbf{p})d\mathbf{p}, \quad \forall \mathbf{x} \in \Omega, \quad (4.26)$$

where $f_{\mathbf{x}}$ is the probability density function of $\mathbf{P}(\mathbf{x})$, \mathbf{x} being fixed in Ω , and $d\mathbf{p} = dp_1dp_2$ is the Lebesgue measure in \mathbb{R}^2 . It is assumed that $f_{\mathbf{x}}(\cdot) = f(\cdot; \mathbf{w}_{\mathbf{x}})$, where $\mathbf{w}_{\mathbf{x}}$ is a vector-valued hyperparameter indexed by $\mathbf{x} \in \Omega$. In order to simplify the analysis, we assume from now on that the aforementioned hyperparameter does not depend on location, and we write $f_{\mathbf{x}}(\cdot) = f(\cdot; \mathbf{w})$ using a slight abuse of notation.

The construction of f can be achieved in many different ways. In what follows, the construction is performed by assuming that (i) \mathcal{G}_c and ψ_c (together with their inverses) are positive and have finite variance, for physical consistency, and (ii) the two fracture properties can exhibit some level of correlation. In accordance with information theory [85, 86] and more precisely, with the principle of maximum entropy [87, 88], the first assumption leads to the consideration of Gamma marginal distributions. Following the notation introduced above, we shall impose that

$$P_{P_1(\mathbf{x})}(dp_1) = f_{\mathcal{G}}(p_1; (\underline{p}_1, \delta_1))dp_1, \quad \forall \mathbf{x} \in \Omega, \quad (4.27)$$

and

$$P_{P_2(\mathbf{x})}(dp_2) = f_{\mathcal{G}}(p_2; (\underline{p}_2, \delta_2))dp_2, \quad \forall \mathbf{x} \in \Omega, \quad (4.28)$$

where $f_{\mathcal{G}}(\cdot; (\underline{p}, \delta))$ denotes the univariate Gamma probability density function with mean \underline{p} and coefficient of variation δ . In this setting, the joint distribution of $\mathbf{P}(\mathbf{x})$ must be constructed from the knowledge of the marginal laws associated with $P_1(\mathbf{x})$ and $P_2(\mathbf{x})$. This ill-posed problem does not admit a unique solution, and many possible forms were proposed in the case of a bivariate Gamma distribution (see, e.g., Chapter 8 in [89] for a review). Here, we use the bivariate Gamma distribution derived by Moran using a copula [90]:

$$f(\mathbf{p}) = \frac{1}{\sqrt{1-\rho^2}} \exp \left\{ -\frac{1}{2(1-\rho^2)} [(\rho \tilde{p}_1)^2 - 2\rho \tilde{p}_1 \tilde{p}_2 + (\rho \tilde{p}_2)^2] \right\} f_{\mathcal{G}}(p_1; (\underline{p}_1, \delta_1)) f_{\mathcal{G}}(p_2; (\underline{p}_2, \delta_2)), \quad (4.29)$$

where $\rho \in (-1, 1)$ is the (Pearson) correlation coefficient between $P_1(\mathbf{x})$ and $P_2(\mathbf{x})$ (\mathbf{x} being fixed), and

$$\tilde{p}_i = \Phi^{-1}(F_{\mathcal{G}}(p_i; (\underline{p}_i, \delta_i))) , \quad i \in \{1, 2\} , \quad (4.30)$$

where Φ^{-1} is the inverse of the univariate Gaussian distribution function and $F_{\mathcal{G}}(\cdot; (\underline{p}_i, \delta_i))$ is the univariate Gamma distribution function with mean \underline{p}_i and coefficient of variation δ_i (which is associated with $f_{\mathcal{G}}(\cdot; (\underline{p}_i, \delta_i))$), and that the extreme cases $\rho = \pm 1$ are also well defined; see [90]. Notice that the vector of hyperparameters then reads as $\mathbf{w} = (\underline{p}_1, \delta_1, \underline{p}_2, \delta_2, \rho)$. It follows that

$$P_1(\mathbf{x}) = F_{\mathcal{G}}^{-1}(\Phi(\Upsilon_1(\mathbf{x})); (\underline{p}_1, \delta_1)) \quad (4.31)$$

and

$$P_2(\mathbf{x}) = F_{\mathcal{G}}^{-1}(\Phi(\Upsilon_2(\mathbf{x})); (\underline{p}_2, \delta_2)) \quad (4.32)$$

for any \mathbf{x} fixed in Ω , where $\Upsilon(\mathbf{x}) = (\Upsilon_1(\mathbf{x}), \Upsilon_2(\mathbf{x}))$ is a centered Gaussian random

variable with covariance matrix [90]:

$$[C_{\Upsilon}] = \begin{bmatrix} 1 & \rho \\ \rho & 1 \end{bmatrix}. \quad (4.33)$$

Upon using the Cholesky factorization $[C_{\Upsilon}] = [L_{\Upsilon}]^T [L_{\Upsilon}]$, it can be deduced that $\{\mathbf{P}(\mathbf{x}), \mathbf{x} \in \Omega\}$ can be defined through

$$P_1(\mathbf{x}) = F_{\mathcal{G}}^{-1}(\Phi(\Xi_1(\mathbf{x})); (\underline{p}_1, \delta_1)), \quad \forall \mathbf{x} \in \Omega, \quad (4.34)$$

and

$$P_2(\mathbf{x}) = F_{\mathcal{G}}^{-1}(\Phi(\rho \Xi_1(\mathbf{x}) + \sqrt{1 - \rho^2} \Xi_2(\mathbf{x})); (\underline{p}_2, \delta_2)), \quad \forall \mathbf{x} \in \Omega, \quad (4.35)$$

where $\{\Xi(\mathbf{x}) = (\Xi_1(\mathbf{x}), \Xi_2(\mathbf{x})), \mathbf{x} \in \mathbb{R}^n\}$ is a centered Gaussian random field with statistically independent, centered Gaussian components such that $\Upsilon(\mathbf{x}) = [L_{\Upsilon}]^T \Xi(\mathbf{x})$, $\forall \mathbf{x} \in \Omega$. Equations (4.34) and (4.35) define the nonlinear mapping \mathcal{T} introduced in Equation (4.25) such that $\mathbf{P}(\mathbf{x}) = \mathcal{T}(\Xi(\mathbf{x}))$, for all $\mathbf{x} \in \Omega$ (note that the spatial dependence of the transformation was dropped given the retained modeling assumptions). This relation can equivalently be stated as $\mathbf{P}(\mathbf{x}) = \mathcal{T}^*(\Upsilon(\mathbf{x}))$, with obvious notation. The Gaussian random fields are defined in the next section.

Construction of the Underlying Gaussian Models

In accordance with the periodic assumption retained in the mechanical modeling framework, it is assumed that each random field $\{\Xi_i(\mathbf{x}), \mathbf{x} \in \mathbb{R}^n\}$, $i \in \{1, 2\}$, satisfies the invariance property $\Xi_i(\mathbf{x}) = \Xi_i(\mathbf{x} + p\mathbf{x}')$ for all $\mathbf{x} \in \Omega$ and $\mathbf{x}' \in \mathbb{Z}^n$ P -almost surely, where it is assumed (without loss of generality) that $\Omega = ([0, p])^n$. Consequently, the centered random field $\{\Xi(\mathbf{x}), \mathbf{x} \in \mathbb{R}^n\}$ is uniquely defined by its restriction to Ω . Assuming the stationary of this restriction in Ω , the underlying Gaussian field is defined through the matrix-valued covariance function

$\boldsymbol{\tau} \mapsto [R_{\Xi}(\boldsymbol{\tau})] = \mathbb{E}\{\Xi(\mathbf{x} + \boldsymbol{\tau}) \otimes \Xi(\mathbf{x})\}$ such that

$$[R_{\Xi}(\boldsymbol{\tau})] = \begin{bmatrix} R_1(\boldsymbol{\tau}) & 0 \\ 0 & R_2(\boldsymbol{\tau}) \end{bmatrix}, \quad \forall \boldsymbol{\tau} \in ([0, p])^n, \quad (4.36)$$

where R_1 and R_2 are the p -periodic covariance functions defining (the restrictions of) $\{\Xi_1(\mathbf{x}), \mathbf{x} \in \mathbb{R}^n\}$ and $\{\Xi_2(\mathbf{x}), \mathbf{x} \in \mathbb{R}^n\}$ (to Ω), respectively. For the sake of illustration, we assume similar covariance functions for the two Gaussian components, setting $R_1 = R_2 = R$, and we consider the case of a separable covariance function in \mathbb{R}^2 :

$$R(\boldsymbol{\tau}) = R_1(\tau_1) \times R_2(\tau_2). \quad (4.37)$$

We further assume that R_1 and R_2 only differ in the choice of hyperparameters, so that the above equation can be written, using an abuse of notation, as

$$R(\boldsymbol{\tau}) = R(\tau_1; L_1) \times R(\tau_2; L_2), \quad (4.38)$$

where $L_1 > 0$ and $L_2 > 0$ are model parameters controlling the correlation ranges of the fields along the directions defined by the canonical basis in \mathbb{R}^2 . The univariate covariance function R is assumed to take the generic form

$$R_\phi(\tau; L) = \exp(-c\phi(\tau; L)), \quad \forall \tau \in [0, p], \quad (4.39)$$

where c is a positive constant (that depends on both ϕ and L) to be defined and ϕ is a p -periodic function taken as

$$\phi(\tau; L) = \frac{|\sin(\pi\tau/p)|}{L} \quad (\text{Periodic Exponential, PE}), \quad (4.40)$$

or

$$\phi(\tau; L) = \frac{\sin^2(\pi\tau/p)}{L^2} \quad (\text{Periodic Squared-Exponential, PSE}). \quad (4.41)$$

The subscript in the notation R_ϕ underlines the choice of a particular periodic function. The two functions defined by (4.40) and (4.41) are specifically chosen so as to investigate the impact of sample path regularity on fracture simulation outcomes. In particular, and while both functions yield random fields of fracture properties that are mean-square continuous, the periodic squared-exponential covariance function obtained by combining (4.39) and (4.41) leads to mean-square differentiable fields which exhibit “smooth” realizations. On the contrary, the periodic exponential function defined by considering (4.40) yields random fields that are not mean-square differentiable and thus have much rougher realizations.

In order to ensure meaningful comparison between the covariance models, the normalization constants are determined such that the spatial correlation length along the direction of one main direction is equal to L , that is:

$$\int_0^{p/2} |R_\phi(\tau; L)| d\tau = L . \quad (4.42)$$

For later use, we introduce the normalized correlation length $L^* = L/p$. For the squared exponential model, the constant c_{PSE} is hence required to satisfy the non-linear equation

$$\frac{1}{2} p \exp\left(-\frac{c_{\text{PSE}}}{2L^2}\right) I_0\left(\frac{c_{\text{PSE}}}{2L^2}\right) = L , \quad (4.43)$$

where I_0 is the 0th order modified Bessel’s function, whereas the constant c_{PE} associated with the exponential covariance kernel must satisfy

$$\frac{1}{2} p \left[I_0\left(\frac{c_{\text{PE}}}{L}\right) - S_0\left(\frac{c_{\text{PE}}}{L}\right) \right] = L , \quad (4.44)$$

where S_0 is the 0th order modified Struve’s function. In this work, these equations are solved numerically using a Newton-Raphson solver.

It should be noticed that the covariance function $\boldsymbol{\tau} \mapsto [\mathbf{R}_{\mathbf{T}}(\boldsymbol{\tau})]$ defining the restriction of the Gaussian random field $\{\mathbf{T}(\mathbf{x}), \mathbf{x} \in \mathbb{R}^n\}$ to Ω is given by

$$[\mathbf{R}_{\mathbf{T}}(\boldsymbol{\tau})] = \begin{bmatrix} \mathbf{R}_1(\boldsymbol{\tau}) & \rho \mathbf{R}_1(\boldsymbol{\tau}) \\ \rho \mathbf{R}_1(\boldsymbol{\tau}) & \rho^2 \mathbf{R}_1(\boldsymbol{\tau}) + (1 - \rho^2) \mathbf{R}_2(\boldsymbol{\tau}) \end{bmatrix}, \quad \forall \boldsymbol{\tau} \in ([0, p])^n, \quad (4.45)$$

which shows the role played by the parameter ρ on the covariance function of $\{P_2(\mathbf{x}), \mathbf{x} \in \Omega\}$ (after the action of \mathcal{T}^*).

Fundamental Properties of the Random Field of Fracture Properties

Based on the construction proposed in Sections ?? and ??, the non-Gaussian random field $\{\mathbf{P}(\mathbf{x}), \mathbf{x} \in \Omega\}$ modeling the fracture properties satisfies the following properties:

1. $P_i(\mathbf{x}) > 0$ for all $\mathbf{x} \in \Omega$ and $i \in \{1, 2\}$, almost surely.
2. $\{\mathbf{P}(\mathbf{x}), \mathbf{x} \in \Omega\}$ is of second order, $\mathbb{E}\{|0\mathbf{P}(\mathbf{x})|0^2\} < +\infty \quad \forall \mathbf{x} \in \Omega$.
3. The field satisfies $\mathbf{P}((0, x_2)) = \mathbf{P}((p, x_2))$ and $\mathbf{P}((x_1, 0)) = \mathbf{P}((x_1, p))$, almost surely.
4. The mean function $\mathbf{x} \mapsto \underline{\mathbf{p}}(\mathbf{x}) = \mathbb{E}\{\mathbf{P}(\mathbf{x})\}$ is given by $\underline{\mathbf{p}}(\mathbf{x}) = \underline{\mathbf{p}} = (\underline{p}_1, \underline{p}_2)$ for all $\mathbf{x} \in \Omega$.
5. The covariance matrix at any location $\mathbf{x} \in \Omega$ reads as

$$\mathbb{E}\{(\mathbf{P}(\mathbf{x}) - \underline{\mathbf{p}}) \otimes (\mathbf{P}(\mathbf{x}) - \underline{\mathbf{p}})\} = \begin{bmatrix} \underline{p}_1^2 \delta_1^2 & \underline{p}_1 \underline{p}_2 \delta_1 \delta_2 \rho \\ \underline{p}_1 \underline{p}_2 \delta_1 \delta_2 \rho & \underline{p}_2^2 \delta_2^2 \end{bmatrix}. \quad (4.46)$$

It can also be deduced that the random field $\{\mathbf{P}(\mathbf{x}), \mathbf{x} \in \Omega\}$ is mean-square continuous for the PE and PSE correlation functions introduced in Section ???. Finally, the field is mean-square differentiable for the PSE covariance function.

Recall that in the properties above, \underline{p}_1 and \underline{p}_2 correspond to the desired mean values for the fracture toughness \mathcal{G}_c and energy threshold ψ_c , and δ_1 and δ_2 are the coefficients of variation that control the statistical dispersions of these parameters. The parameter ρ measures the level of correlation between the fracture properties.

Stochastic Simulation Aspects

Simulating realizations of the random field of fracture properties requires (i) drawing realizations of the underlying Gaussian random fields defined in ??, and (ii) evaluating the nonlinear transformations defined by (4.34) and (4.35). Routines to compute the latter mappings are readily available in many scientific computing environments. Regarding the generation of the Gaussian fields, we presently resort to truncated Karhunen-Loëve expansions. Each (mean-square continuous) random field $\{\Xi_i(\mathbf{x}), \mathbf{x} \in \mathbb{R}^n\}$, $i \in \{1, 2\}$, is thus expanded as

$$\Xi_i(\mathbf{x}) = \sum_{k=1}^{q_i} \sqrt{\lambda_k} \eta_k \varphi_k(\mathbf{x}) , \quad (4.47)$$

where $\{\eta_k\}_{k \geq 1}$ is a set of independent normalized Gaussian random variables, and $\{\lambda_k\}_{k \geq 1}$ and $\{\varphi_k\}_{k \geq 1}$ are the nonnegative eigenvalues (ordered as a nonincreasing sequence) and the associated orthonormal eigenfunctions of the covariance function that satisfy the following integral equation (which is a Fredholm integral equation of the second kind):

$$\int_{\Omega} R(\mathbf{x}, \mathbf{x}') \varphi_k(\mathbf{x}') d\mathbf{X}' = \lambda_k \varphi_k(\mathbf{x}) , \quad \forall \mathbf{x} \in \Omega , \quad (4.48)$$

where R is the covariance kernel introduced in Section ?? (note the abuse of notation, with $\boldsymbol{\tau} = \mathbf{x} - \mathbf{x}'$). For arbitrary covariance functions, this integral equation can be solved by using a standard Galerkin formulation [91, 92]: given a finite set of basis

functions $\{\phi_j\}_{j=1}^{N_{\text{node}}} \subset L_2(\Omega)$, each eigenfunction is approximated as

$$\varphi_k(\boldsymbol{x}) \approx \sum_{j=1}^{N_{\text{node}}} \alpha_j^{(k)} \phi_j(\boldsymbol{x}) . \quad (4.49)$$

Substituting this approximation in the integral equation and enforcing the residual to be orthogonal to $\text{span}(\{\phi_j\}_{j=1}^{N_{\text{node}}})$, we obtain

$$\sum_{j=1}^{N_{\text{node}}} \alpha_j^{(k)} \int_{\Omega} \int_{\Omega} R(\boldsymbol{x}, \boldsymbol{x}') \phi_j(\boldsymbol{x}') \phi_{\ell}(\boldsymbol{x}) d\boldsymbol{X}' d\boldsymbol{X} = \sum_{j=1}^{N_{\text{node}}} \alpha_j^{(k)} \int_{\Omega} \lambda_j \phi_j(\boldsymbol{x}) \phi_{\ell}(\boldsymbol{x}) d\boldsymbol{X} . \quad (4.50)$$

Considering the above equation for all eigenfunctions leads to the generalized eigenvalue problem $[K][A] = [\Lambda][M][A]$, where $[A]_{j\ell} = \alpha_j^{(\ell)}$, $[\Lambda]_{j\ell} = \lambda_j \delta_{j\ell}$ (with $\delta_{j\ell}$ the Kronecker delta), and $[K]$ and $[M]$ are the matrices with entries

$$[K]_{j\ell} = \int_{\Omega} \int_{\Omega} R(\boldsymbol{x}, \boldsymbol{x}') \phi_j(\boldsymbol{x}') \phi_{\ell}(\boldsymbol{x}) d\boldsymbol{X}' d\boldsymbol{X} , \quad [M]_{j\ell} = \int_{\Omega} \phi_j(\boldsymbol{x}) \phi_{\ell}(\boldsymbol{x}) d\boldsymbol{X} . \quad (4.51)$$

For each Gaussian field $\{\Xi_i(\boldsymbol{x}), \boldsymbol{x} \in \mathbb{R}^n\}$, the truncation order $q_i \leq N_{\text{node}}$ can be determined by analyzing the convergence of the error function

$$\varepsilon_{\text{KL}}(q) = 1 - \left(\sum_{k=1}^q \lambda_k \sqrt{\sum_{k=1}^{N_{\text{node}}} \lambda_k} \right) , \quad (4.52)$$

and by selecting q_i such that $\varepsilon_{\text{KL}}(q_i) \leq \varepsilon_0$ for some given tolerance $0 < \varepsilon_0 \ll 1$.

4.3 Verification

4.3.1 Mode I: Edge-Notched Unilateral Tension Test

Consider a $1 \text{ mm} \times 1 \text{ mm}$ plate with a pre-existing crack on the left side, loaded in uniaxial tension, as shown in Figure 4.1a. We assume the plate to be composed of an

isotropic material with Young's modulus $E = 2.1 \times 10^5$ MPa, Poisson's ratio $\nu = 0.3$, fracture toughness $\mathcal{G}_c = 2.7$ mJ mm $^{-2}$, and critical strength $\sigma_c = 2.5 \times 10^3$ MPa. The plate is fixed along the bottom, and the top surface is displaced in the vertical direction. Roller supports are also assumed to be in place, such that the horizontal displacement vanishes along the top surface. The plate is assumed to be sufficiently thick such that plane strain conditions hold.

The domain is meshed with linear triangular elements. The maximum/minimum element characteristic lengths are 0.05 mm and 0.005 mm, respectively, corresponding to a mesh with 7845 elements. The crack surface density is approximated with a regularization length $l = 0.015$ mm, such that the half phase-field bandwidth is resolved by approximately 6 elements.

We examine two representations of the pre-existing crack. First, we use a “geometric notch” to represent the crack as shown in Figures 4.1b and 4.2a. In this case, the traction-free boundary condition on the notch surfaces is satisfied in a weak sense. The resulting damage fields as a function of boundary displacement are shown in Figures 4.2b to 4.2d. Only the damage fields obtained using the spectral decomposition are shown in the Figures. Contours of the damage field obtained using the contact split with a threshold were found to be indistinguishable.

Secondly, we use an initial damage field $d(t = 0) = d_0$ to represent the initial crack, where d_0 is given by:

$$d_0(\mathbf{x}) = \begin{cases} \left(1 - \frac{\tau(\mathbf{x})}{2l}\right)^2, & \tau(\mathbf{x}) \leq 2l \\ 0, & \tau(\mathbf{x}) > 2l \end{cases} \quad (4.53)$$

$$\text{with} \quad (4.54)$$

$$\tau(\mathbf{x}) = \begin{cases} |\mathbf{x} \cdot \mathbf{e}_2|, & \mathbf{x} \cdot \mathbf{e}_1 \leq 0, \\ \|\mathbf{x}\|, & \mathbf{x} \cdot \mathbf{e}_1 > 0, \end{cases} \quad (4.55)$$

with an origin for the coordinate system at the center of the plate. The initial damage

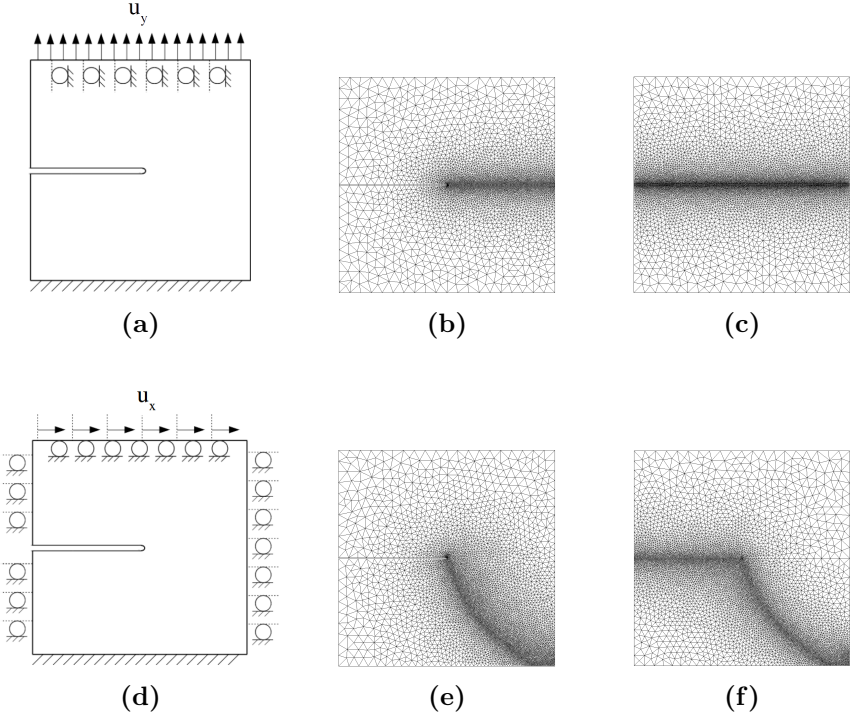


FIGURE 4.1. Boundary conditions of the plate with a pre-existing crack for (a) a mode I tension test and (d) a mode II shear test. Finite element meshes for the mode I calculations (b - c) and for the mode II calculations (e - f). For (b, e) the meshes have the initial crack geometry “meshed-in” while (c, f) have local refinement around the initial damage field. All meshes are pre-refined along the predicted crack-path with a characteristic element size of 0.005 mm.

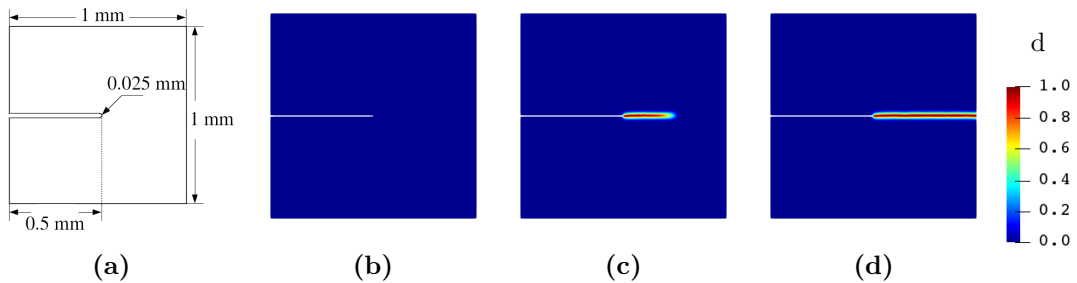


FIGURE 4.2. Edge-notched specimen loaded in tension with initial crack represented by a geometric notch with a rounded corner. (a) Dimensions of the notched plate. Damage d at (b) $u_y = 0$ mm, (c) $u_y = 0.0048$ mm, (d) $u_y = 0.006$ mm.

field is resolved using the locally refined mesh of linear triangular elements shown in Figure 4.1c. The resulting initial damage field is shown in Figure 4.3b. Once again,

the contour plots of the damage field obtained using a spectral decomposition and the contact split were found to be indistinguishable.

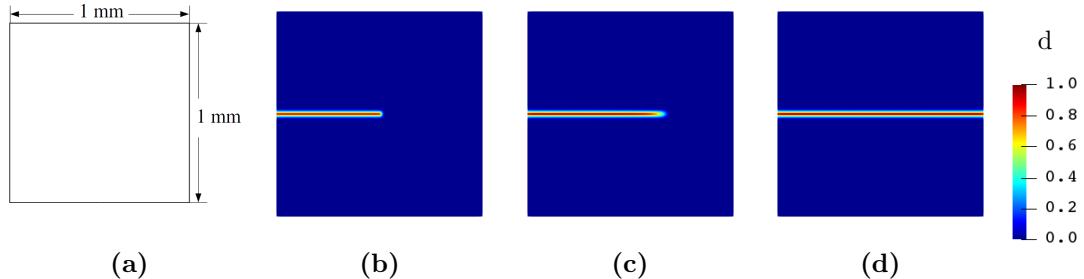


FIGURE 4.3. Edge-notched specimen loaded in tension with initial crack represented by a damage field. (a) Dimensions of the intact plate. The Damage d at (b) $u_y = 0 \text{ mm}$ (c) $u_y = 0.0048 \text{ mm}$ (d) $u_y = 0.006 \text{ mm}$.

Plots of the vertical component of the reaction force at the top boundary of the plate versus the prescribed y -displacement are shown in Figure 4.4, for both representations of the initial crack and split strategies. The reaction force is nondimensionalized with respect to the critical strength and the plate thickness, i.e. $f_y^* = f_y / (\sigma_c t)$, and the displacement is nondimensionalized by $u_y^* = u_y / a$, where a is the side length of the square plate. As expected, the contact split does not affect the material response in the uniaxial loading case (Figure 4.4a), and the results appear to be relatively insensitive to the choice of threshold for switching between the spectral split and the contact split (Figure 4.4b).

4.3.2 Mode II: Edge-Notched Shear Test

The effect of the proposed energy split becomes readily apparent when the loading case is dominated by in-plane or out-of-plane shear. Let us consider the same edge-notched thick plate as in the last section, but subjected to a different loading. A schematic of the boundary conditions for this case and the corresponding meshes are shown in Figures 4.1d to 4.1f.

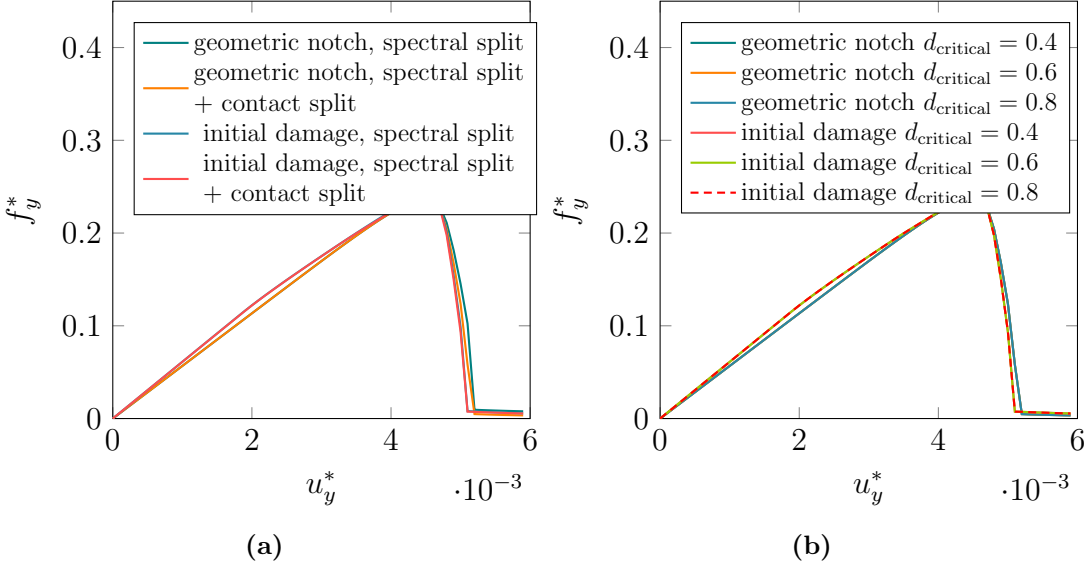


FIGURE 4.4. Mode I force–displacement curves obtained using (a) the spectral decomposition with two representations of the pre-existing crack (b) a spectral decomposition in conjunction with the contact split with different critical damage threshold on two representations of the pre-existing crack.

Once again, the effect of the contact split is examined by comparing the results using two different representations of the initial crack, as shown in Figure 4.5 and Figure 4.6a. Simulations that rely solely on the spectral decomposition result in dramatically different crack paths (Figures 4.5c, 4.5d, 4.5g and 4.5h) and force-displacement responses (Figure 4.6a). We note that after the initial decay following a horizontal displacement of $u_x = 1.0 \times 10^{-2}$ mm, the force for the geometric notch with the spectral decomposition begins to rise. Even though the damage field completely separates the plate into two sections, the force continues to increase. This is because the spectral decomposition does not prevent all traction from being transmitted across a fully damaged surface.

In contrast, when the traction-free condition is enforced using the contact split, the crack paths (Figures 4.5c, 4.5d, 4.5k and 4.5l) as well as the force-displacement curves (Figure 4.6b) are similar for both representations of the pre-existing crack. Notably in this case, the force at the boundary decays completely to zero as the plate

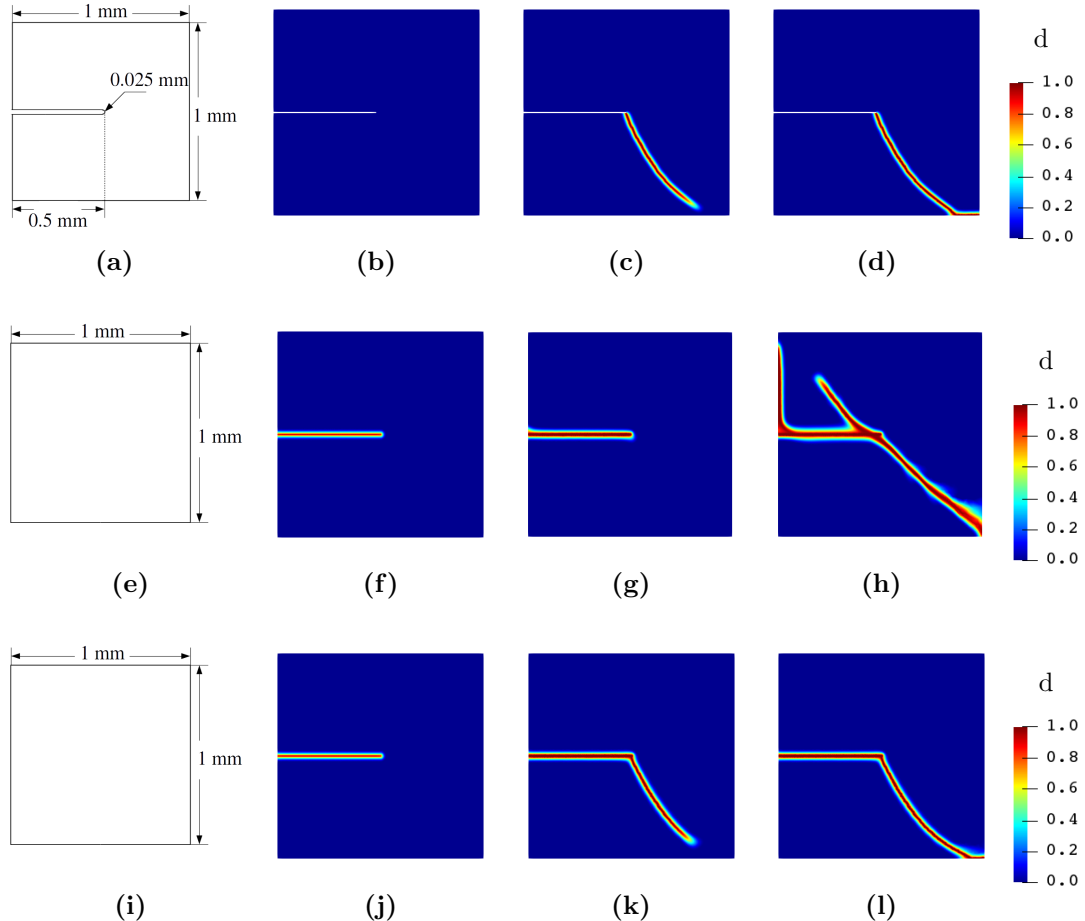


FIGURE 4.5. The crack paths obtained using (a-d) the spectral decomposition on a geometrically notched plate, (e-h) the spectral decomposition with an initial damage field d_0 (4.53) representing the initial crack, and (i-l) the contact split with an initial damage field. Snapshots of crack paths are shown at (b,f,j) $u_x = 0$ mm, (c,g,k) $u_x = 0.0109$ mm, and (d,h,l) $u_x = 0.02$ mm.

is separated in two by the damage field. As shown in Figure 4.6b, the results are also relatively insensitive to the particular choice of threshold for the contact split.

We note that if the threshold is selected to be too high (e.g. $d_{\text{critical}} \geq 0.8$) a small upward perturbation in the force-displacement curve can be observed, shortly after a horizontal displacement of $u_x = 1.0 \times 10^{-2}$ mm. The brief increase is due to the fact that the band of damage wherein the contact split is applied is too small, and some traction can still be transmitted across the fully damaged band. Essentially, there are

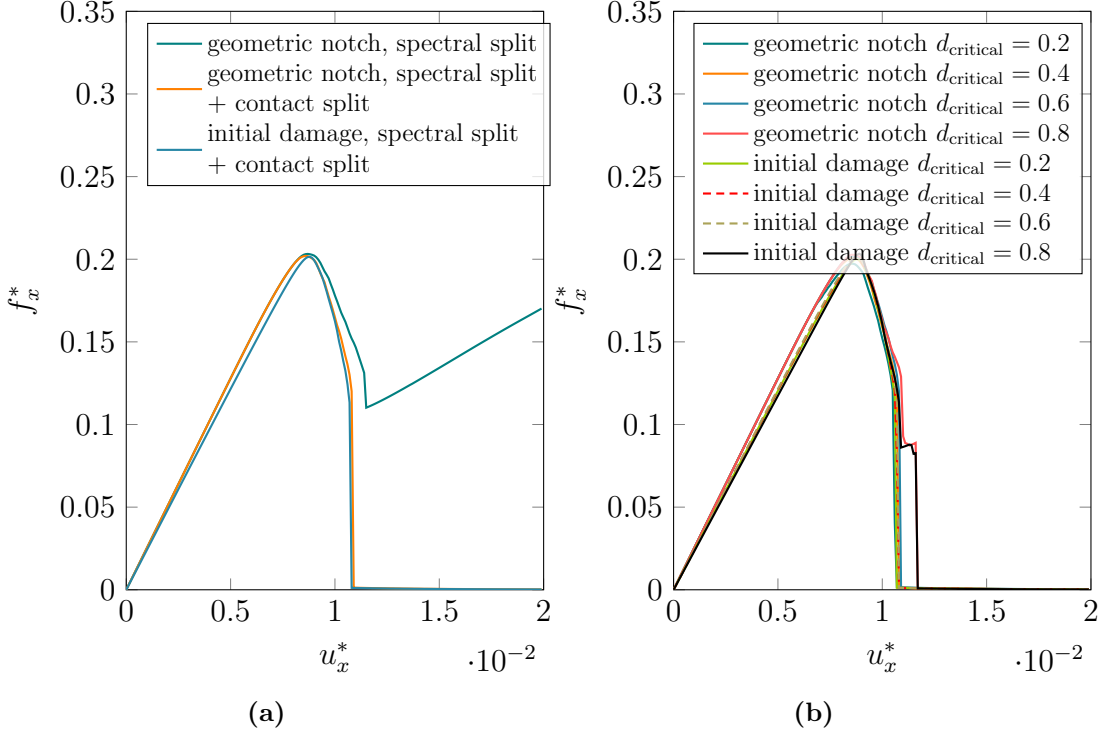


FIGURE 4.6. Mode II force–displacement curves obtained using (a) spectral decomposition with two representations of the initial crack (b) spectral decomposition in conjunction with the contact split with different critical damage threshold on two representations of the initial crack.

elements capturing the peak damage field wherein some quadrature points are below the threshold while others are above it. While further mesh refinement can remove this artifact, in practice we employ meshes that sufficiently capture the phase-field regularization, wherein $2l/h^e = 5$. Given this level of mesh refinement and typical damage profiles, we anticipate that a threshold of $d_{\text{critical}} = 0.6$ is sufficient to prevent any such artifacts. As such, we employ a threshold of $d_{\text{critical}} = 0.6$ for all subsequent problems.

4.3.3 Crack Propagation Under Biaxial Tension

We now examine a problem in which a thin plate with initial imperfections is subject to biaxial tension. Plane-stress conditions are assumed to hold. The plate geometry

and boundary conditions are summarized in Figure 4.7a, and the initial damage field representing two imperfections is shown in Figure 4.7b. Periodic boundary conditions are assumed on all sides.

Using property values that are representative of a typical clay specimen, the plate is assumed to be composed of a material with a Young's modulus E of 4 MPa, a Poisson's ratio ν of 0.2, a fracture toughness \mathcal{G}_c of 27 kJ m^{-2} , and a critical fracture energy ψ_c of 30 J m^{-2} .

The governing equation for the mechanical problem in this case is given by:

$$\nabla \cdot (\tilde{\boldsymbol{\sigma}} + \sigma_0 \mathbf{I}) = 0, \quad (4.56)$$

where σ_0 is a scalar-valued function that varies temporally and serves to model the drying process. The initial stress $\sigma_0 \mathbf{I}$ is equivalent to an inelastic eigen-strain, i.e. $\boldsymbol{\varepsilon}_0 = \mathbb{S} : (\sigma_0 \mathbf{I})$, where \mathbb{S} is the compliance tensor.

With a view towards nondimensionalization, as will be discussed in ??, the fracture driving force may be nondimensionalized as

$$\mathcal{D}^* = \sqrt{\frac{(1 - \nu^2)a}{E\mathcal{G}_c}} \sigma_0, \quad (4.57)$$

where a is a characteristic size for the domain. Here, we choose it to be the width of the plate.

We now compare simulation results obtained using three elastic energy split techniques: a no-split approach, the spectral split, and the contact split. The damage fields obtained using the three different split techniques are shown in Figure 4.8 at representative magnitudes of the dimensionless driving force.

The no-split approach treats the entire elastic energy as an active potential to be degraded, neglecting the tension-compression asymmetry. It is widely used in calculations of drying processes because the effective loading condition is assumed

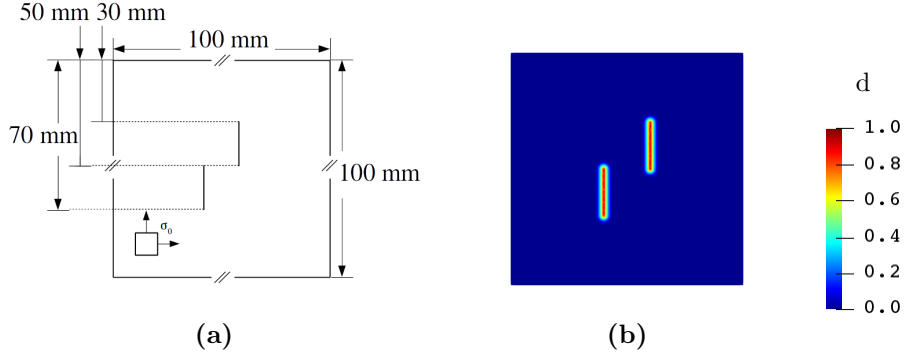


FIGURE 4.7. (a) Dimensions and boundary conditions of a thin plate with two parallel initial cracks. (b) The initial cracks are represented by an initial damage field.

to be tensile: biaxial tension in 2D and triaxial tension in 3D. However, we note that tensile loading conditions do not necessarily lead to a tensile local stress/strain state everywhere in the domain, hence it is possible to have crack propagation under compression, as can be observed in this example. We will return to this issue after examining the results obtained using a spectral decomposition and a spectral decomposition with the contact split.

The spectral decomposition prevents crack propagation under compression (Figure 4.8d), but without enforcing the traction-free condition on the crack surfaces represented by the damage field, which may affect secondary crack paths that emerge from existing crack surfaces (Figure 4.8e). Such artifacts can be removed by enforcing the traction-free condition on the regularized crack surfaces using the contact split (Figures 4.8g to 4.8i).

We now return to the issue of the possibility of crack growth under compression with a no-split approach. Comparing the damage profiles shown in Figures 4.8a, 4.8d and 4.8g one can observe that a damage bridge forms between the two vertical initial cracks only for the case of a no-split method. To explore this region more precisely, we consider the fields immediately before the bridge forms, and examine

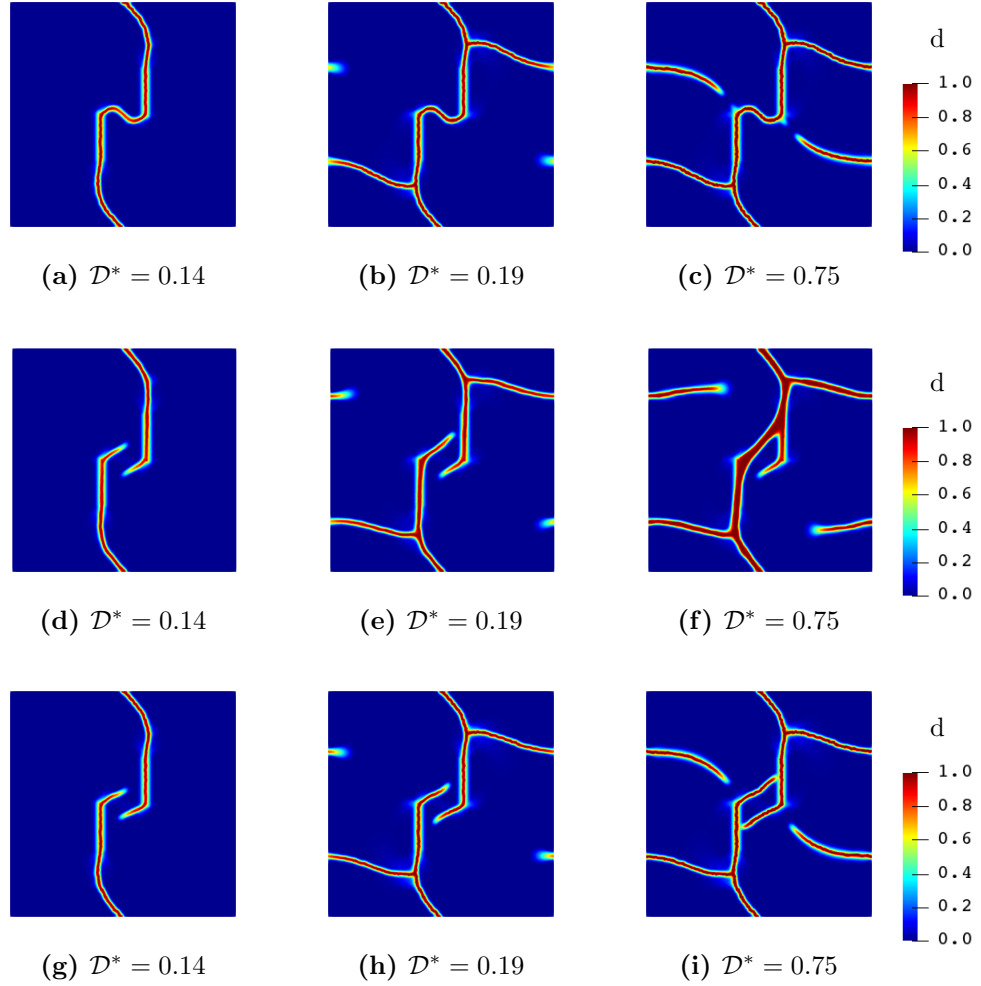


FIGURE 4.8. Crack paths obtained using (a-c) a no-split technique (d-f) the spectral decomposition (g-i) the contact split.

contour plots of the normal pressure for an orientation that is orthogonal to the bridge (Figure 4.9). The contour plots clearly indicate that the region is loaded in compression immediately before the bridge forms.

As a final observation in this section, we note that the crack-paths obtained using the spectral decomposition exhibit a broadening of the damage field at late stages of growth (Figure 4.8f). By contrast, the contact decomposition results in damage profiles that remain relatively thin compared to the specimen dimensions (Figure 4.8i).

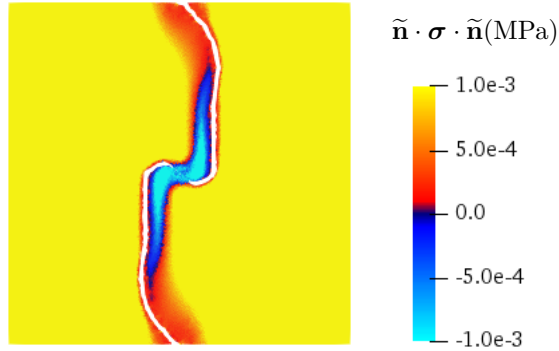


FIGURE 4.9. Contour plot of the normal pressure right before the bridge forms. The pressure is calculated for an orientation that is estimated to be orthogonal to the bridge. Elements within the contour of $d = 0.75$ are removed to indicate the current crack set.

4.3.4 Reconstruction of the marginal PDF

4.4 Numerical examples

In this section, we study in detail the formation of crack networks in thin films and soil dessication. We begin in Section ?? with a deterministic benchmark problem under quasi-one-dimensional conditions. The spacing between fractures is calculated as a function of the driving force with the cohesive fracture model and compared against a linear elasticity solution. Attention is then turned to an investigation of the stochastic aspects of fracture with a two-dimensional plane stress model in Section ??, wherein the fracture toughness and critical fracture energy are modeled as random fields. Finally, in Section ?? we present stochastic simulations of a soil dessication process in three dimensions.

4.4.1 One-Dimensional Simplification: Side View

We begin by deriving an analytical solution for the fracture of a thin film bonded to a thick substrate, as shown in Figure 4.10. Assuming that the planar dimensions of the film are much larger than its thickness, we first simplify the problem into a

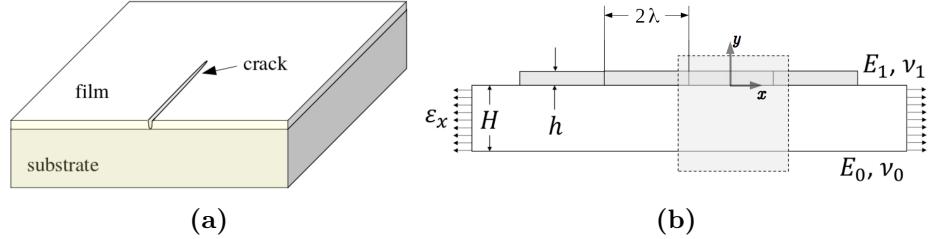


FIGURE 4.10. Description of a one-dimensional model for thin-film cracking. (a) Side view (highlighted in yellow) of the geometry (b) schematic representation of the side view. The elasticity solution is derived for the region highlighted with the shaded box, i.e. between the two discontinuities across the thin film. The coordinate system is centered at the middle of the bottom surface of the thin film.

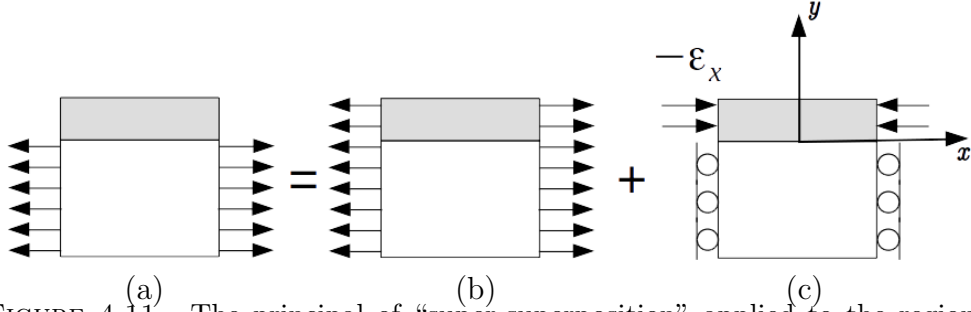


FIGURE 4.11. The principle of “super-superposition” applied to the region of interest marked in Figure 4.10b. The analytical solution is derived based on the boundary conditions shown in (c).

two-dimensional (or quasi 1D) plane-strain problem. The film is assumed to have Young's modulus E_1 , Poisson's ratio ν_1 , and thickness h . The substrate has Young's modulus E_0 , Poisson's ratio ν_0 , and thickness H . The fracture of the film is driven by the underlying substrate being stretched an amount ε_x . The problem with these simplifications and assumptions has been studied by many researchers, and analytical solutions from elasticity theory have been derived in several different ways. The derivation presented herein most closely follows that provided in Yin et al. [70].

With the increase of the tensile strain in the substrate, some uniformly distributed discontinuities with spacing 2λ form across the thickness of the film. We assume that no debonding occurs and that the vertical component of the displacement does not

vary in the horizontal direction, i.e.

$$u_y(x, y) = u_y(y). \quad (4.58)$$

The plane-strain equilibrium equation in the x-direction is written as

$$\frac{E_1}{1 - \nu_1^2} u_{x,xx} + \mu_1 u_{x,yy} = 0, \quad (4.59)$$

where μ_1 denotes the shear modulus of the film. This is supplemented by appropriate boundary conditions (Figure 4.11)

$$u_x(0, y) = 0, \quad (4.60)$$

$$u_{x,y}(x, h) = 0, \quad (4.61)$$

$$\frac{1}{h} \int_0^h \sigma_x(\lambda, y) dy = -\frac{E_1}{1 - \nu_1^2} \varepsilon_x. \quad (4.62)$$

We obtain the closed-form solution to the displacement field

$$u_x(x, y) = \varepsilon_x x - \frac{\sinh(cx/h)}{\cosh(c\lambda/h)} \frac{\cos(d(1 - y/h))}{\sin(d)} \sqrt{\frac{E_1}{\mu_1(1 - \nu_1^2)}} h \varepsilon_x, \quad (4.63)$$

where c and d are functions of Dundur's parameters α and β . Following [93, 69, 70], c and d can be computed as:

$$c = \frac{2}{\pi k(\alpha, \beta)}, \quad d = \sqrt{\frac{2}{1 - \nu_1}} c, \quad (4.64)$$

$$\alpha = \frac{\bar{E}_1 - \bar{E}_0}{\bar{E}_1 + \bar{E}_0}, \quad \beta = \frac{\mu_1(1 - 2\nu_0) - \mu_0(1 - 2\nu_1)}{2\mu_1(1 - \nu_0) + 2\mu_0(1 - \nu_1)}, \quad (4.65)$$

$$k(\alpha, \beta) \approx k(\alpha) = \frac{1.258 - 0.4\alpha - 0.26\alpha^3 - 0.3\alpha^4}{1 - \alpha}, \quad (4.66)$$

with $\bar{E}_0 = \frac{E_0}{(1 - \nu_0^2)}$, and $\bar{E}_1 = \frac{E_1}{(1 - \nu_1^2)}$. By replacing λ with $\lambda/2$, the crack opening

displacement can be written as

$$\delta(0, y) = 2 \tanh\left(\frac{c\lambda}{2h}\right) \frac{\cos(d(1 - y/h))}{\sin(d)} \sqrt{\frac{E_1}{\mu_1(1 - \nu_1^2)}} h \varepsilon_x. \quad (4.67)$$

Then the fracture toughness can be obtained as the work done to close the crack, i.e.

$$\mathcal{G}_c \cdot 2h = \int_0^h \sigma_x(0, y) \delta(0, y) \, dy, \quad (4.68)$$

$$\mathcal{G}_c = \frac{(1 - \nu_1^2)\sigma_x^2 h}{E_1 c} \left[2 \tanh\left(\frac{c\lambda}{2h}\right) - \tanh(c\lambda/h) \right]. \quad (4.69)$$

The amount of energy released by opening a transverse crack is governed by two dimensionless parameters:

$$\mathcal{D}^* = \sqrt{\frac{(1 - \nu_1^2)h}{E_1 \mathcal{G}_c}} \sigma_x, \quad l^* = \frac{\lambda}{h}. \quad (4.70)$$

It is then convenient to interpret the parameter \mathcal{D}^* as the dimensionless fracture driving energy and l^* as the dimensionless crack spacing. (4.69) can be rendered dimensionless following (4.70), and the relation between the dimensionless fracture driving energy and the dimensionless crack spacing can be written as

$$\mathcal{D}^* \mathcal{C}(l^*; c) = 1, \quad \mathcal{C}(l^*; c) = \frac{1}{c} \left[2 \tanh\left(\frac{1}{2} cl^*\right) - \tanh(cl^*) \right]. \quad (4.71)$$

In Figure 4.12a, we set the Poisson's ratio of both the film and the substrate to be $\nu_0 = \nu_1 = 0.2$, and plot the dimensionless fracture driving energy versus the dimensionless crack spacing for different combinations of the mismatch in the Young's modulus between the film and the substrate.

Next, we performed a series of numerical simulations using the phase-field for cohesive fracture model following the setup described in Figure 4.10b. Specifically,

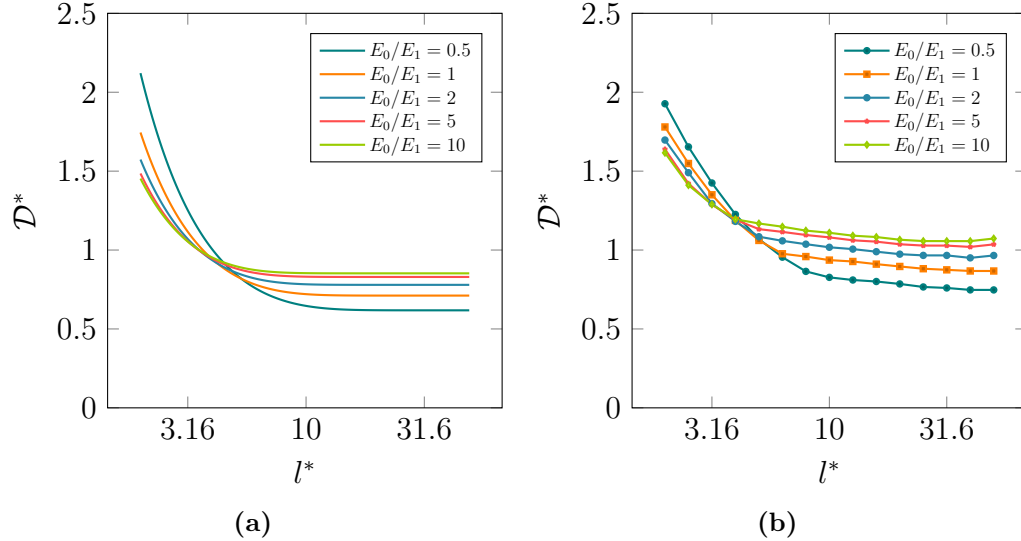


FIGURE 4.12. Relationship between the dimensionless fracture driving energy and the dimensionless crack spacing: (a) analytical solution using linear elasticity; and (b) numerically generated curves using the phase-field for cohesive model detailed in this work.

we examine the amount of driving energy required to propagate one transverse crack through the thickness of the film. The substrate and the film are represented by two rectangular domains $\Omega_0 = [-\lambda, \lambda] \times [-5 \text{ mm}, 0]$ and $\Omega_1 = [-\lambda, \lambda] \times [0, 1 \text{ mm}]$, respectively. The film-substrate system is the union of the two, i.e. $\Omega = \Omega_0 \cup \Omega_1$, and left-right periodicity is enforced. The substrate and the film are discretized with linear triangular elements with characteristic lengths of $h_0^e = \lambda/10$ and $h_1^e = \lambda/100$, respectively. The numerical results (Figure 4.12b) show a good agreement with the analytical solution.

4.4.2 Two-Dimensional Simplification: Stochastic Aspects of Fracture

We now consider a two-dimensional model of a thin film on a substrate wherein the geometry of the resulting fracture patterns is considerably more complex. For the bulk material properties, we adopt values that are representative of clay. The material properties and model parameters are summarized in Table 4.1.

We focus attention on the sensitivity of the resulting fracture patterns to stochastic spatial variations in the fracture properties. The random field of fracture properties $\{(\mathcal{G}_c(\mathbf{x}), \psi_c(\mathbf{x})), \mathbf{x} \in \Omega\}$ is defined and sampled following the model and procedures presented in ???. For all cases, the spatial correlation length L is larger than the regularization length l of the phase-field model. A tolerance of 1×10^{-3} is chosen for the truncation error in the Karhunen-Loëve expansion (4.52). The mean values of \mathcal{G}_c and ψ_c are chosen in accordance with reported values for clay as listed in Table 4.1. Coefficients of variation are chosen to be 0.03, leading to a variation of about $\pm 10\%$ around the mean value for the two random fracture parameters. All realizations shown in figures are normalized with respect to the corresponding stationary mean function, and the normalized quantities are denoted by \mathcal{G}_c^* and ψ_c^* .

Table 4.1. Summary of material properties and model parameters for all calculations in ??

Property/Parameter	Symbol	Value	Unit	Comment
Young's modulus	E	4	MPa	See [94, 1]
Poisson's ratio	ν	0.2	nondim.	See [94, 1]
Mean fracture toughness	$\underline{\mathcal{G}}_c$	27	kJ m^{-2}	See [95]
Mean critical fracture energy	$\underline{\psi}_c$	30	J m^{-2}	See [95]
Regularization length	l	0.5	mm	Such that $2l/h^e \approx 5$
Degradation shape parameter	p	1	nondim.	

A Plane-Stress Model

We now consider the problem of a thin film of thickness h that is bonded to an elastic underlayer of thickness H , as shown in Figure 4.13. The entire structure is assumed to be bonded to a rigid substrate. For this case, we employ the shear-lag model that is detailed in [66]. For the sake of clarity, the model is briefly described here.

We consider a square domain and assume the characteristic fragment sizes to be small compared to the overall specimen dimensions, and impose periodic boundary

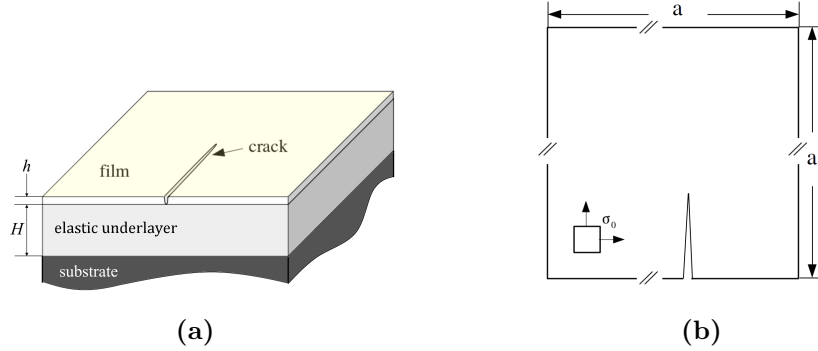


FIGURE 4.13. Description of a two-dimensional model for thin-film cracking. (a) Top view (highlighted in yellow) (b) schematic representation of the top view. A typical crack is shown to emphasize that fracture is only considered in the film.

conditions on all four boundaries. Assuming the underlying elastic layer is sufficiently thick and that the shear stress is uniform, equilibrium of a differential element of the film at the film-layer interface yields

$$\nabla \cdot \boldsymbol{\sigma} = \mu \frac{\mathbf{u}}{hH}, \quad (4.72)$$

where $\boldsymbol{\sigma} = \mathbb{C} : [\boldsymbol{\varepsilon} - \mathbb{S} : (\sigma_0 \mathbf{I})]$ is the stress, μ is the shear modulus of the elastic underlayer, and \mathbf{u} is the displacement. The corresponding potential energy representing the mismatch between the two sides of the film-layer interface can be written as

$$\psi_{\text{interface}} = \frac{1}{2} \frac{\mu}{hH} \|\mathbf{u}\|^2. \quad (4.73)$$

The underlying elastic layer is assumed to be much thicker than the film, i.e. $H = mh$, where $m \gg 1$. The interfacial energy can therefore be simplified as

$$\psi_{\text{interface}} = \frac{1}{2} \frac{\mu}{mh^2} \|\mathbf{u}\|^2. \quad (4.74)$$

The total energy of the simplified plane-stress model can then be written as

$$\begin{aligned} \Psi_{\text{total}} = & - \underbrace{\left(\int_{\partial\Omega} \boldsymbol{\tau} \cdot \mathbf{u} \, dA + \int_{\Omega} \mathbf{b} \cdot \mathbf{u} \, dV \right)}_{\text{external energy}} + \underbrace{\int_{\Omega} g(d) \psi_{\text{elastic}}^{(A)} \, dV + \int_{\Omega} \psi_{\text{elastic}}^{(I)} \, dV}_{\text{degraded elastic energy}} \\ & + \underbrace{\int_{\Omega} g(d) \frac{1}{2} \frac{\mu}{mh^2} \|\mathbf{u}\|^2 \, dV}_{\text{degraded interfacial energy}} + \underbrace{\int_{\Omega} \frac{3G_c}{8l} (d + l^2 \|\nabla d\|^2) \, dV}_{\text{approx. fracture energy}} \end{aligned} \quad (4.75)$$

For all calculations in ??, we assume $\frac{\mu}{mh^2} = 0.1$.

The square domain is discretized using linear triangular elements with a characteristic length of $h^e = a/500$. This mesh is used for the displacement subproblem for linear elasticity, the phase-field subproblem for fracture, and the generalized eigenvalue problem for the random fields. The displacement field and the damage field are constrained to be a -periodic, and the random fields are constructed to be a -periodic as well.

Effect of Correlation Length and Smoothness

To study the effect of the correlation length, crack patterns for four different values of L are compared. Ten calculations, corresponding to ten samples of the stochastic fields, are carried out for each value of L . Representative random fields and their corresponding damage fields are shown in Figure 4.14. A Flooding algorithm (described in ??) is used to group elements into clusters in a volume-preserving way, to facilitate the counting of distinct fragments. Following the one-dimensional derivation (??), two dimensionless parameters are extracted as

$$\mathcal{D}^* = \sqrt{\frac{(1 - \nu_1^2)h}{E_1 G_c}} \sigma_0, \quad l^* = \frac{\lambda}{h}, \quad \lambda \approx \sqrt{A}, \quad (4.76)$$

where the crack spacing λ is estimated from the fragment area A . Dimensionless curves are plotted in Figure 4.16.

As expected, it is seen that the PSE covariance model generates smoother realizations. As the normalized correlation length $L^* = L/p$ becomes larger, i.e. Figures 4.14c, 4.14i and 4.14o, a substantial amount of damage accumulates before localization occurs to form a “crack”. When the sample exhibits less spatial fluctuations, a non-negligible portion of the energy is dissipated into the matrix in the form of diffuse damage, resulting in fewer cracks and larger fragment sizes. As the normalized correlation gets even larger, i.e. Figures 4.14m to 4.14o, morphologically different crack networks are obtained.

On the other hand, the rougher samples generated using the PE covariance function, i.e. Figures 4.14d to 4.14f, 4.14j to 4.14l and 4.14p to 4.14r, have sufficient variations that serve as effective imperfections for damage localization. In terms of the mean size of fragments that form, the corresponding damage fields are seen to be far less sensitive to the spatial correlation length. However, as the correlation length increases, the orientation of the damage fields begins to acquire a structure that aligns with the axes of the domain. This observation is in accordance with the tensor-product structure of the covariance model, and with the fact that larger correlation lengths allow more pronounced spatial structures to develop (sample-wise) for PE functions.

Samples obtained with the two covariance models (parameterized by the same correlation lengths), considering the same realization for the underlying Gaussian field (from one covariance model to another), are compared in Figure 4.15 to study the effect of smoothness. It is seen that rougher material properties provide more candidate locations for damage localization, hence resulting in more fragments per unit volume of the domain (in a statistical sense). More precisely, the probability density functions (PDFs) corresponding to the dimensionless crack spacing (Figure 4.17),

estimated using approximately 2000 fragments and 10 independent realizations of the fields, show a substantial difference: the mean fragment size obtained with rough material properties (here, with the PE model) turns out to be much smaller than the mean fragment size generated by smoother samples of fracture properties (associated with the PSE model).

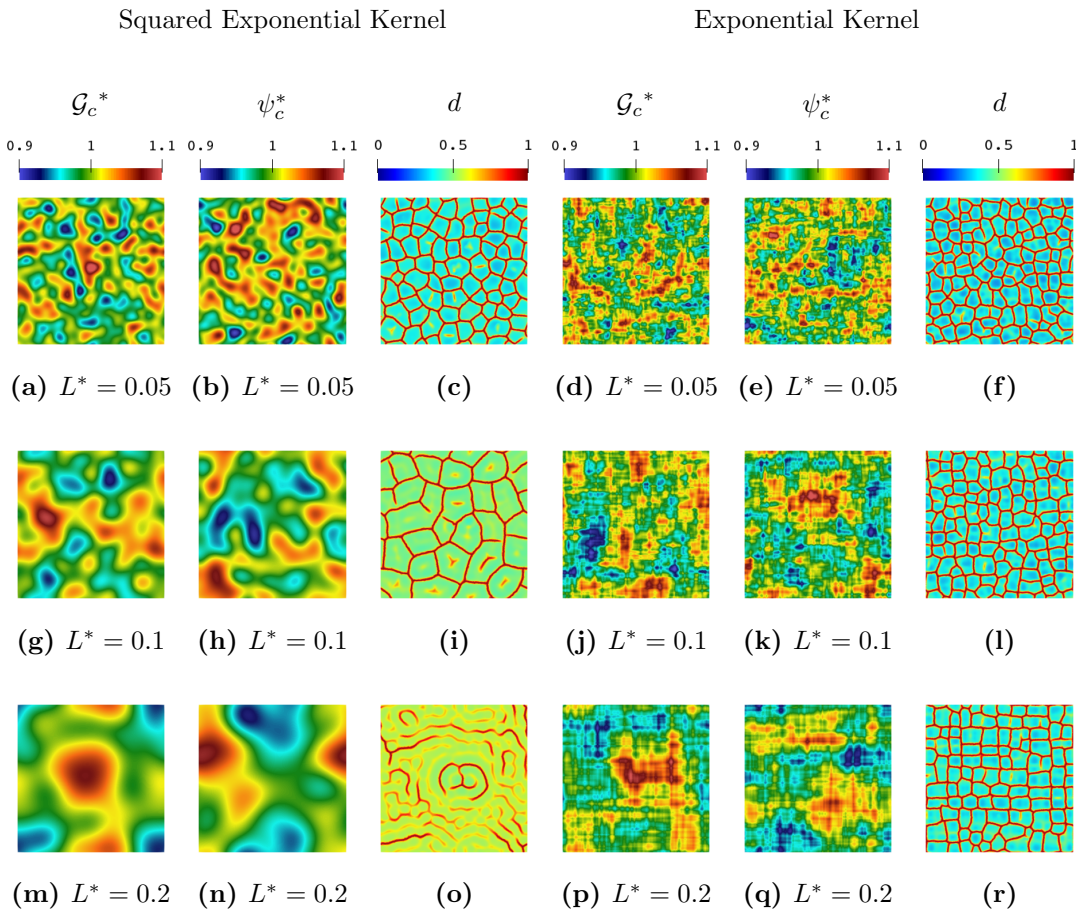


FIGURE 4.14. Damage fields resulting from six pairs of realizations with different correlation models and normalized correlation lengths. The left three pairs (a-b, g-h, m-n) are realizations obtained with a PSE covariance function, while the right three pairs (d-e, j-k, p-q) are samples generated with a PE covariance function. Energy release rate \mathcal{G}_c and the critical fracture energy ψ_c have a coefficient of variation of 0.03, and normalized spatial correlation length L^* of (a-b, d-e) 0.05 (g-h, j-k) 0.1 (m-n, p-q) 0.2. The corresponding damage fields are shown in (c, f, i, l, o, r), respectively. In these results, independent realizations of the underlying Gaussian fields are used.

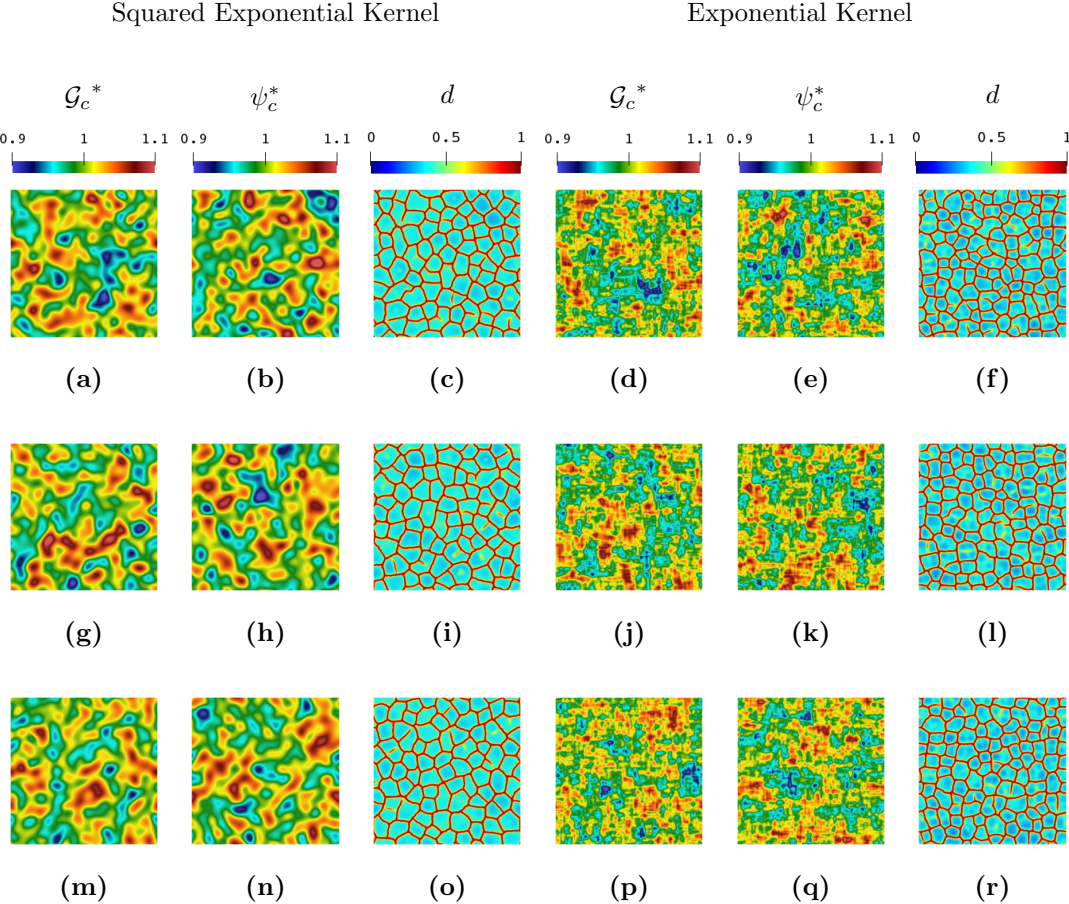


FIGURE 4.15. Three pairs of qualitative comparison of smoothness of the kernel function with the same normalized correlation length $L^* = 0.05$. (a-f) pair 1 (g-l) pair 2 (m-r) pair 3. Each row compares two kernel functions transformed from the same samples of the underlying Gaussian fields.

Parametric Analysis

The stochastic model constructed in this paper enables the introduction of point-wise correlation (that is, in the first-order marginal probability distribution) between the two fracture properties. With regard to fracture mechanics, one might wonder, for example, whether or not the fracture toughness \mathcal{G}_c and the critical fracture energy ψ_c are correlated (at a given location), and if so, to what extent. In this section, we perform a parametric analysis for different values of the correlation coefficient ρ ,

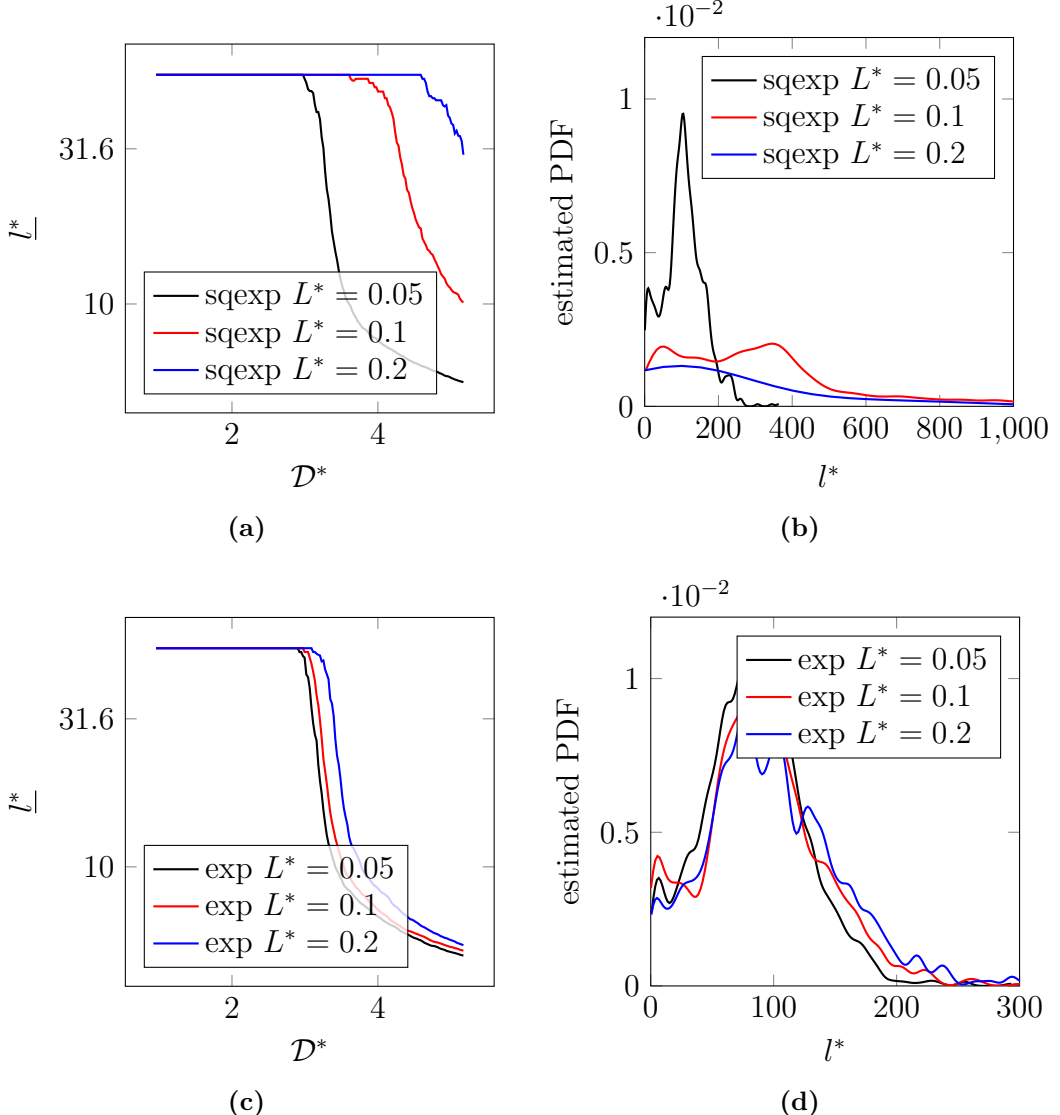


FIGURE 4.16. (a, c) Mean dimensionless crack spacing \underline{l}^* versus dimensionless crack driving force D^* (b, d) Estimated probability density of dimensionless crack spacing for different values of correlation length when $D^* = 5.17$ based on (a-b) a PSE kernel (c-d) a PE kernel

with the aim of understanding which field plays a dominant role in determining the resulting fracture morphology in thin films.

In order to obtain meaningful statistical results, 10 independent realizations are considered, and the same samples (of the underlying Gaussian random fields) are used when ρ varies. The normalized correlation length is set to $L^* = 0.05$ for

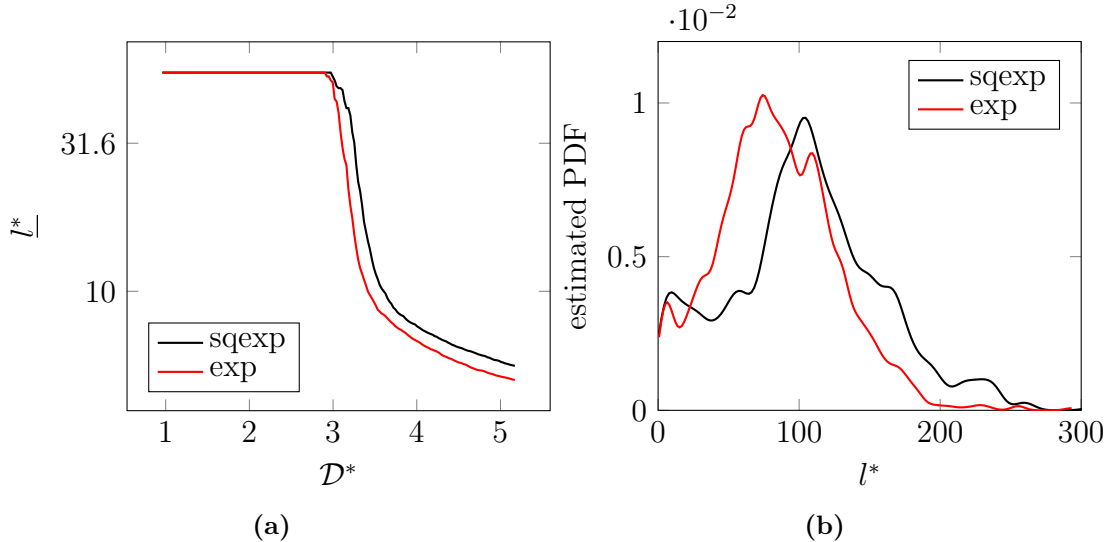


FIGURE 4.17. Comparisons of (a) mean dimensionless crack spacing \underline{l}^* versus dimensionless crack driving force D^* and (b) Estimated probability density of dimensionless crack spacing for different values of correlation length when $D^* = 5.17$ for results obtained using a PSE kernel and a PE kernel

both fracture properties. Three pairs of fracture toughness and critical fracture energy samples, constructed using (4.34) and (4.35) with $\rho \in \{0, 0.5, 1\}$, are shown in Figure 4.18. Note that the special case of $\rho = 0$ recovers the case of independent material properties.

Statistics of the dimensionless crack spacing l^* are once again extracted at $D^* = 5.17$. The resulting dimensionless curves and normalized probability density functions are shown in Figures 4.19 and 4.20. These results indicate that the distribution of fragment size is relatively insensitive to the coefficient of correlation, regardless of the smoothness of the covariance kernel.

In contrast, when we superimpose the fracture patterns, we observe that the fracture morphology does exhibit a sensitivity to variations in the fracture toughness (Figure 4.21a). The superimposed results are only shown for the PSE covariance function, but comparable results are obtained with the PE covariance function. By comparison, when the fracture toughness is held fixed while the critical fracture

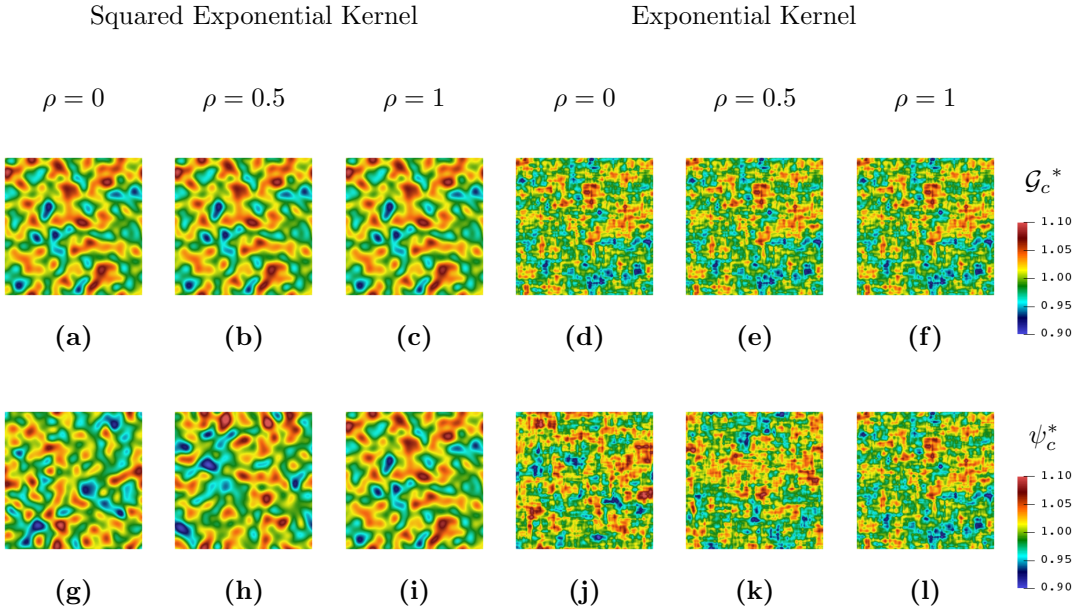


FIGURE 4.18. Point-wise correlated material properties: (a-f) normalized fracture toughness \mathcal{G}_c^* and (g-l) normalized critical fracture energy ψ_c^* with (left) PSE covariance function (right) PE covariance function

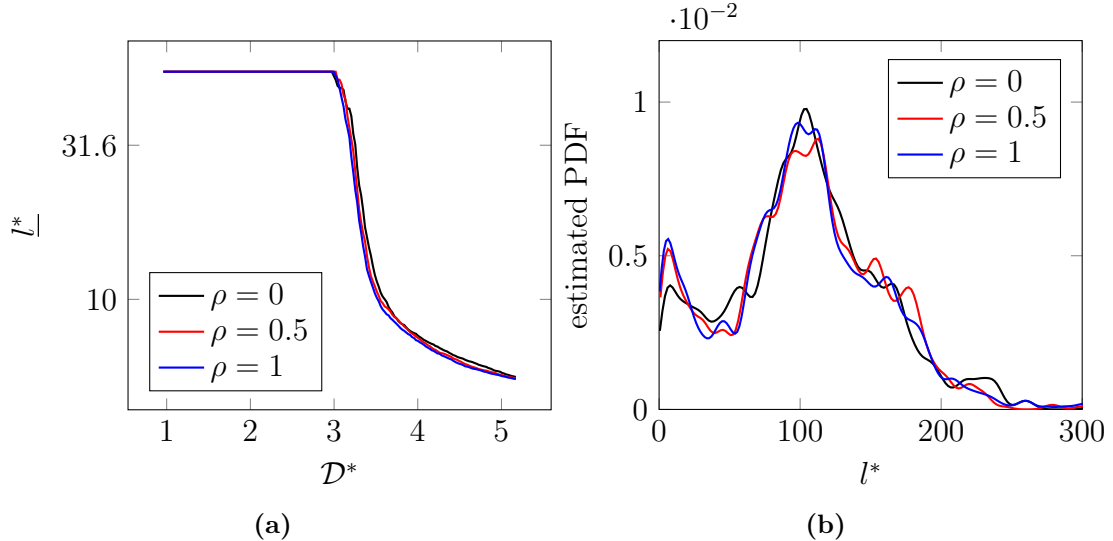


FIGURE 4.19. Comparisons of (a) mean dimensionless crack spacing as a function of dimensionless crack driving force and (b) estimated PDFs of dimensionless fragment size at loading $\mathcal{D}^* = 5.17$ for results with an underlying PSE kernel

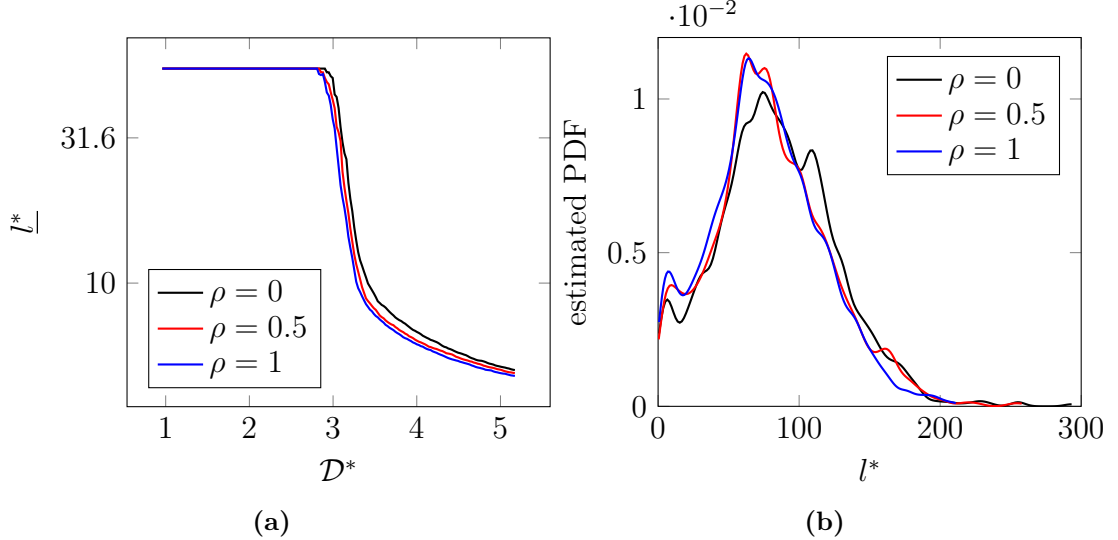


FIGURE 4.20. Comparisons of (a) mean dimensionless crack spacing and dimensionless crack driving force and (b) estimated PDFs of dimensionless fragment size at loading $D^* = 5.17$ for results with an underlying PE kernel

energy is varied, the superimposed fracture patterns are nearly indistinguishable (Figure 4.21b). The clear conclusion is that the energetics are primarily responsible for driving the fracture morphology, a result that is not surprising. This conclusion is also supported by the results shown in Figures 4.22 and 4.23, in which fracture patterns are plotted over contours of the fracture toughness and the critical energy. For both types of covariance functions, the fracture patterns are seen to follow contours of minimal fracture toughness while largely ignoring those of the critical fracture energy.

Discussion on Modeling Flexibility: Impact of the Covariance Structure

We now briefly examine how different structures of the covariance kernel can alter the fragment morphology. It has been demonstrated experimentally [71, 72, 73, 74, 75] how macro-scale processing conditions to construct samples may lead to morphologically different crack networks. For example, Kitsunezaki et al. [74] carried out a series of tests to study the effect of macroscopic disturbances on crack patterns.

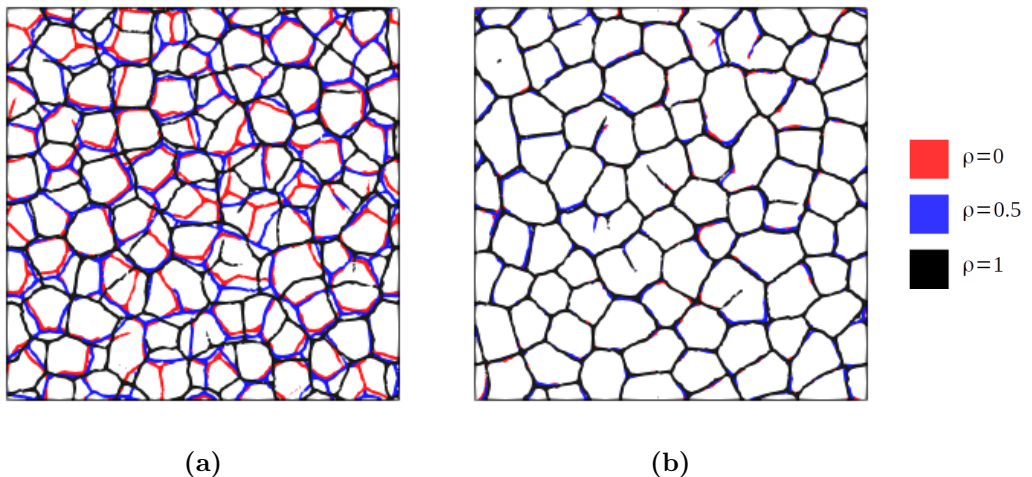


FIGURE 4.21. Superposition of fracture networks obtained by three samples of different coefficients of correlation, using the PSE kernel. Only the volume within the damage contour of $d = 0.9$ is shown to represent the resulting fracture network. Three samples are sampled (a) by holding \mathcal{G}_c constant and (b) by holding ψ_c constant.

They poured calcium carbonate (CaCO_3) paste into a shallow circular container. Different modes of agitation were applied to the paste before it was dried, and the resulting crack patterns showed a strong correlation with the modes of agitation.

We hypothesize that the agitation gives rise to effective fracture properties at the macro-scale that have a structure that is consistent with the agitation. We further assume a rougher spatial variation of properties in the direction parallel to the agitation than in the direction orthogonal to the agitation. Accordingly, we model the spatial variations in the fracture properties using composite covariance functions, defined on purpose by a tensor-product structure involving PSE and PE functions. In Figure 4.24, we compare the experimentally-observed crack patterns to our simulation results obtained using random fracture properties with the postulated anisotropic covariance functions. The comparison shows reasonable agreement (without specifically optimizing the hyperparameters in the stochastic model), indicating that the differing processing conditions may have resulted in different spatial

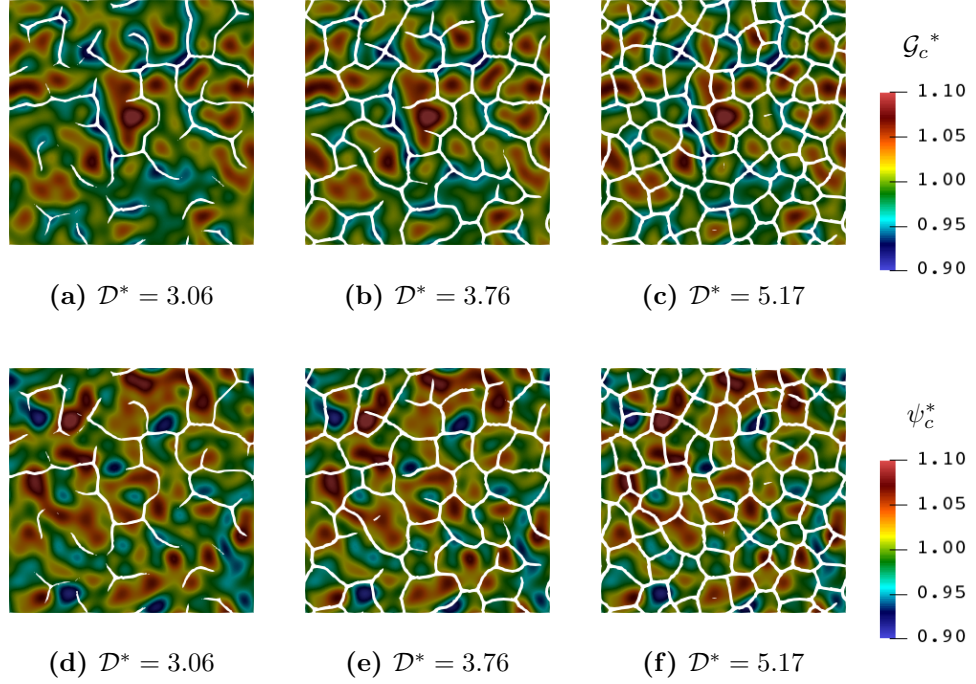


FIGURE 4.22. Snapshots of damage field at different loading levels with $d \geq 0.75$ plotted over (a-c) fracture toughness \mathcal{G}_c and (d-f) critical fracture energy ψ_c with an underlying PSE covariance function

variations in the effective fracture properties.

4.4.3 Inverse Identification Based on Three-Dimensional Physical Experiments

In Rodriguez [1], a series of drying tests with mining waste placed on grooved circular plates (225 mm in diameter) was performed to observe crack evolution due to desiccation processes. Three tests were carried out with different film thicknesses $h \in \{4 \text{ mm}, 8 \text{ mm}, \text{ and } 16 \text{ mm}\}$.

To replicate this study using model-based simulations and our phase-field model (enhanced with the stochastic description of fracture properties), we adopt fully three-dimensional models. The material properties used for this study are listed in Table 4.2. Consistent with the experimental studies of [1], the film-substrate system is represented by a cylindrical domain. The substrate is modeled as a rigid body

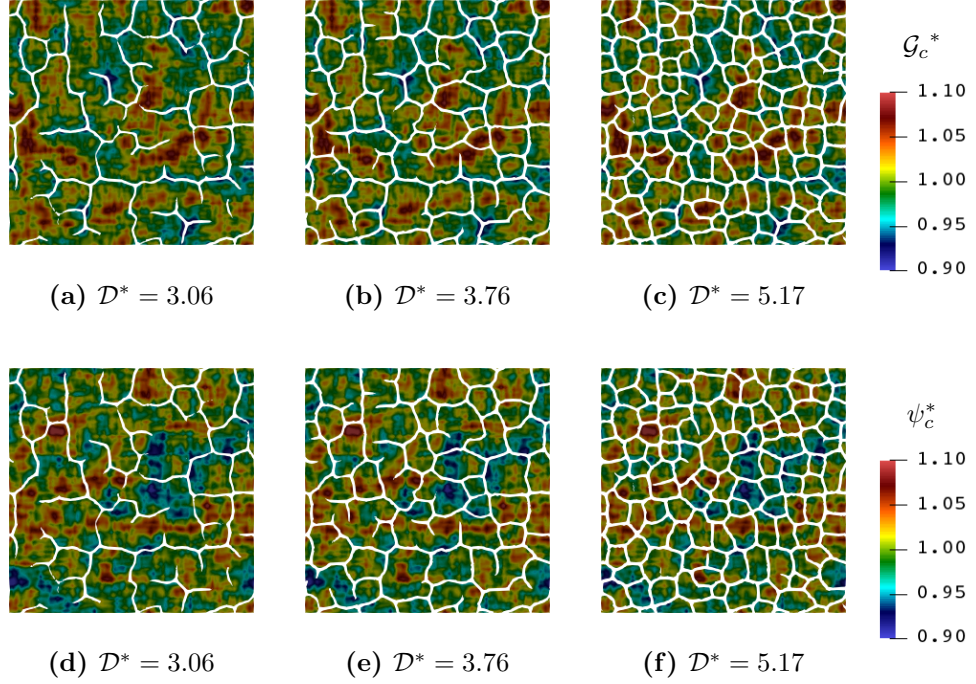


FIGURE 4.23. Snapshots of damage field at different loading levels with $d \geq 0.75$ plotted over (a-c) fracture toughness \mathcal{G}_c and (d-f) critical fracture energy ψ_c with an underlying PE covariance function

Table 4.2. Summary of material properties of mining waste and model parameters for all calculations in ??

Property/Parameter	Symbol	Value	Unit	Comment
Young's modulus	E	4	MPa	See [65]
Poisson's ratio	ν	0.2	nondim.	See [65]
Mean fracture toughness	$\underline{\mathcal{G}}_c$	27	kJ m^{-2}	See [96, 97]
Mean critical fracture energy	$\underline{\psi}_c$	30	J m^{-2}	See [96, 97]
Regularization length	l	0.8	mm	Such that $2l/h^e \approx 5$
Degradation shape parameter	p	1	nondim.	

with an arbitrarily high fracture toughness. The substrate and film are discretized using tetrahedral elements with characteristic lengths of $h_0^e = 1.6$ mm and $h_1^e = 0.36$ mm, respectively. The solutions to the linear elasticity subproblem, the phase-field for fracture subproblem, and the generalized eigenvalue problem are once again

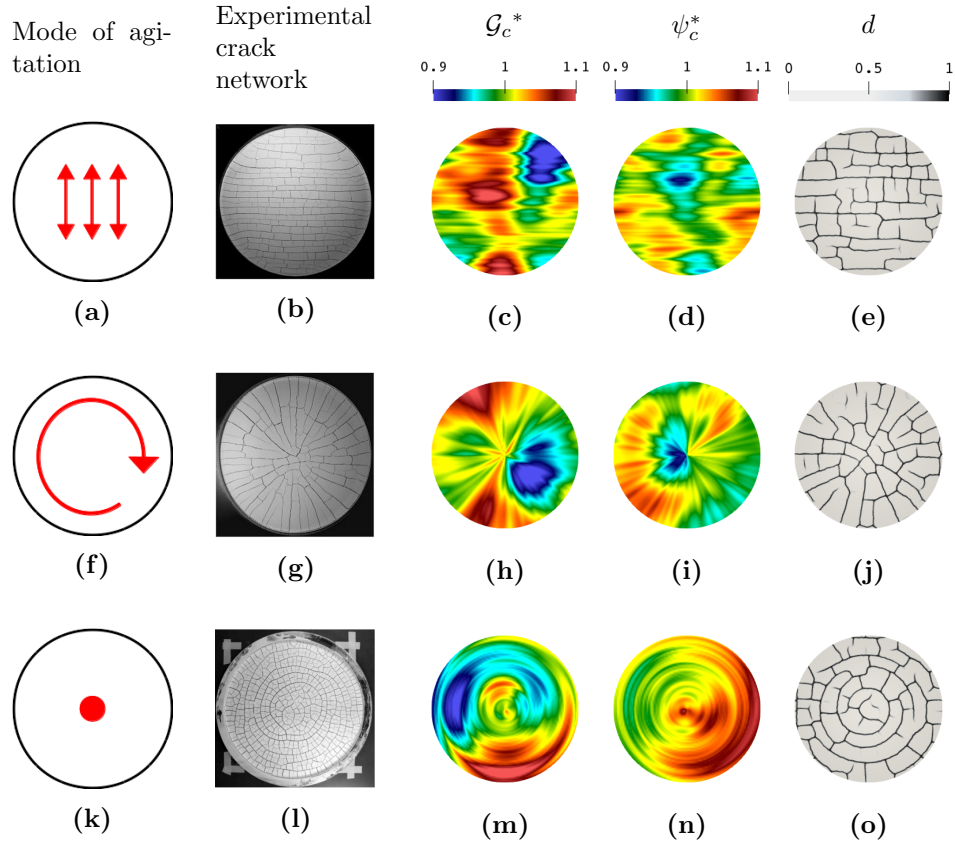


FIGURE 4.24. Three sets of experiments and calculations for (a-e) unilateral agitation (f-j) rotational agitation (k-o) point agitation. (b, g, l) snapshots of crack patterns from experiments. postulated spatially correlated (c, h, m) fracture toughness and (d, i, n) critical fracture energy to reproduce experimental observations. (e, j, o) damage fields obtained using corresponding spatially varying material properties.

approximated using the same mesh.

We first calibrate the spatial variability in our model against the experimental observations of the fracture patterns for the thinnest ($h = 4\text{mm}$) specimen. To formulate the statistical inverse problem, we assume that (1) the fracture toughness and the critical fracture energy are uncorrelated (i.e., $\rho = 0$); and (2) both fracture properties have the same coefficient of variation (set to 0.03) and spatial correlation lengths, and that they can be defined using isotropic squared exponential kernels.

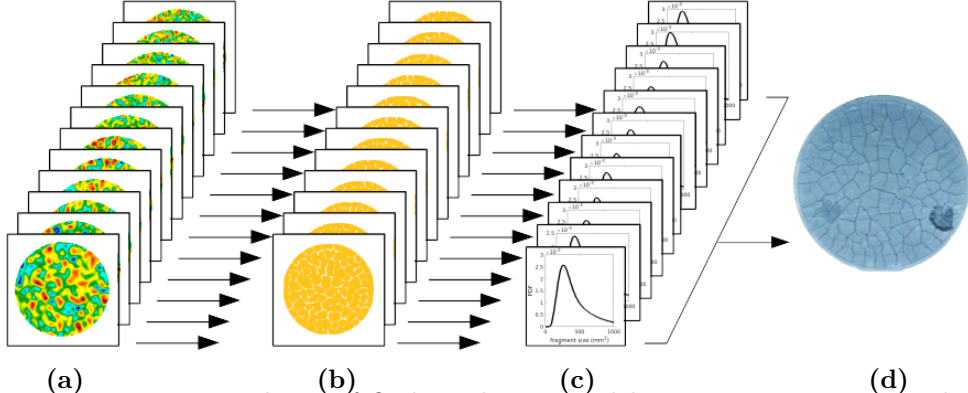


FIGURE 4.25. Procedures of finding the optimal hyperparameter to match the experiment: (a) 12 pairs of fracture properties are sampled to explore the space of admissible spatial correlation lengths; three dimensional energy minimization problems are solved to obtain (b) the resulting fracture morphology; (c) distributions of fragment sizes are extracted from the simulated results, and the log-likelihood values of these distributions at the samples extracted from (d) the experimental fracture morphology are computed.

In addition, the variations of the properties through the thickness of the film are assumed negligible compared to in-plane variations.

Based on these assumptions, the spatial correlation length L is the only parameter to be determined, and a parametric search is performed in $\mathbb{L} = \{ 3 \text{ mm}, 3.5 \text{ mm}, 4 \text{ mm}, 4.5 \text{ mm}, 5 \text{ mm}, 5.5 \text{ mm}, 6 \text{ mm}, 6.5 \text{ mm}, 7 \text{ mm}, 7.5 \text{ mm}, 8 \text{ mm}, 8.5 \text{ mm} \}$. Energy minimization problems for the case of $h = 4 \text{ mm}$ are simulated for each pair of realizations and the corresponding fracture patterns are obtained. For a given value of $L \in \mathbb{L}$, the flooding algorithm is used to identify fragments on the top surface of the thin film, and a kernel density estimation of the probability density function associated with the fragment size, denoted by $f_{\text{fs}}^{\text{sim}}(\cdot; L)$, is obtained. The optimal value of L is then identified by maximizing the log-likelihood function \mathcal{L} defined as

$$\mathcal{L}(L) = \sum_{A_{\text{fs}}^{\text{exp}} \in \mathbb{A}_{\text{exp}}} \ln f_{\text{fs}}^{\text{sim}}(l^*(A_{\text{fs}}^{\text{exp}}); L) , \quad l^*(A) = \frac{\sqrt{A}}{h} , \quad (4.77)$$

where \mathbb{A}_{exp} denotes the collection of fragment size samples extracted by using the same flooding algorithm on the experimental result. The aforementioned workflow

to calibrate the model is summarized in Figure 4.25. The fracture properties with spatial correlation $L = 4$ mm lead to the maximum log-likelihood among the span of samples considered. Figure 4.26 compares the estimated PDF and the fracture morphology obtained using the calibrated stochastic model to those of the experimental specimen for $h = 4$ mm.

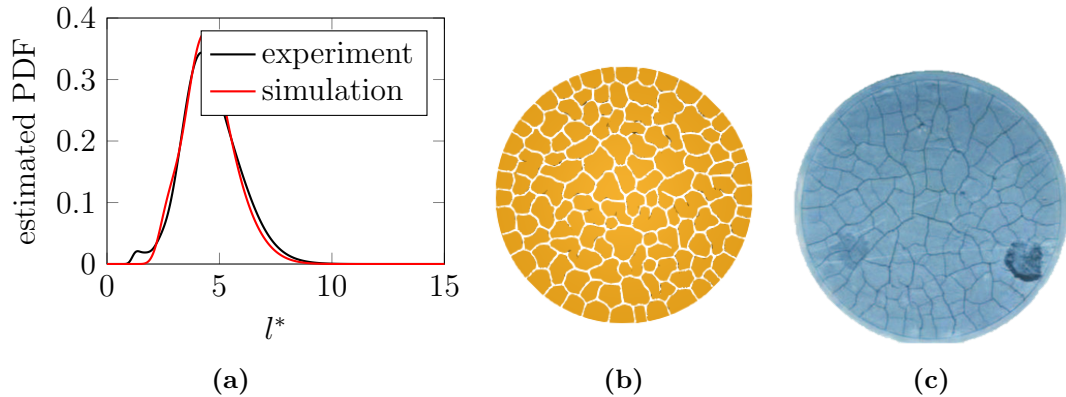


FIGURE 4.26. (a) Estimated PDFs of the dimensionless fragment sizes extracted from the experimental result and the calibrated stochastic model. (b) Fracture morphology obtained using the calibrated fracture properties. (c) Photograph of cracks in the mining waste.

To then benchmark our model against specimens with different thicknesses, three 3D calculations are carried out using the same realization of fracture properties with $L = 4$ mm. As shown in Figure 4.27, our results appear to agree reasonably well with the experimental observations. In general, the thicker films fracture into larger fragments, which also agrees with the simplified models presented in ????.

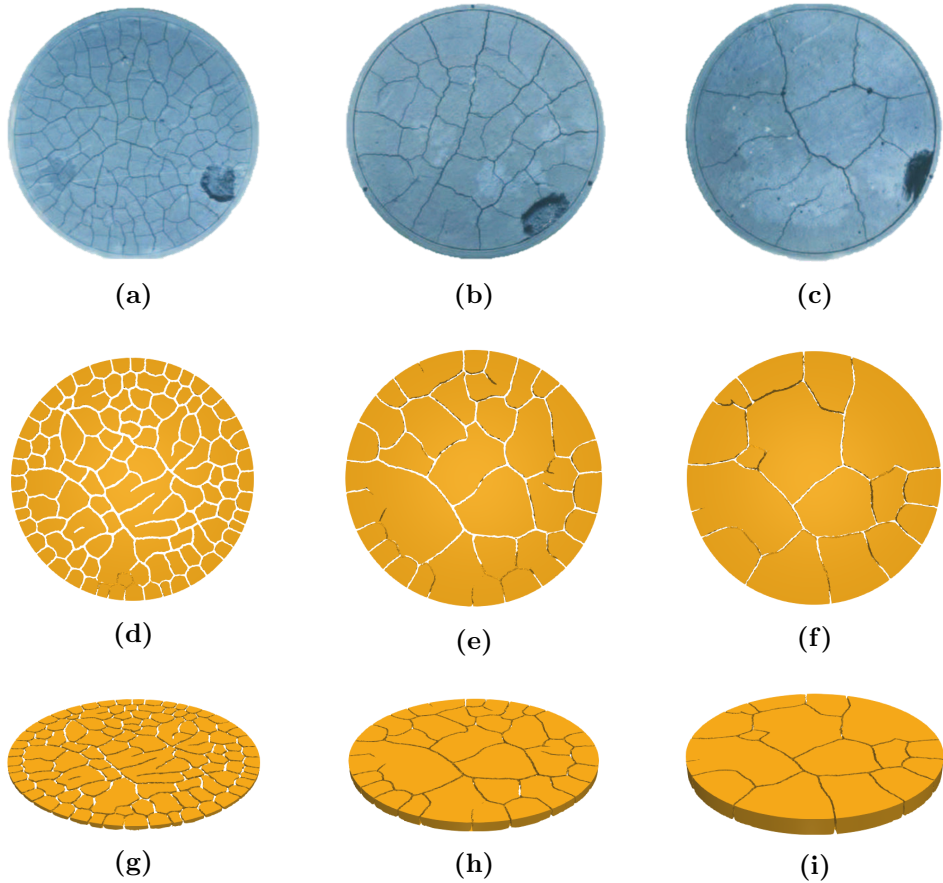


FIGURE 4.27. Qualitative comparison between the experiments and the simulations: (a-c) Photographs (modified from [1]) of cracks in mining waste due to desiccation at steady state for three test specimens with thickness (a) 4 mm, (b) 8 mm, and (c) 16 mm. (d-f) Top view and (g-i) panoramic view of corresponding numerical simulation results with different film thickness. Volumes of material with $d \geq 0.75$ were removed to improve the visualization of the crack geometry.

5

Towards Ductile Fracture

5.1 Introduction

5.2 Theory

5.2.1 *Constitutive choices*

5.2.2 *A power-law approximation to the yield surface*

5.2.3 *Variational constitutive updates*

5.3 Verification

5.3.1 *A homogeneous example: uniaxial constitutive response*

5.3.2 *A nonhomogeneous example: uniaxial load-displacement curves*

5.3.3 *Crack resistance curves*

5.4 Numerical examples

5.4.1 *Three-point bending*

5.4.2 *The Sandia Fracture Challenge*

5.4.3 *Spallation of oxidation scale*

6

Conclusion

Appendix A

Code availability

Appendix B

On the phase-field irreversibility constraint

Appendix C

The flooding algorithm for counting fragments

We describe the algorithm for clustering various elements in a mesh to individual fragments, as delineated by a damage field. The algorithm assigns each element a cluster order parameter, and different clusters are separated by a band of “broken” elements where the damage is above a threshold, i.e. $d > d_{\text{th}}$. Figure C.1 provides an example of this algorithm for a representative damage field.

The algorithm has a fundamental “flooding” structure. In particular, a seeding element broadcasts its information to all of its geometric neighbors, and each neighbor becomes a new seed for the next round of information propagation. In the context of counting fragments, the information of an element includes its state and the cluster it belongs to. An element is considered to be “intact” if all of its nodal damage values are below d_{th} , otherwise it is considered to be “broken”.

Three lists are managed by the algorithm. The first list **ALL** includes all elements that need to be classified. The second list **CANDIDATE**, optionally a first-in-first-out (FIFO) queue, includes all candidate elements for the current cluster. The third list **BROKEN** includes all “broken” elements. Each cluster CLUSTER^i is essentially a list of

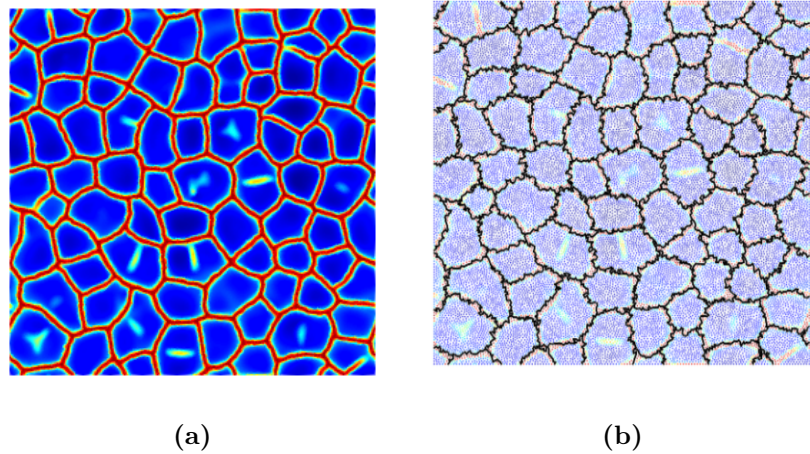


FIGURE C.1. (a) Final damage field obtained using a spatially correlated random \mathcal{G}_c and ψ_c . (b) Corresponding clusters labeled by the flooding algorithm. Cluster boundaries are marked in black.

elements that belong to the same parent cluster.

The algorithm consists of three stages. In the first stage, we update the damage values of all nodes and states of all elements. All elements that have a status change require reclassification. Therefore, any cluster that contains elements pending reclassification is pushed into **ALL** for future reclassification.

In the second stage, all “intact” elements in **ALL** are pushed into **CANDIDATE** one at a time until **ALL** has no more “intact” elements. Each new cluster is constructed by dequeuing **CANDIDATE**. The first element in **CANDIDATE** is dequeued after all of its connecting “intact” elements from **ALL** are pushed into **CANDIDATE**.

During the third stage, “broken” elements are grouped into their nearest cluster to preserve the total volume of the mesh. In our implementation, “broken” elements are assigned to clusters based on the solution to a minimization problem of weighted Euclidean distance between the elements and cluster centroids.

The skeleton of the flooding algorithm is outlined in Algorithm 1.

Algorithm 1 An iterative flooding algorithm for fragmentation count

```
1: Set  $d_0 \leftarrow 0$ 
2: Set cluster count  $c \leftarrow 0$ 
3: Group all elements into  $\text{CLUSTER}^c$ 
4: for time step  $n \in \{0, 1, 2, \dots\}$  do
5:   for each cluster  $\text{CLUSTER}^i$  do
6:     Move all “broken” elements into  $\text{BROKEN}$ 
7:     if  $\text{CLUSTER}^i$  contains any element that has a state change, i.e. from “intact” to “broken” then
8:       Move all remaining elements into  $\text{ALL}$ 
9:     end if
10:    end for
11:    while  $\text{ALL}$  is not empty do
12:      if All elements in  $\text{ALL}$  are “broken” then
13:        Move all elements in  $\text{ALL}$  into  $\text{BROKEN}$ 
14:        Break while loop
15:      else
16:        Move one “intact” element from  $\text{ALL}$  to  $\text{CANDIDATE}$ 
17:        Increment cluster count  $c \leftarrow c + 1$ 
18:        while  $\text{ALL}$  is not empty do
19:          for each element  $e$  that shares a common edge with the first element
in the queue  $\text{CANDIDATE}$  do
20:            if  $e$  is “intact” then
21:              Enqueue  $e$  into  $\text{CANDIDATE}$ 
22:            else
23:              Move  $e$  into  $\text{BROKEN}$ 
24:            end if
25:          end for
26:          Dequeue first element in  $\text{CANDIDATE}$  into  $\text{CLUSTER}^c$ 
27:        end while
28:      end if
29:    end while
30:    Move all elements in  $\text{BROKEN}$  into their nearest cluster
31: end for
```

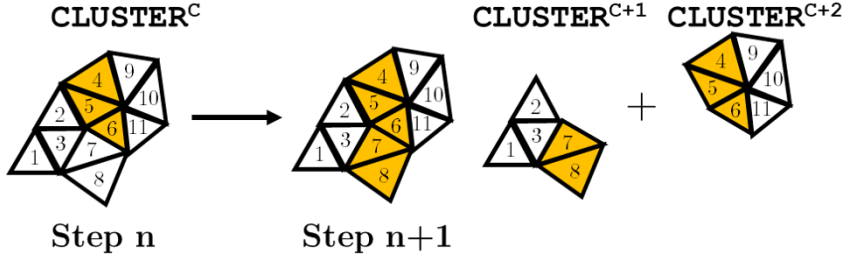


FIGURE C.2. Status change from step n to step $n+1$. “Broken” elements are labeled in yellow, and “intact” elements are white. The step-by-step reclassification procedure is shown in Table C.1.

Table C.1. Demonstration of classification after the update from time step n to time step $n+1$. Broken elements are denoted with an underscore.

Step	Stage	ALL	CANDIDATE	BROKEN	Comments
n		\emptyset	\emptyset	\emptyset	$CLUSTER^c = \{1, 2, 3, \underline{4}, \underline{5}, \underline{6}, 7, 8, 9, 10, 11\}$
$n+1$		\emptyset	\emptyset	\emptyset	$CLUSTER^c = \{1, 2, 3, \underline{4}, \underline{5}, \underline{6}, \underline{7}, \underline{8}, 9, 10, 11\}$
$n+1$	1	$\{1, 2, 3, 9, 10, 11\}$	\emptyset	$\{\underline{4}, \underline{5}, \underline{6}, \underline{7}, \underline{8}\}$	Declassify $CLUSTER^c$
$n+1$	2	$\{2, 3, 9, 10, 11\}$	$\{1\}$	$\{\underline{4}, \underline{5}, \underline{6}, \underline{7}, \underline{8}\}$	Enqueue element 1 to CANDIDATE
$n+1$	2	$\{9, 10, 11\}$	$\{1, 2, 3\}$	$\{\underline{4}, \underline{5}, \underline{6}, \underline{7}, \underline{8}\}$	Enqueue connected elements 2, 3
$n+1$	2	$\{9, 10, 11\}$	$\{2, 3\}$	$\{\underline{4}, \underline{5}, \underline{6}, \underline{7}, \underline{8}\}$	Dequeue element 1
$n+1$	2	$\{9, 10, 11\}$	$\{3\}$	$\{\underline{4}, \underline{5}, \underline{6}, \underline{7}, \underline{8}\}$	Dequeue element 2
$n+1$	2	$\{9, 10, 11\}$	\emptyset	$\{\underline{4}, \underline{5}, \underline{6}, \underline{7}, \underline{8}\}$	Dequeue element 3
$n+1$	2	$\{10, 11\}$	$\{9\}$	$\{\underline{4}, \underline{5}, \underline{6}, \underline{7}, \underline{8}\}$	$CLUSTER^{c+1} = \{1, 2, 3\}$
$n+1$	2	\emptyset	$\{9, 10, 11\}$	$\{\underline{4}, \underline{5}, \underline{6}, \underline{7}, \underline{8}\}$	Enqueue element 9 to CANDIDATE
$n+1$	2	\emptyset	$\{10, 11\}$	$\{\underline{4}, \underline{5}, \underline{6}, \underline{7}, \underline{8}\}$	Enqueue connected elements 10, 11
$n+1$	2	\emptyset	$\{11\}$	$\{\underline{4}, \underline{5}, \underline{6}, \underline{7}, \underline{8}\}$	Dequeue element 9
$n+1$	2	\emptyset	\emptyset	$\{\underline{4}, \underline{5}, \underline{6}, \underline{7}, \underline{8}\}$	Dequeue element 10
$n+1$	2	\emptyset	\emptyset	$\{\underline{4}, \underline{5}, \underline{6}, \underline{7}, \underline{8}\}$	Dequeue element 11
$n+1$	3	\emptyset	\emptyset	$\{\underline{4}, \underline{5}, \underline{6}\}$	Group elements 7, 8 into $CLUSTER^{c+1}$
$n+1$	3	\emptyset	\emptyset	\emptyset	Group elements 4, 5, 6 into $CLUSTER^{c+2}$

Bibliography

- [1] R Rodriguez. Hydrogeotechnical characterization of a metallurgical waste. *Canadian Geotechnical Journal*, 43(10):1042–1060, 2006.
- [2] Gianni Dal Maso. *An introduction to Γ -convergence*, volume 8. Springer Science & Business Media, 2012.
- [3] Qiang Yang, Laurent Stainier, and Michael Ortiz. A variational formulation of the coupled thermo-mechanical boundary-value problem for general dissipative solids. *Journal of the Mechanics and Physics of Solids*, 54(2):401–424, 2006.
- [4] Timo Heister, Mary F Wheeler, and Thomas Wick. A primal-dual active set method and predictor-corrector mesh adaptivity for computing fracture propagation using a phase-field approach. *Computer Methods in Applied Mechanics and Engineering*, 290:466–495, 2015.
- [5] Satish Balay, Shrirang Abhyankar, Mark F. Adams, Jed Brown, Peter Brune, Kris Buschelman, Lisandro Dalcin, Alp Dener, Victor Eijkhout, William D. Gropp, Dmitry Karpeyev, Dinesh Kaushik, Matthew G. Knepley, Dave A. May, Lois Curfman McInnes, Richard Tran Mills, Todd Munson, Karl Rupp, Patrick Sanan, Barry F. Smith, Stefano Zampini, Hong Zhang, and Hong Zhang. PETSc Web page. <https://www.mcs.anl.gov/petsc>, 2019. URL <https://www.mcs.anl.gov/petsc>.
- [6] Tianchen Hu, Johann Guilleminot, and John E Dolbow. A phase-field model of fracture with frictionless contact and random fracture properties: Application to thin-film fracture and soil dessication. *Computer Methods in Applied Mechanics and Engineering*, 368:113106, 2020.
- [7] Nathan Capps, Colby Jensen, Fabiola Cappia, Jason Harp, Kurt Terrani, Nicolas Woolstenhulme, and Daniel Wachs. A critical review of high burnup fuel fragmentation, relocation, and dispersal under loss-of-coolant accident conditions. *Journal of Nuclear Materials*, 546:152750, 2021.
- [8] Vincenzo V. Rondinella and Thierry Wiss. The high burn-up structure in nuclear fuel. *Materials Today*, 13(12):24–32, 2010.

- [9] J. A. Turnbull, S. K. Yagnik, M. Hirai, D. M. Staicu, and C. T. Walker. An assessment of the fuel pulverization threshold during loca-type temperature transients. *Nuclear Science and Engineering*, 179(4):477–485, 2015.
- [10] Wen Jiang, Benjamin W. Spencer, and John E. Dolbow. Ceramic nuclear fuel fracture modeling with the extended finite element method. *Engineering Fracture Mechanics*, 223:106713, 2020. ISSN 0013-7944.
- [11] Katalin Kulacsy. Mechanistic model for the fragmentation of the high-burnup structure during loca. *Journal of Nuclear Materials*, 466:409 – 416, 2015.
- [12] Lars O. Jernkvist. A review of analytical criteria for fission gas induced fragmentation of oxide fuel in accident conditions. *Progress in Nuclear Energy*, 119:103188, 2020. ISSN 0149-1970.
- [13] Pritam Chakraborty, Yongfeng Zhang, and Michael R. Tonks. Multi-scale modeling of microstructure dependent intergranular brittle fracture using a quantitative phase-field based method. *Computational Materials Science*, 113:38 – 52, 2016. ISSN 0927-0256.
- [14] Martin Diehl, Marcel Wicke, Pratheek Shanthraj, Franz Roters, Angelika Brueckner-Foit, and Dierk Raabe. Coupled crystal plasticity–phase field fracture simulation study on damage evolution around a void: Pore shape versus crystallographic orientation. *JOM*, 69(5):872–878, May 2017.
- [15] Chukwudi Chukwudzie, Blaise Bourdin, and Keita Yoshioka. A variational phase-field model for hydraulic fracturing in porous media. *Computer Methods in Applied Mechanics and Engineering*, 347:957 – 982, 2019.
- [16] Andro Mikelić, Mary F Wheeler, and Thomas Wick. A quasi-static phase-field approach to pressurized fractures. *Nonlinearity*, 28(5):1371–1399, apr 2015.
- [17] Jian-Ying Wu. A unified phase-field theory for the mechanics of damage and quasi-brittle failure. *Journal of the Mechanics and Physics of Solids*, 103:72 – 99, 2017.
- [18] Zachary A. Wilson and Chad M. Landis. Phase-field modeling of hydraulic fracture. *Journal of the Mechanics and Physics of Solids*, 96:264 – 290, 2016. ISSN 0022-5096.
- [19] Keita Yoshioka, Dmitri Naumov, and Olaf Kolditz. On crack opening computation in variational phase-field models for fracture. *Computer Methods in Applied Mechanics and Engineering*, 369:113210, 2020.
- [20] B. Bourdin, G.A. Francfort, and JJ Marigo. The variational approach to fracture. *Journal of Elasticity*, 91:5 – 148, 2008.

- [21] K. Govers. Comparison of interatomic potentials for UO₂. *Journal of Nuclear Materials*, 366:161–177, 2007.
- [22] N. Moelans, B. Blanpain, and P. Wollants. Quantitative analysis of grain boundary properties in a generalized phase field model for grain growth in anisotropic systems. *Phys. Rev. B*, 78:024113, Jul 2008.
- [23] E.N. Hodkin. The ratio of grain boundary energy to surface energy of nuclear ceramics as determined from pore geometries. *Journal of Nuclear Materials*, 88 (1):7 – 14, 1980. ISSN 0022-3115.
- [24] G.L. Reynolds, W.B. Beeré, and P.T. Sawbridge. The effect of fission products on the ratio of grain-boundary energy to surface energy in irradiated uranium dioxide. *Journal of Nuclear Materials*, 41(1):112 – 114, 1971. ISSN 0022-3115.
- [25] Mohamed S. Ebeida, Scott A. Mitchell, Anjul Patney, Andrew A. Davidson, and John D. Owens. A simple algorithm for maximal poisson-disk sampling in high dimensions. *Computer Graphics Forum*, 31(2pt4):785–794, 2012.
- [26] M. Oguma. Microstructure effects on fracture strength of UO₂ fuel pellets. *Journal of Nuclear Science and Technology*, 19(12):1005–1014, 1982.
- [27] A. G. Evans and R. W. Davidge. The strength and fracture of stoichiometric polycrystalline UO₂. *Journal of Nuclear Materials*, 33:249–260, 1969.
- [28] M. Oguma. Microstructure effects on fracture strength of u02 fuel pellets. *Journal of Nuclear Science and Technology*, 19(12):1005–1014, 1982.
- [29] Anders Puranen. Post test examinations on loca tested rods. Studsvik Report STUDSVIK/N-13/198, Studsvik, 2013.
- [30] R. L. Williamson, J. D. Hales, S. R. Novascone, G. Pastore, K. A. Gamble, B. W. Spencer, W. Jiang, S. A. Pitts, A. Casagrande, D. Schwen, A. X. Zabriskie, A. Toptan, R. Gardner, C. Matthews, W. Liu, , and H. Chen. Bison: A flexible code for advanced simulation of the performance of multiple nuclear fuel forms. *Nuclear Technology*, 2020.
- [31] L. K. Aagesen, S. Biswas, W. Jiang, A. M. Jokisaari, D. Andersson, M. W. D. Cooper, and C. Matthews. Determine fragmentation criteria in high-burnup uo₂ fuel during accident conditions. Technical Report INL/EXT-20-00558, Idaho National Laboratory, 2020.
- [32] G.A. Francfort and J.J. Marigo. Revisiting brittle fracture as an energy minimization problem. *Journal of the Mechanics and Physics of Solids*, 46(8):1319–1342, 1998.

- [33] B. Bourdin, G.A. Francfort, and J.J. Marigo. Numerical experiments in revisited brittle fracture. *Journal of the Mechanics and Physics of Solids*, 48(4):797–826, 2000.
- [34] Blaise Bourdin, Gilles A Francfort, and Jean-Jacques Marigo. The variational approach to fracture. *Journal of elasticity*, 91(1-3):5–148, 2008.
- [35] A. Karma, D. A. Kessler, and H. Levine. Phase-field model of mode III dynamic fracture. *Physical Review Letters*, 87(4):045501–1–4, 2001.
- [36] A. Karma and A. E. Lobkovsky. Unsteady crack motion and branching in a phase-field model of brittle fracture. *Physical Review Letters*, 93(10):245510, 2004.
- [37] H. Henry and H. Levine. Dynamic instabilities of fracture under biaxial strain using a phase field model. *Physical Review Letters*, 93(10):105504, 2004.
- [38] R. Spatschek, C. M. Gugenberger, and E. Brener. Phase field modeling of fracture and stress-induced phase transitions. *Physical Review E*, 75:066111, 2007.
- [39] H. Amor, J. J. Marigo, and C. Maurini. Regularized formulation of the variational brittle fracture with unilateral contact: Numerical experiments. *Journal of the Mechanics and Physics of Solids*, 57(8):1209–1229, 2009.
- [40] AAL Baldelli, B Bourdin, JJ Marigo, and C Maurini. Delamination and fracture of thin films: a variational approach. *Direct and variational methods for nonsmooth problems in mechanics Amboise, France*, 2013.
- [41] AA León Baldelli, J-F Babadjan, Blaise Bourdin, Duvan Henao, and Corrado Maurini. A variational model for fracture and debonding of thin films under in-plane loadings. *Journal of the Mechanics and Physics of Solids*, 70:320–348, 2014.
- [42] C. Miehe, F. Welschinger, and M. Hofacker. Thermodynamically consistent phase-field models of fracture: Variational principles and multi-field FE implementations. *International Journal for Numerical Methods in Engineering*, 83: 1273–1311, 2010.
- [43] C. Miehe, M. Hofacker, and F. Welschinger. A phase field model for rate-independent crack propagation: Robust algorithmic implementation based on operator splits. *Computer Methods in Applied Mechanics and Engineering*, 199: 2765–2778, 2010.
- [44] Hanen Amor, Jean-Jacques Marigo, and Corrado Maurini. Regularized formulation of the variational brittle fracture with unilateral contact: Numerical

experiments. *Journal of the Mechanics and Physics of Solids*, 57(8):1209 – 1229, 2009. ISSN 0022-5096.

- [45] Michael Strobl and Thomas Seelig. A novel treatment of crack boundary conditions in phase field models of fracture. *Pamm*, 15(1):155–156, 2015.
- [46] Michael Strobl and Thomas Seelig. On constitutive assumptions in phase field approaches to brittle fracture. *Procedia Structural Integrity*, 2:3705–3712, 2016.
- [47] Fan Fei and Jinyun Choo. A phase-field method for modeling cracks with frictional contact. *arXiv preprint arXiv:1905.10547*, 2019.
- [48] Fan Fei and Jinyun Choo. A phase-field model of geologic shear fracture, 2020.
- [49] Yu-Sheng Lo, Michael Borden, K. Ravi-Chandar, and Chad M. Landis. A phase-field model for fatigue crack growth. *Journal of the Mechanics and Physics of Solids*, 132(103684), 2019.
- [50] JTA Roberts, E Smith, N Fuhrman, and D Cubicciotti. On the pellet-cladding interaction phenomenon. *Nuclear Technology*, 35(1):131–144, 1977.
- [51] Bruno Michel, Jérôme Sercombe, Gilles Thouvenin, and Rémy Chatelet. 3d fuel cracking modelling in pellet cladding mechanical interaction. *Engineering fracture mechanics*, 75(11):3581–3598, 2008.
- [52] Lars Olof Jernkvist. A model for predicting pellet-cladding interaction-induced fuel rod failure. *Nuclear engineering and design*, 156(3):393–399, 1995.
- [53] Fumihisa Nagase and Toyoshi Fuketa. Effect of pre-hydriding on thermal shock resistance of zircaloy-4 cladding under simulated loss-of-coolant accident conditions. *Journal of nuclear science and technology*, 41(7):723–730, 2004.
- [54] Michael Billone, Yong Yan, Tatiana Burtseva, Robert Daum, et al. Cladding embrittlement during postulated loss-of-coolant accidents. Technical report, Argonne National Lab.(ANL), Argonne, IL (United States), 2008.
- [55] Mohamed M El-Basyouny and Matthew Witczak. Calibration of alligator fatigue cracking model for 2002 design guide. *Transportation research record*, 1919(1):76–86, 2005.
- [56] Sherif M El-Badawy, Myung Goo Jeong, and Mohamed El-Basyouny. Methodology to predict alligator fatigue cracking distress based on asphalt concrete dynamic modulus. *Transportation Research Record*, 2095(1):115–124, 2009.
- [57] T Saar and O Talvik. Automatic asphalt pavement crack detection and classification using neural networks. In *2010 12th Biennial Baltic Electronics Conference*, pages 345–348. IEEE, 2010.

- [58] Joe W Button and Robert L Lytton. Guidelines for using geosynthetics with hot-mix asphalt overlays to reduce reflective cracking. *Transportation Research Record*, 2004(1):111–119, 2007.
- [59] Yetkin Yildirim, Ahmed Qatan, Jorge Prozzi, et al. *Field manual for crack sealing in asphalt pavements.*, 2006.
- [60] John W Hutchinson and Zhigang Suo. Mixed mode cracking in layered materials. In *Advances in applied mechanics*, volume 29, pages 63–191. Elsevier, 1991.
- [61] Kevin M Crosby and R Mark Bradley. Fragmentation of thin films bonded to solid substrates: Simulations and a mean-field theory. *Physical Review E*, 55(5):6084, 1997.
- [62] Kwan-tai Leung and Zoltan Néda. Pattern formation and selection in quasistatic fracture. *Physical review letters*, 85(3):662, 2000.
- [63] Supti Sadhukhan, Tapati Dutta, and Sujata Tarafdar. Crack formation in composites through a spring model. *Physica A: Statistical Mechanics and its Applications*, 390(4):731–740, 2011.
- [64] Jingwen Zhang, Yuyang Lu, Linghui He, Lizhong Yang, and Yong Ni. Modeling progressive interfacial debonding of a mud-crack film on elastic substrates. *Engineering Fracture Mechanics*, 177:123–132, 2017.
- [65] Marcelo Sánchez, Osvaldo L Manzoli, and Leonardo JN Guimarães. Modeling 3-d desiccation soil crack networks using a mesh fragmentation technique. *Computers and Geotechnics*, 62:27–39, 2014.
- [66] J Liang, R Huang, Jean-Herve Prevost, and Z Suo. Evolving crack patterns in thin films with the extended finite element method. *International Journal of Solids and Structures*, 40(10):2343–2354, 2003.
- [67] N Sukumar and J-H Prévost. Modeling quasi-static crack growth with the extended finite element method part i: Computer implementation. *International journal of solids and structures*, 40(26):7513–7537, 2003.
- [68] Rui Huang, N Sukumar, and J-H Prévost. Modeling quasi-static crack growth with the extended finite element method part ii: Numerical applications. *International Journal of Solids and Structures*, 40(26):7539–7552, 2003.
- [69] Z Cedric Xia and John W Hutchinson. Crack patterns in thin films. *Journal of the Mechanics and Physics of Solids*, 48(6-7):1107–1131, 2000.
- [70] HM Yin, GH Paulino, and William G Buttlar. An explicit elastic solution for a brittle film with periodic cracks. *International Journal of Fracture*, 153(1):39, 2008.

- [71] So Kitsunezaki, Akio Nakahara, and Yousuke Matsuo. Shaking-induced stress anisotropy in the memory effect of paste. *EPL (Europhysics Letters)*, 114(6):64002, 2016.
- [72] So Kitsunezaki, Yousuke Matsuo, and Akio Nakahara. Stress development up to crack formation in drying paste. *Journal of Chemical Engineering of Japan*, 50(10):775–779, 2017.
- [73] Zoltán Halász, Akio Nakahara, So Kitsunezaki, and Ferenc Kun. Effect of disorder on shrinkage-induced fragmentation of a thin brittle layer. *Physical Review E*, 96(3):033006, 2017.
- [74] So Kitsunezaki, Arina Sasaki, Akihiro Nishimoto, Tsuyoshi Mizuguchi, Yousuke Matsuo, and Akio Nakahara. Memory effect and anisotropy of particle arrangements in granular paste. *The European Physical Journal E*, 40(10):88, 2017.
- [75] Akio Nakahara, Tomoki Hiraoka, Rokuya Hayashi, Yousuke Matsuo, and So Kitsunezaki. Mechanism of memory effect of paste which dominates desiccation crack patterns. *Philosophical Transactions of the Royal Society A*, 377(2136):20170395, 2018.
- [76] Katherine A. Acton, Sarah C. Baxter, Bahador Bahmani, Philip L. Clarke, and Reza Abedi. Voronoi tessellation based statistical volume element characterization for use in fracture modeling. *Computer Methods in Applied Mechanics and Engineering*, 336:135 – 155, 2018.
- [77] Darith-Anthony Hun, Johann Guilleminot, Julien Yvonnet, and Michel Bornert. Stochastic multiscale modeling of crack propagation in random heterogeneous media. *International Journal for Numerical Methods in Engineering*, 119(13):1325–1344, 2019.
- [78] C. Peco, Y. Liu, C. Rhea, and J.E. Dolbow. Models and simulations of surfactant-driven fracture in particle rafts. *International Journal of Solids and Structures*, 156:194–209, 2019.
- [79] Jian-Ying Wu and Miguel Cervera. A thermodynamically consistent plastic-damage framework for localized failure in quasi-brittle solids: Material model and strain localization analysis. *International Journal of Solids and Structures*, 88:227–247, 2016.
- [80] Jian-Ying Wu. A unified phase-field theory for the mechanics of damage and quasi-brittle failure. *Journal of the Mechanics and Physics of Solids*, 103:72–99, 2017.
- [81] Rudy JM Geelen, Yingjie Liu, Tianchen Hu, Michael R Tupek, and John E Dolbow. A phase-field formulation for dynamic cohesive fracture. *Computer Methods in Applied Mechanics and Engineering*, 348:680–711, 2019.

- [82] Eric Lorentz, Sam Cuvilliez, and Kyrylo Kazymyrenko. Convergence of a gradient damage model toward a cohesive zone model. *Comptes Rendus Mécanique*, 339(1):20–26, 2011.
- [83] Eric Lorentz. A nonlocal damage model for plain concrete consistent with cohesive fracture. *International Journal of Fracture*, 207(2):123–159, 2017.
- [84] Mircea Grigoriu. Existence and construction of translation models for stationary non-gaussian processes. *Probabilistic Engineering Mechanics*, 24:545–551, 2009.
- [85] E.T. Jaynes. Information theory and statistical mechanics i. *Physical Review*, 106(4):620–630, 1957.
- [86] E.T. Jaynes. Information theory and statistical mechanics ii. *Physical Review*, 108(2):171–190, 1957.
- [87] C.E. Shannon. A mathematical theory of communication. *Bell System Technical Journal*, 27(3):379–423, 1948.
- [88] C.E. Shannon. A mathematical theory of communication. *Bell System Technical Journal*, 27(4):623–656, 1948.
- [89] N. Balakrishnan and C.-D. Lai. *Continuous Bivariate Distributions*. Springer-Verlag New York, 2009.
- [90] Patrick Moran. Statistical inference with bivariate gamma distributions. *Biometrika Trust*, 56:627–634, 1969.
- [91] R. G. Ghanem and P. D. Spanos. *Stochastic Finite Elements: A Spectral Approach (Revised Edition)*. Dover, 2003.
- [92] O. Le Maître and O. Knio. *Spectral Methods for Uncertainty Quantification*. Springer Netherlands, 2010.
- [93] J.L. Beuth. Cracking of thin bonded films in residual tension. *International Journal of Solids and Structures*, 29(13):1657 – 1675, 1992. ISSN 0020-7683.
- [94] R Obrzud. *The hardening soil model: A practical guidebook*. Zace Services, 2010.
- [95] A Ramsaroop, K Kanny, and TP Mohan. Fracture toughness studies of polypropylene-clay nanocomposites and glass fibre reinforced polypropylene composites. *Materials Sciences and Applications*, 1(05):301, 2010.
- [96] R Rodríguez, Marcelo Sanchez, A Ledesma, and A Lloret. Experimental and numerical analysis of desiccation of a mining waste. *Canadian Geotechnical Journal*, 44(6):644–658, 2007.

- [97] MR Lakshmikantha, PC Prat, and A Ledesma. Image analysis for the quantification of a developing crack network on a drying soil. *Geotechnical Testing Journal*, 32(6):505–515, 2009.

Biography

About myself.